Active Flux Methods with Gradient Degrees of Freedom

by

Iman Samani

A dissertation submitted in partial fulfillment
of the requirements for the degree of
Doctor of Philosophy
(Aerospace Engineering)
in the University of Michigan
2024

Doctoral Committee:

Professor Philip L. Roe, Chair
Professor Karthik Duraisamy
Professor Krzysztof J. Fidkowski
Professor Shravan K. Veerapaneni

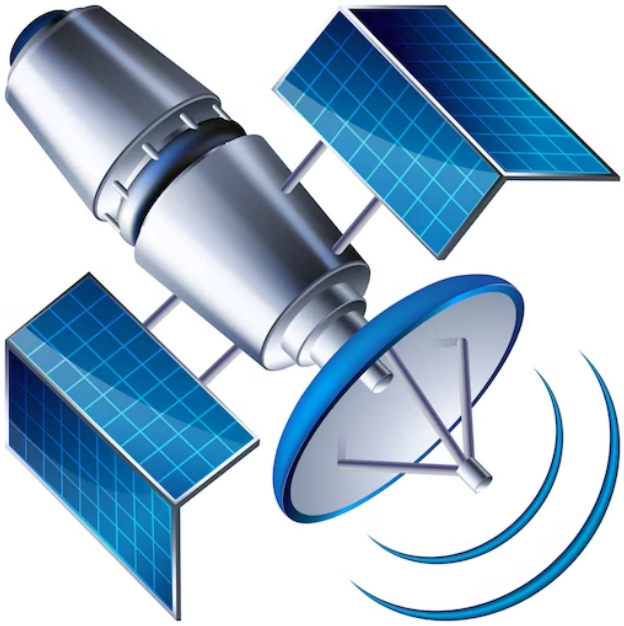

Iman Samani
isamani@umich.edu
ORCID iD: 0000-0002-7999-5930

DEDICATION

I dedicate this thesis to my beloved parents, Hamidreza and Zahra, whose unwavering support, endless encouragement, and boundless love have been my guiding light throughout this challenging academic journey. Your sacrifices, wisdom, and unshakable belief in my abilities have been the cornerstone of my success. You have shown me the value of determination, resilience, and the pursuit of knowledge. This thesis stands as a tribute to your enduring faith in me, and I am forever grateful for the sacrifices you have made to help me achieve my dreams. Thank you for being my pillars of strength, and for inspiring me to reach for the stars. This accomplishment is as much yours as it is mine.

ACKNOWLEDGEMENTS

I want to express my heartfelt appreciation to those individuals who have provided invaluable support and encouragement throughout my doctoral studies at the University of Michigan. My deepest gratitude goes to my advisor, Phil Roe, whose unwavering guidance and insights in mathematics have been instrumental in shaping my academic journey. Our discussions, characterized by their helpful nature, often concluded with more questions than I initially posed. I believe this dynamic has significantly contributed to my growth as a researcher and adept problem solver. While Phil's profound knowledge spans both technical and philosophical dimensions of the field, I find myself more profoundly influenced by his perspective and approach to life beyond the academic sphere. Both Phil and his wife, Jacqui, have consistently extended a warm welcome since our first meeting, leaving a lasting impression that I will always cherish and value.

Gratitude extends to my committee members, Karthik Duraisamy, Krzysztof J. Fidkowski, and Shravan K. Veerapaneni, for their invaluable expert insights and opinions.

Heartfelt thanks to my parents for their unwavering support and care throughout my graduate studies and beyond. Without their constant encouragement and belief in my decisions, I wouldn't be the person I am today. Thanks also to my sister and brothers for being a continual source of strength during my academic journey. Your love and encouragement have been invaluable, adding depth and meaning to every milestone. I consider myself truly blessed to have such a loving and supportive family.

Deep gratitude to my friends who have been a constant presence throughout my academic journey. Your camaraderie and support have transformed difficulties into shared moments of ease during our gatherings. Thank you for the laughter, encouragement, and understanding that made this journey memorable. Having friends like you by my side has truly enriched the entire experience.

Lastly, profound thanks to my exceptional wife, Mahnaz, for her unwavering love, constant support throughout every step of this journey, and unshakable belief in me.

TABLE OF CONTENTS

LIST OF FIGURES

FIGURE

LIST OF TABLES

TABLE

LIST OF ALGORITHMS

ALGORITHM

LIST OF APPENDICES

APPENDIX

LIST OF ACRONYMS

AF Active Flux

EMI Electromagnetic Interference

DG Discontinuous Galerkin

FDM Finite Difference Methods

FEM Finite Element Methods

FVM Finite Volume Methods

GSM Global Spectral Methods

LES Large Eddy Simulation

MCT Multidimensional Corner Treatment

ABSTRACT

This thesis presents a numerical approach designed to solve wave propagation problems with high accuracy on an unstructured grid. The method employs a fully explicit approach with a compact stencil, addressing both material and remote boundaries automatically. The ultimate goal is to contribute to the development of a highly accurate Navier-Stokes code for aeroacoustic predictions, specifically focusing on waves with wavelengths not significantly larger than the grid size. In essence, the aim is to accurately capture short waves using relatively coarse and cost-effective unstructured grids that can represent intricate geometric details.

The underlying hypothesis is based on the belief that, for ensuring accuracy, particularly in terms of bandwidth – which is often more crucial than achieving high formal accuracy – the method must be fully-discrete and explicit. This choice is driven by the recognition that a numerical stencil, while encompassing the analytical domain of dependence to prevent instability, should not be excessively large. An overly large stencil includes irrelevant data, leading to either instability or an overly dissipative scheme. Moreover, semi-discrete methods, despite enabling high formal accuracy for long waves, prove less effective in ensuring well-behaved mid- and high-frequency behavior due to the gradual inclusion of data from outside the true domain of dependence unless the time step is significantly reduced.

Any endeavor to enhance accuracy invariably involves the processing of additional information, commonly achieved by enlarging the stencil. However, in the scenario of element enlargement, where irrelevant information is incorporated into a large stencil, it not only encounters the issues previously outlined but also poses challenges on irregular grids and in proximity to boundaries. An alternative approach is to augment the set of information retained at each location, as demonstrated in methods such as Discontinuous Galerkin and Active Flux. This extended set of information encompasses various variables, including but not limited to values, gradients, and element averages of the solution.

Guided by these heuristics, the thesis establishes a general framework applicable across arbitrary dimensions and levels of element accuracy. It introduces an analytical solution designed to smooth initial-value wave propagation problems. Consequently, a Hermitian version of the Active Flux method is devised in two dimensions, successfully retaining the ad-

vantages of optimal one-dimensional methods. There is a high likelihood that extending this method to three dimensions will be straightforward. Notably, the algorithm autonomously identifies the correct direction of propagating waves, forming a robust foundation for non-reflecting boundary conditions and addressing multi-material problems. The efficacy of the method is demonstrated through various interface conditions in acoustics and elastodynamics wave propagation.

This method attains at least fifth-order accuracy and provides compelling numerical evidence for a form of superconvergence, indicating the potential for highly precise solutions. In doing so, it significantly propels the state-of-the-art in solving wave propagation problems.

CHAPTER 1

Introduction

The demand for numerical methods to address temporal wave propagation problems is great and spans many industries, including aviation, electronics, and geophysics, among others.

In the aviation industry, which holds a pivotal role in modern society, substantial environmental concerns and repercussions have emerged. As a response to these challenges, there is mounting pressure for the aviation sector to adopt "greener" technologies [2]. A notable aspect of this endeavor is noise reduction [3]. Aeroacoustics is dedicated to the science of noise management in aviation, presenting unique computational challenges. Noise in aviation originates from highly energetic flow patterns, rendering conventional acoustic methods ineffective. Furthermore, destructive interference often results in only a small fraction of the noise reaching distant observers. Common approaches involve solving the Euler equations, linearized about a nonlinear base flow [4, 5]. Often, a zonal approach [6] is employed, solving the full Euler or Navier-Stokes equations in the near-field, and adopting progressively simplified models at greater distances [7].

Similarly, the electronics industry also grapples with wave propagation challenges, where the solutions to Maxwell's equations become crucial [8, 9]. Maxwell's equations govern the behavior of electromagnetic waves and are fundamental to the operation of electronic devices. Accurate numerical methods are essential for the design and analysis of electronic components, circuits, and systems. Challenges in electronics involve high-frequency wave propagation, signal integrity, and Electromagnetic Interference (EMI) management [10]. Effective numerical techniques are vital to address these complexities and optimize electronic systems.

In the field of geophysics, wave propagation plays a vital role in earthquake prediction and seismic hazard assessment [11]. Here, elastodynamic equations are solved to model the behavior of seismic waves in the Earth's crust and mantle. These simulations aid in understanding earthquake mechanisms, ground motion predictions, and the evaluation of structural responses to seismic events. Numerical methods are indispensable for simulating

the propagation of seismic waves through complex geological structures, allowing scientists to make critical assessments for disaster preparedness and infrastructure resilience [12]. However, the challenges in geophysics involve the modeling of multiscale and multiphysics phenomena, as well as the need for high-performance computing resources to handle large-scale simulations [13].

Ongoing challenges persist in wave propagation problems, require continuous attention and innovative solutions. These challenges encompass various facets, including but not limited to: accurate wave propagation across extensive distances, management of remote boundary conditions, navigating complex geometrical configurations, and overcoming wave propagation obstacles through disparate materials, encompassing air, structures, and acoustic linings.

To effectively tackle these challenges, it's crucial to utilize specialized numerical methods that align with the unique characteristics of each problem. These distinct features demand dedicated strategies and methodologies for developing numerical schemes that can provide accurate approximations for the solutions required in such complex scenarios. Practical issues specifically addressed in this thesis include a capacity to compute on coarse grids by resolving the high frequencies through Hermite approximation, a capacity to propagate weak waves over large distances by reducing numerical dissipation,a capacity to compute problems having remote boundaries without the use of large grids, a capacity to operate with arbitrary unstructured grids to deal with complex geometry, and a capacity to capture material interfaces in a very compact manner.

1.1 Contemporary Numerical Approaches in Wave Propagation Problems

Numerical approaches in wave propagation problems are computational techniques and methodologies used to simulate and analyze the behavior of waves as they propagate through various mediums and interact with different structures. The subsequent sections delve into a review of some of these practices.

1.1.1 Finite Difference Methods

Finite Difference Methods (FDM) discretize the continuous domain into a grid of discrete points, approximating the derivatives through finite difference approximations. FDM are straightforward to incorporate and have undergone extensive scrutiny in prior research [14, 15]. Despite their age and simplicity, these schemes continue to be widely employed in various

applications, including optimized FDM for aeroacoustics simulations [16], Yee schemes for Maxwell's equations [17], and FDM simulations for seismic wave propagation [18]. These schemes have maintained their popularity due to their simplicity of implementation and fully explicit formulations. High-order FDM can be created by enlarging the stencil width in one dimension space and/or modifying its shape in higher dimensions.

One drawback of finite difference techniques lies in the challenge they face when simulating waves in intricate domains in higher dimensions.

1.1.2 Finite Element Methods

Finite Element Methods (FEM) rely on the concept that a computational domain can be represented as a collection of interconnected elements, often organized in an unstructured manner [19].

In the context of FEM [20, 21, 22], each of these elements is used to approximate the solution, employing piecewise polynomials known as basis functions. These basis functions are carefully selected to ensure accuracy and continuity across element boundaries. Subsequently, FEM proceeds to assemble a global system of equations, combining the element-level equations derived from all interconnected elements. This process results in the creation of a large, sparse matrix system that encapsulates the equations governing the problem. Upon the assembly of the global system and the imposition of boundary conditions, numerical solvers, such as direct solvers or iterative methods, are employed to acquire the solution to this system of equations. However, these techniques often lose their efficiency when dealing with large global systems. An alternative method, introduced in the early 1970s, is the Discontinuous Galerkin (DG) method [23]. DG methods aim to independently approximate the solution within each element by utilizing test functions confined to the local elemental space. By distributing the data at element interfaces and having the capability to approximate the local solution with any desired level of accuracy using the test functions, a highly-accurate and compact method emerges. Nevertheless, this comes at the cost of increased memory requirements and computational expenses[24]. It also leads to semi-discretisations that impose small time steps and can misrepresent high frequencies [25].

1.1.3 Finite Volume Methods

Similar to FEM, Finite Volume Methods (FVM) also partitions the computational domain into interconnected elements, referred to as control volumes in FVM. Within each of these control volumes, it employs a conservative approach to approximate the solution by considering the conservation of quantities across the interfaces of these control volumes. A Riemann

solver is often used to calculate the fluxes at the interfaces by solving Riemann problems at each interface [26, 27]. Extending Riemann solvers to multidimensional cases is a straightforward process, involving the solution of Riemann problems normal to the element face. However, this approach designed for one-directional wave motion and makes an assumption that all waves propagate strictly perpendicular to element interfaces, which can lead to the generation of nonphysical waves dependent on the grid geometry rather than representing genuine flow features.

Numerous endeavors have been pursued to rectify the irregularities present in the solutions. These efforts encompass a combination of simplified wave solvers, such as HLL or Rusanov, in conjunction with full Riemann solvers as highlighted in [28]. Additionally, researchers have explored the application of the Multidimensional Corner Treatment (MCT) method, originally conceived by Colella [29], and have investigated various rotated Riemann techniques, including those documented in [30, 31, 32]. These approaches are designed to ameliorate the observed issues within the solutions. Nevertheless, it is essential to acknowledge that while these methods effectively mitigate the symptoms of the problem, they often introduce higher computational complexity and do not fundamentally resolve the root issue, which persists in the fact that the modified solvers remain grounded in one-dimensional physics.

Roe, in [33, 34], highlights the necessity of modeling multidimensional physical processes in nonlinear systems with numerical methods that consider the appropriate domain of dependence. For omnidirectional wave propagations, this entails utilizing information from circular domains in two dimensions and spherical domains in three dimensions. This requirement poses a fundamental challenge for inherently one-dimensional schemes like Riemann solvers. Previous efforts to develop schemes, such as fluctuation splitting or residual distribution methods introduced by Roe for linear advection [35], have attempted to circumvent the use of Riemann solvers. These methods, extended to hyperbolic-elliptic systems by Rad, have achieved third-order accuracy and demonstrated the ability to approximate potential flow around elliptical bodies in steady-state problems [36, 37]. They afford many points of similarity with the present method and these will be explored in future research.

1.1.4 Global Spectral Methods

In contrast to finite methods, the Global Spectral Methods (GSM) represent the solution as a superposition of basis functions, over the entire computational domain [38, 39, 40, 41]. These basis functions are selected to satisfy boundary conditions and accurately capture the behavior of the underlying problem. A multitude of options exist for these basis func-

tions, including trigonometric functions, Chebyshev polynomials, and Legendre polynomials, among others.

The strength of the GSM lies in its ability to provide exponentially accurate solutions. Nonetheless, due to its global nature, GSM is characterized by the dense and intricate algebraic formulation of its basis functions, introduces computational complexity and costs. As a consequence, it is especially well-suited for problems involving relatively straightforward domains of simple shape, but less suited to complex domains. Furthermore, this global nature poses challenges when attempting to implement parallel computations efficiently.

1.1.5 Active Flux

Active Flux (AF) method represents a novel approach aimed at addressing the limitations of existing methods discussed in prior sections. Its foundation lies in Scheme V, which was identified by van Leer in a 1977 paper as the most efficient among six schemes he devised to achieve better-than-first-order convergence for the one-dimensional advection problem [42]. Scheme V introduces additional edge values alongside the element-average value for each element and utilizes these extra degrees of freedom to enhance solution accuracy up to third order. The AF method independently updates interface values based on edge values, incorporating both the previous element average and previous edge values. Notably, the interface update need not be conservative; the only requirement is that fluxes are consistent, allowing flexibility in choosing an edge update method. This flexibility enables the incorporation of multidimensional physics, breaking free from the constraints of solving one-dimensional Riemann problems. The AF method currently operates at third-order accuracy and has found applications in diverse problem domains, including unsteady, compressible, two-dimensional Euler equations on arbitrary unstructured grids [43, 44]. In this context, it has demonstrated superior cost-effectiveness, achieving comparable accuracy in significantly less time, compared to the DG method with quadratic reconstruction. Further optimization of the implementation promises to enhance this advantage by a factor of two to three. The AF method boasts a compact nature, versatility across structured and unstructured grids, and can be efficiently coded as a loop over elements.

1.2 Towards High-Order Methods

The current accuracy standard in commercial numerical solvers is second-order due to the desire to maintain low computational costs. However, the increasing demand for solving more intricate problems has sparked an interest in developing high-order methods. Re-

cent advancements in high-order methods have revealed that they can, in fact, be more cost-effective than lower-order alternatives while maintaining the same level of error [45]. Nevertheless, the advantages offered by existing high-order methods are not significant or established enough to entice developers to switch their tools. Additionally, many of these methods face issues related to robustness, a crucial requirement for production codes.

In our pursuit of high-order method development, we are guided by the recommendations outlined in [25]. One key recommendation is that the method should be fully discrete and explicit. This approach is chosen because while the numerical stencil needs to encompass the analytical domain of dependence to prevent instability, an overly large numerical stencil can include irrelevant data, leading to instability or excessive dissipation in the scheme. Furthermore, any semi-discrete method progressively expands its stencil at each stage, eventually incorporating data from outside the true domain of dependence unless the time step is significantly reduced. Consequently, while semi-discrete methods can provide high formal accuracy for long waves, they are less effective in ensuring proper behavior for mid- and high-frequency components.

Any effort to enhance accuracy typically involves processing more information, often achieved by expanding the stencil, as seen in methods like ENO [46] and its various derivatives such as WENO [47], H-WENO [48], and TENO [49], as well as dispersion-preserving methods [50, 51]. However, the enlargement of the stencil not only encounters the previously mentioned issues but also poses challenges on irregular grids and near boundaries. An alternative approach involves enriching the set of variables retained at each location, as demonstrated by Discontinuous Galerkin and Active Flux methods. We will begin by exploring these options in one spatial dimension, aiming to glean valuable insights related to low-frequency accuracy, bandwidth, resolution of discontinuities, and the prevention of undamped high-frequency modes.

1.2.1 Stencil Enlargement

We can convey our points without delving into the intricacies of ENO/WENO/TENO and simply by examining the application of basic finite difference methods to linear advection. These observations are equally applicable to more sophisticated methods. It's a well-established fact that odd-order schemes outperform even-order schemes [52, 53]. Iserles and Strang [54] have demonstrated that the most effective odd-order polynomial interpolation schemes have slightly biased stencils, featuring one additional mesh point on the upwind side. They also established that this family of schemes remains stable for Courant numbers within the range of $[0, 1]$. In Figure 1.1, we present the amplification factors for finite differ-

ence schemes of order 3, 5, and 7. We consider a Courant number of 0.25 on the left and 0.75 on the right. The plotted quantity is $g(\nu,\theta)^{1/\nu}$, where $g(\nu,\theta)$ represents the amplification of a sine wave with frequency θ in a single timestep. Taking this value to the power of $1/\nu$ yields the "normalized amplification" as the wave traverses one element.

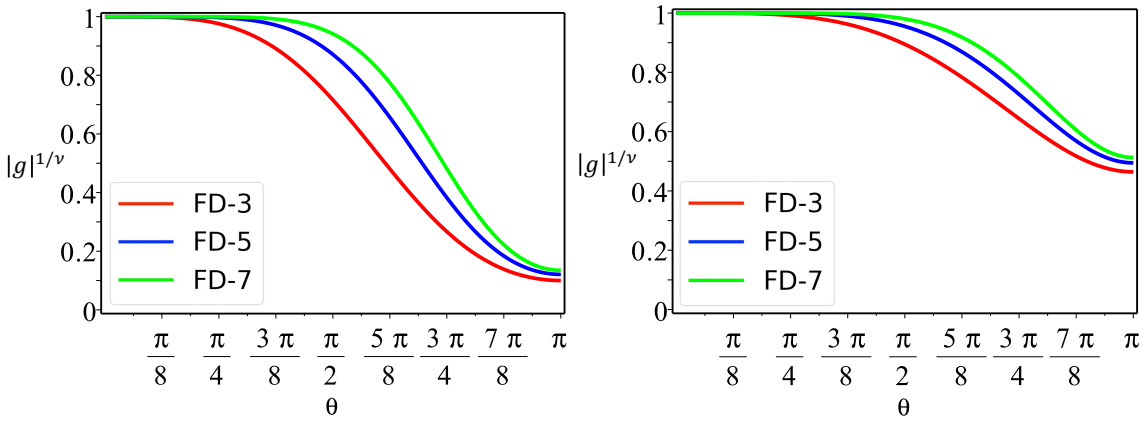

Figure 1.1: Normalized amplification of finite difference schemes. **left:** $\nu = 0.25$ and **right:** $\nu = 0.75$.

Indeed, as we elevate the order of the schemes, we observe a wider range of accurately treated frequencies. However, the enhancements appear somewhat underwhelming, especially considering the significant increase in complexity, which becomes particularly pronounced in higher dimensions. The primary reason for this is the larger stencil, which extends well beyond the domain of dependence. While it provides additional information, this information is primarily useful for low frequencies. Essentially, we have more data, but it is of lower quality. When confronted with higher frequencies for which the method lacks pertinent information, it attempts to mitigate them, albeit not very effectively, especially at $\nu = 0.75$. This consideration is particularly pertinent in the context of Large Eddy Simulation (LES), where a "scale gap" can exist between the resolved low frequencies and the unresolved yet "modeled" frequencies [55]. Our aim is to bridge this gap and eliminate it entirely.

When tackling a problem that involves long-distance wave propagation, it's essential to determine the required mesh size in terms of points per wavelength to maintain the amplitude within a specified tolerance. In this analysis, we set a stringent criterion of preserving the amplitude within one part in a thousand for each cell crossed. Table 1.1 presents the outcomes for our three finite difference schemes and highlights the anticipated trends.

An alternative measure of the quality of an advection scheme lies in its ability to accurately represent a traveling square wave. General theoretical insights into this aspect are available [52, 53]. For even-order methods, the phase error predominates over the amplification error,

Order	$\nu = 0.25$	$\nu = 0.50$	$\nu = 0.75$
3	18.0	16.4	13.6
5	9.6	9.1	8.0
7	7.0	6.7	6.1

Table 1.1: Number of points per wavelength necessary to maintain amplitude within 0.1% per wavelength of travel for three finite difference schemes.

leading to modes with incorrect phase speeds that are only weakly damped, resulting in pronounced spurious oscillations on one side of a discontinuity. These oscillations typically have an amplitude of around 20 to 25%. Therefore, our focus here is exclusively on odd-order schemes. This leads to smaller spurious oscillations (around $5-7\%$ in amplitude) appearing on both sides of the discontinuity and having a much smaller spatial extent. The width $w(t)$ of the "discontinuous region" is related to the formal accuracy p in smooth regions, following the important result $w(t) \propto t^{1/(p+1)}$, although the constant in this relationship is influenced by the extent of the stencil.

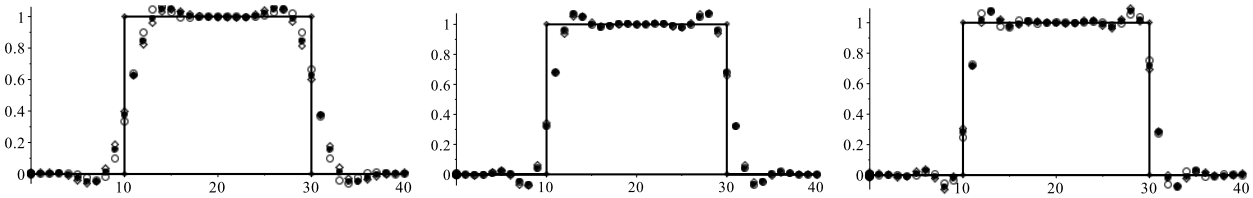

Figure 1.2: Square waves advected over twice their length, simulated using optimal finite difference schemes with 3rd, 5th, and 7th order accuracy. Courant numbers of 0.25 (open circle), 0.50 (filled circle), and 0.7537 (diamond) are considered.

Results presented in Figure 1.2 exhibit remarkable insensitivity to the Courant number, with many symbols overlapping. As anticipated, the profiles become narrower as the order of accuracy increases, although the improvement from 5th order to 7th order is not substantial. Moreover, the region outside the shock but contaminated by the shock remains relatively constant, possibly due to the larger stencil associated with increased accuracy. Overshoots and undershoots remain modest in all cases.

1.2.2 Stencil Enrichment

1.2.2.1 Discontinuous Galerkin

As discussed in Section 1.1.2, this method has gained recognition and has an extensive body of literature dedicated to it, although practical applications in the aerospace industry are

relatively scarce. The DG method is implemented on a simplicial mesh employing trial functions for polynomial reconstruction. Minimizing the error in the time derivative in a least-squares fashion is achieved by using the same set of functions as both trial and test functions. Typically, time-marching is accomplished using a Runge-Kutta method, and the fourth-order RK4 scheme is a common choice, even when spatial derivatives are evaluated to a higher order. This choice is justified by the usual small time steps employed for stability reasons. A Von Neumann analysis of the linear advection equation for a sine wave with frequency θ yields normalized amplification, $g(\nu,\theta)^{1/\nu}$, as depicted in Figure 1.3 for the complete space-time operation. Notably, these results differ significantly from those presented in Figure 1.1.

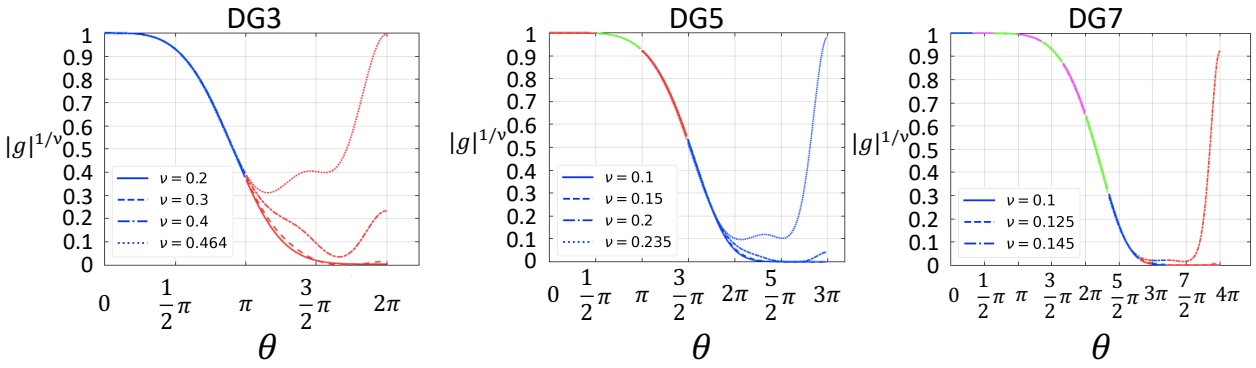

Figure 1.3: Normalized amplification of Discontinuous Galerkin schemes with order 3, 5 and 7. Note the change of horizontal scale.

One noteworthy observation is the presence of solution modes with frequencies exceeding the Shannon limit, which imposes a restriction of $\theta \leq \pi$. There has been ongoing debate [56] as to whether such modes should be considered "physical" or dismissed as "spurious". We contend that they can be both. These modes do not contribute to the formal accuracy of the method since accuracy is defined solely concerning the resolved frequencies. However, they do exist, and if they are not sufficiently damped, they can manifest in the "solution" as waves that exhibit some form of unconventional behavior. To the extent that this misbehavior is benign, it might enhance the overall "realism" of the simulation. For methods of odd order p, the upper limit of observable frequencies is $(p+1)\pi/2$. In the case of DG methods, Figure 1.3 illustrates high-frequency waves that are only weakly damped, and we will refer to these as spurious.

If we define bandwidth as the range of frequencies within which the amplitude is well preserved, a comparison between Figures 1.1 and 1.3 reveals significant improvements, with the extent of resolved frequencies extended by factors ranging between two and three. However, it's worth noting that the maximum stable Courant numbers have been reduced to

values of 0.406, 0.271, and 0.206 for orders 3, 5, and 7, respectively. This reduction can be explained by the discussion above regarding the challenges of semi-discrete methods. Additionally, when Courant numbers are just within the stable range, there are modes that are only lightly damped. This contrasts with the behavior of simple finite difference schemes, where accuracy consistently improves with increasing Courant number, becoming exact when $\nu = 1.0$ for simple linear advection. On a positive note, the left column of Figure 1.5 demonstrates significantly improved square waves. The third-order DG method is comparable to the fifth-order FDM, and the fifth-order DG method outperforms the seventh-order FDM.

1.2.2.2 Active Flux

The AF method, being a relatively recent concept, is still in the process of defining itself. Its key characteristic is the calculation of fluxes based on updates derived from the governing equations rather than relying on data interpolation. While this distinction is particularly prominent in multidimensional applications, it's essential to note that one-dimensional evolution essentially involves interpolation in characteristic variables. In this context, we present the one-dimensional version as proposed in [25]. Additionally, other high-order extensions in one dimension have been explored by Abgrall and Barsukov [57].

The normalized amplification factors for the Active Flux method are presented in Figure 1.4. Similar to the DG method, this approach significantly expands the range of accurately resolved frequencies.

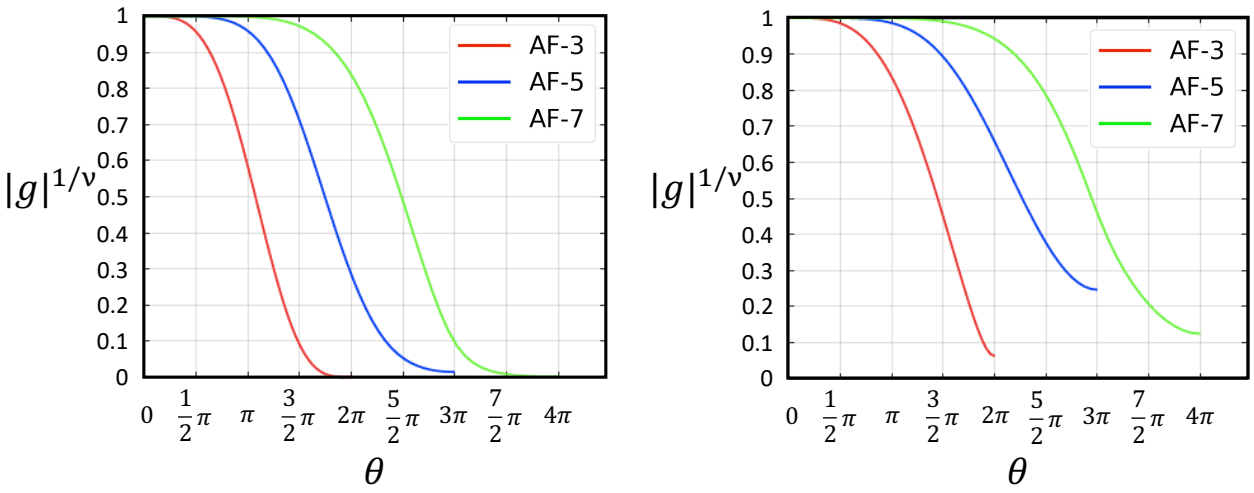

Figure 1.4: Normalized amplification factors for Active Flux schemes. **left:** $\nu = 0.25$ and **right:** $\nu = 0.75$.

To provide a more detailed comparison, Table 1.2 is included, indicating the points required per wavelength to meet the stringent criterion of less than one part in a thousand

for each cell crossed. This improvement over the simple finite difference method (Table 1.1) ranges from two to threefold. In fact, the third-order scheme performs comparably to the fifth-order finite difference scheme, while the fifth-order version is substantially superior to the seventh-order finite difference scheme. We believe that these results are indicative of the trade-off between mesh enrichment and refinement in similar comparisons.

Order	$\boldsymbol{\nu = 0.25}$	$\boldsymbol{\nu = 0.50}$	$\boldsymbol{\nu = 0.75}$
3	10.7	9.5	8.2
5	4.0	3.8	3.2
7	2.2	1.9	1.8

Table 1.2: Number of points per wavelength necessary to maintain amplitude within 0.1% per wavelength of travel for three Active Flux schemes.

The unexpectedly good results for the square wave in the right-hand column of Fig. 1.5 might be surprising. There is a common misconception that discontinuous reconstructions are favorable when dealing with true discontinuities in the solutions. However, Roe has addressed this misconception in [33]. It is clarified that discontinuous reconstruction offers no advantage in one-dimensional computations (unless the true discontinuity aligns with an interface) and is, in fact, detrimental in higher dimensions since it imposes simplistic one-dimensional physics.

The results presented for AF method in Figure 1.5 demonstrate a high level of compactness, with minimal contamination outside of the square wave. While we haven't displayed those results, a similar pattern emerges for weakly nonlinear shocks, as seen, for instance, in the far field of a sonic boom. This suggests the potential for computing such flows effectively without the need for limiter mechanisms.

1.3 Element Enrichment: Sources of Additional Information

As explored in Section 1.2, the journey toward higher-order methods involves the enrichment of elements to achieve compactness and higher frequency resolution. Now, the question arises: What are the various sources of information that can be incorporated to enrich the element for reconstruction? Traditionally, one approach is to define an element that provides additional solution values as degrees of freedom at various locations within the element. This can include the element average. The inclusion of element average among the degrees of freedom is a favorable choice for the Active Flux method, as discussed in Sections 3.3.1.4

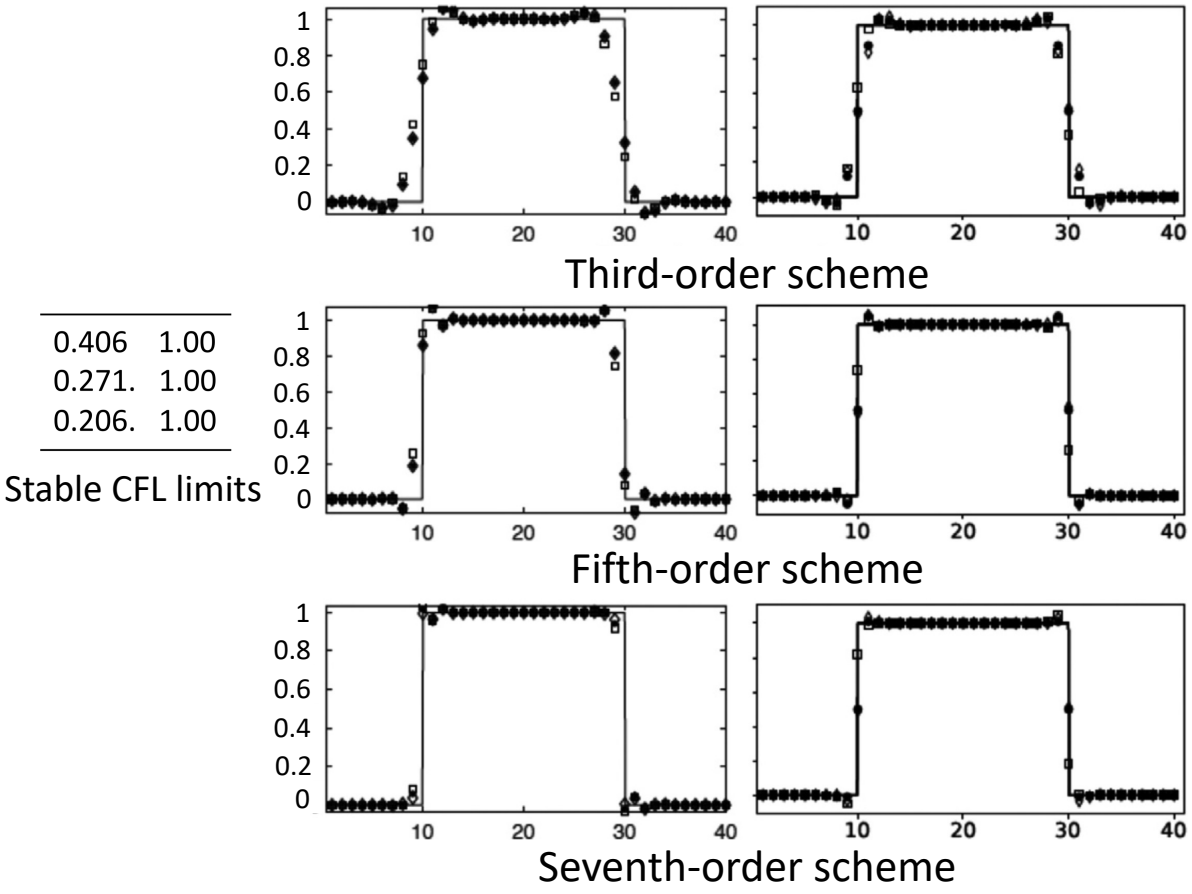

Figure 1.5: Results for a square wave advected over twice its length using (left) the Discontinuous Galerkin method and (right) the Active Flux method at three different Courant numbers. Open circle: $\nu = 0.25$, Solid circle: $\nu = 0.5$, Open diamond: $\nu = 0.75$. Note that the open circles are nearly concealed by the solid ones.

and 3.3.2.4, where it aids in straightforwardly enforcing conservation. However, achieving the element average as one of the degrees of freedom is not always feasible due to the requirement of symmetry within the degrees of freedom, which will be elaborated upon in Section 2.3.

Expanding the range of information locations within the element is not advisable when working with Active Flux, primarily because the introduction of new locations necessitates updates, thereby reducing the stability limits for these updates. Instead, an alternative approach involves incorporating different types of information at the same locations within the element, such as an arbitrary order gradient, which gives rise to what is referred to as the Hermite element. These elements are not a recent development in finite element theory and can be traced back to at least the 1970s [58]. They have been extensively explored in one space dimension [59] for solving ordinary differential equations.

Hermite methods in higher dimensions were initially introduced by Goodrich [60]. These techniques combine gradient-based interpolation with dual grids to create stable, high-order accurate approaches for solving hyperbolic problems. Vargas et al. [61] developed three variations of these methods specifically designed for periodic problems, eliminating the need for time evolution on dual grids. Additionally, Hermite methods can be combined with DG methods to enhance geometric adaptability [62]. However, it is worth noting that there are limited instances of such methods in higher dimensions, and none of them align precisely with the elements utilized in this thesis.

1.4 Thesis Outsets

Drawing from these guiding principles outlined in the previous sections, this dissertation introduces an effective strategy, known as the Hermite Active Flux method for tackling wave propagation problems when dealing with coarse grids. Currently, this approach is primarily applied within the context of multimaterial wave propagation, where linear equations with non-constant coefficients govern the behavior of waves. These multidimensional schemes are founded on the generalization proposed by Fan and Roe [63] of Poisson's solution for the initial-value problem associated with the scalar wave equation [64].

Chapter 2 introduces a comprehensive concept for defining elements in an arbitrary dimension and accuracy. This concept is pivotal for discretizing the domain of interest into a grid, a fundamental step for numerically solving general physics problems. Importantly, this foundation is fully unstructured, making it suitable for application in irregular and complex geometries.

The groundwork laid in this chapter serves as the basis for the development presented in Chapter 3, where a linear fifth-order Hermite algorithm is constructed for the acoustic

component of the Euler equations. Notably, this algorithm addresses challenges related to remote boundaries and material interfaces, automatically.

In Chapter 4, the Elastodynamic wave equations are decomposed into two distinct wave systems. These two wave systems exhibit similarities to acoustic equations and are fully decoupled, except at the boundaries. The solutions are obtained using the methodology outlined in Chapter 3.

In conclusion, Chapter 5 of the dissertation summarizes the key findings and insights, offering suggestions for potential avenues of future research.

CHAPTER 2

Advancing Accuracy: Exploring Arbitrary Order of Accuracy and Hermite Elements in Various Dimensions

An element in the finite element method is a geometric entity or subdomain that represents a portion of the overall domain or structure under consideration. It is characterized by its shape, size, and mathematical formulation, and serves as a building block for discretizing the problem domain into smaller, manageable regions.

Each element typically possesses certain properties and attributes, including geometry, topology, and material properties, which are essential for accurately representing the behavior of the system being analyzed. These information components are often defined or approximated within the element using interpolation or basis (shape) functions, allowing the element to represent a specific portion of the domain.

The selection of the element type relies on the specific problem at hand and the desired level of accuracy for the analysis. In the finite element method, commonly employed element types for two-dimensional problems include triangles and quadrilaterals, while for three-dimensional problems, tetrahedra, hexahedra (cubes), and prisms are commonly utilized. It is worth noting that the concept of element types extends beyond three dimensions, allowing for the definition of elements in higher dimensions such as pentachorons or 5-cells in four and hexaterons or 6-cells in five dimensions. The method developed in this thesis is not a finite-element method, but it has been found helpful to take a similarly careful approach to the meaning of the numbers that a code produces. We will use elements, but not in conventional ways.

By discretizing the problem domain into elements and solving the governing equations within each element, the finite element method allows for an efficient and accurate approximation of the system's behavior, making it a widely used numerical technique in various fields, including structural analysis, heat transfer, fluid dynamics, and electromagnetics. We

hope to achieve a similar versatility

In this chapter, we start by introducing a general concept of "element" and its extension into arbitrary dimensions, along with the flexibility of reconstructing it to any desired order. Subsequently, we delve into the reconstruction of elements in one-, two-, and three-space dimensions. Finally, we conclude the chapter with a discussion on grid definition, which encompasses a collection of interconnected elements.

2.1 Element Definition

In the context of practical applications, an element is commonly characterized as a collection of nodes or vertices that play a crucial role in shaping and establishing connectivity within the element. These nodes serve as reference points, offering the required degrees of freedom essential for solving the governing equations associated with the problem formulated within the element. Notably, nodes can be regarded as zero-dimensional entities, capable of being precisely defined through the utilization of the following code snippet:

```
class Node:
    def __init__(self, vector, property):
        self.vector = vector
        self.property = property
```

In this snippet, a "node" or "zero-dimensional" element is defined within an n-dimensional space partly by using a one-dimensional vector of length n, that represents the location of the corresponding element. A node is not useful unless it also has properties. These properties are encapsulated within a one-dimensional vector of variable length, which scales according to the number of properties defined for the node. These encompass, though are not confined to, properties like point values of distinct information, gradients of information up to any order such as those seen in Hermite elements, material characteristics, and more. Subsequently, these properties contribute to the information reconstruction process within non-zero-dimensional elements where the node participates. It is noteworthy that a zero-dimensional element inherently exhibits full accuracy since there is no requirement for interpolation or reconstruction to determine values within the element.

Let's define an m-dimensional element through an array possessing a length of $m + 1$. Within this array, the entry $i = 0, 1, \cdots, m$, represents a collection of i-dimensional elements termed "sub-elements". These sub-elements collectively amalgamate to form successively higher-dimensional constructs, culminating in the original m-dimensional element. The initial definition of a zero-dimensional element or node, serves as the foundational step. This

method fundamentally furnishes a methodologically organized approach to apprehend the intricate constitution of elements across diverse dimensions.

Lemma 1. *Let n and m be positive integers such that $n \geq m > 0$. In an n-dimensional space, a minimum of $m + 1$ linearly independent nodes is necessary to construct a valid m-dimensional element.*

Proof. Consider an m-dimensional element in an n-dimensional space. To construct such an element, we need a basis consisting of m linearly independent vectors to span its subspace. By the definition of a basis, the number of linearly independent vectors in any basis is equal to the dimension of the subspace.

Assume, for the sake of contradiction, that we can construct a valid m-dimensional element using fewer than $m + 1$ linearly independent nodes. This implies the existence of a set of m nodes that can define the m-dimensional element.

However, this contradicts the requirement of having a basis with m linearly independent vectors, as $m < m + 1$. Hence, it is necessary to have at least $m + 1$ linearly independent nodes in an n-dimensional space to construct a valid m-dimensional element. □

Theorem 1. *Let E be an m-dimensional element constructed from $m + 1$ nodes in n-dimensional space, where $n \geq m \geq 0$. Then the element E has $\binom{m+1}{k+1}$, k-dimensional sub-element for $0 \leq k \leq m$.*

Proof. We define the sub-elements of E by choosing $k + 1$ nodes from the $m + 1$ available nodes, where $0 \leq k \leq m$. Each combination of $k + 1$ nodes forms a unique k-dimensional sub-element of E.

The number of ways to choose $k + 1$ nodes from $m + 1$ nodes is given by the binomial coefficient $\binom{m+1}{k+1}$.

Therefore, $\binom{m+1}{k+1}$ represents the number of distinct k-dimensional sub-elements that can be formed from E.

Hence, we have proved that an m-dimensional element E constructed from $m + 1$ nodes in an n-dimensional space, where $n \geq m > 0$, has $\binom{m+1}{k+1}$, k-dimensional sub-elements for $0 \leq k \leq m$. □

2.2 Arbitrary-Dimensional Elements

In order to construct elements of arbitrary dimensions, nodes, which are zero-dimensional elements, are utilized. As stated in Lemma 1, a minimum of $m + 1$ nodes is required to construct an m-dimensional element for $m > 0$.

The following code snippet defines a class called "Element" which represents an arbitrary-dimensional element. It takes a list of nodes as input during initialization and determines the dimension of the element based on the number of nodes. Additionally, it calculates the faces of the element using the "combination" function, which returns all unique combinations of m nodes of the element (see Theorem 1). It should be noted that each node in the list must have at least m dimension(s).

```
class Element:
    def __init__(self, nodes):
        self.nodes = nodes
        self.dimension = len(nodes) - 1
        self.faces = combination(nodes, self.dimension)
```

Nodes within an element serve as degrees of freedom, allowing for the interpolation of information within the element. Typically, this is achieved by reconstructing a polynomial of degree p within the element. The nodes act as reference or control points for the polynomial interpolation, enabling the accurate representation and approximation of the desired information or function within the element.

Lemma 2. *For a polynomial of order p in n dimensions, the degree of freedom is given by the multinomial coefficient $\binom{p+n}{p}$.*

Proof. Consider a polynomial of the form:

$$P(x_1, x_2, \ldots, x_n) = \sum_{0 \leq p_1+p_2+\ldots+p_n \leq p} c_{p_1,p_2,\ldots,p_n} x_1^{p_1} x_2^{p_2} \ldots x_n^{p_n}$$

where $c_{p_1,p_2,\ldots,p_n}$ represents the coefficients of the polynomial.

Each coefficient $c_{p_1,p_2,\ldots,p_n}$ can be considered as a degree of freedom in the polynomial. Now, let's count the number of coefficients $c_{p_1,p_2,\ldots,p_n}$.

Consider the expansion of the complete homogeneous symmetric polynomial

$$h_p(x_1, x_2, \ldots, x_n) = \sum_{1 \leq i_1 \leq i_2 \leq \ldots \leq i_p \leq n} x_{i_1} x_{i_2} \cdots x_{i_p}$$

Introduce p additional variables $x_{n+1}, x_{n+2}, \ldots, x_{n+p-1}$ to ensure that there are exactly p variables in each monomial.

Now, think of distributing p identical stars (representing the variables) into $n+p-1$ bins (including the additional variables) using $(n-1)$ bars. The number of ways to do this is given by the binomial coefficient $\binom{n+p-1}{p}$.

The stars and bars argument ensures that each distribution corresponds to a unique monomial in the complete homogeneous symmetric polynomial, and vice versa.

To determine the count of coefficients $c_{p_1,p_2,\ldots,p_n}$, we enumerate the distinct monomials of degree p involving $n+1$ variables $x_0, x_1, x_2, \ldots, x_n$. Subsequently, by setting $x_0 = 1$, the total number of coefficients for the polynamial P is given by $\binom{n+p}{p}$.

Hence, the lemma is proved. □

Using Lemma 2, we can demonstrate that an m-dimensional element defined by $m+1$ nodes can only reconstruct a linear polynomial. This limitation arises from the fact that we have $m+1$ degrees of freedom, which is only sufficient to reconstruct a linear polynomial in m dimension. The number of degrees of freedom corresponds to the number of coefficients that can be adjusted to define the polynomial. With $m+1$ degrees of freedom, we are able to uniquely determine a linear polynomial, but higher-order polynomials would require additional degrees of freedom to accurately represent them.

2.3 Arbitrary-Order Elements

Although increasing the number of reference points within an element leads to a higher order of accuracy, it is important to note that the order of accuracy of elements is not solely determined by the number of nodes. Rather, it is determined by the amount of information available at each reference node. In other words, the accuracy of an element depends on the amount of information or data associated with each individual reference node. While increasing the number of nodes can provide more reference points for interpolation, the availability of additional information at each node is crucial for achieving higher-order accuracy. Therefore, the order of accuracy primarily relies on the quantity and quality of information associated with the reference nodes, rather than the number of nodes alone.We will refer to this as mesh *enrichment* rather than mesh refinement.

For an m-dimensional element to be well-defined, it is mandatory to have at least $m+1$ degrees of freedom. However, in order to achieve an arbitrary order of accuracy for an m-dimensional element, we require a total of $\binom{p+m}{p}$ pieces of information. The difference, denoted as DOF_{add}, represents the additional degrees of freedom needed to construct an element of order p.

Mathematically, we can express it as:

$$DOF_{add} = \binom{p+m}{p} - (m+1) \tag{2.1}$$

The additional reference information can be distributed among the sub-elements of the original element to enhance accuracy. For example, in the case of a three-dimensional element, this information can be allocated to faces, edges, or even vertices, allowing for different types of information to be defined at the same location. However, it is crucial to ensure that the information is equally distributed within each sub-element to maintain symmetry. For instance, if there are four faces (two-dimensional sub-elements) in a three-dimensional element, the extra information should be sufficient to assign equal amounts of information to each face. This requirement places limitations on the available approaches to increase the order of accuracy for arbitrary elements, as maintaining symmetry and equal distribution within the sub-elements becomes crucial.

In general, there are three possible types of information that can be utilized as element degrees of freedom:

1. **Values:** Solution's specific values at individual nodes within the element.

2. **Gradients:** Arbitrary order gradients of solution at individual nodes.

3. **Averages:** Spatial average of solution within individual sub-elements[1].

The selection of each type is contingent on the nature of the problem and the availability of information locations within each sub-element. For instance, when opting for element averages as degrees of freedom, there is a single information location representing the entire element, which is the element itself.

Theorem 2. *Let list* $= [x_1, x_2, ..., x_k]$ *be an arbitrary list of positive integers, and let* n *be the target sum we want to obtain. We define the function* $f(n, n_{last})$ *that counts the number of distinct ways to obtain the sum* n *by adding combinations of numbers from the list without considering permutations. The parameter* n_{last} *ensures that we only use the same or larger numbers in subsequent calls, thereby avoiding counting permutations of the same combination.*

The function f *can be represented mathematically as follows:*

$$f(n, n_{last}) = \begin{cases} 1, & \text{if } n = 0 \\ 0, & \text{if } n < 0 \\ \sum_{i=1}^{k} f(n - x_i, x_i), & \text{otherwise} \end{cases}$$

[1]In the case of a zero-dimensional sub-element, this simplifies to the "value" type because the element average of a node is identical to the individual value of that node.

Proof. We will prove the correctness of the function f using mathematical induction.

Base Cases:

For $n = 0$, there is only one way to obtain the sum. Therefore, $f(0, n_{last}) = 1$.

For $n < 0$, it is not possible to obtain a non-negative sum. Hence, $f(n, n_{last}) = 0$.

Inductive Step:

Assuming the function works correctly for all values up to n, we will show that it also works for $n + 1$.

Let $list = [x_1, x_2, ..., x_k]$ be the list of numbers.

For $n + 1$, we iterate over the numbers in the list. If the current number x_i is greater than or equal to n_{last}, we recursively call $f(n - x_i, x_i)$. This ensures that we only consider numbers that are the same or larger than n_{last}, thus avoiding counting permutations of the same combination.

By applying this logic, the function $f(n, n_{last})$ will correctly count the number of distinct ways to obtain the target sum n by adding combinations of numbers from the given list without considering permutations.

Hence, the function f is correct for any arbitrary list of positive integers and target sum. □

Theorem 1 demonstrates that the number of k-dimensional sub-elements within an arbitrary m-dimensional element, constructed using $m + 1$ nodes, is given by $\binom{m+1}{k+1}$, where $0 \leq k \leq m$. It offers a set of fundamental integers that can be utilized to determine the number of potential ways to enhance the element's order of accuracy.

In our pursuit of increasing the order of accuracy, we recognize the significance of symmetry as a crucial property. Hence, we are exploring various methods to distribute the additional degrees of freedom (DOF_{add}) among the sub-elements. This entails seeking one of the many possible ways to distribute the number of sub-elements such that it sums up to DOF_{add}. Understanding these limitations is vital, as it allows us to recognize scenarios where the degrees of freedom cannot be evenly distributed among certain sub-elements, thereby violating the symmetry requirement. This result provides a foundational understanding of the combinatorial possibilities inherent in the element's structure.

The information associated with each node in an m-dimensional element is utilized to interpolate the properties within the element. This is typically performed by a set of basis functions $B_p = \{b_i\}$ that form a complete set of polynomials of degree p. Here, B_p has $\binom{p+n}{p}$ members . Property q is then reconstructed by the projection of data onto B_p (see

appendix A).

$$q = \sum_{i=1}^{\binom{p+n}{p}} c_i b_i \tag{2.2}$$

where c_i is the coefficient corresponding to the basis function b_i.

2.4 One-Dimensional Elements

A one-dimensional linear element comprises two nodes, namely x_1 and x_2, where x_2 is greater than x_1. In this context, we are examining a one-dimensional element which exists within a one-dimensional space ($m = n$) represented by x. To simplify matters, the element is transformed from the physical space x to the reference space ξ using the following equation (refer to figure 2.1):

$$\xi = \frac{x - x_1}{x_2 - x_1} = \frac{1}{\Delta x}(x - x_1) \tag{2.3}$$

here, $\Delta x = x_2 - x_1$ denotes the length of the element.

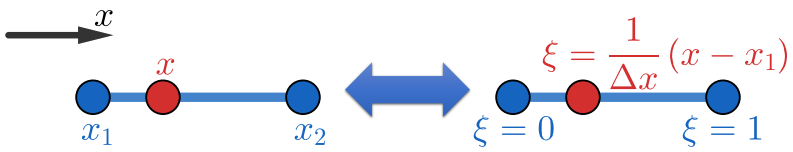

Figure 2.1: Mapping from physical space to reference space for a one-dimensional element.

Within the element, in order to achieve p-th order accuracy in interpolating properties, we need $p + 1$ pieces of information to be available. As outlined in Theorem 2, there are multiple approaches to accomplish this.

A traditional approach includes creating a stencil that integrates property values at $p+1$ evenly spaced and distinct locations, as demonstrated in Figure 2.2 (consult table 2.1 for related coefficients and basis functions). However, a challenge arises when using this method to attain high values of p. The expanded stencil can extend well beyond the actual domain of dependence, unless extremely small time steps are utilized. This issue is further compounded when employing iterative time-stepping techniques, like the Runge-Kutta method.

The Hermite element provides the required information in different forms, for example as derivatives of the properties [2], perhaps at the same locations as the values, as shown in Figure 2.3 (refer to table 2.2 for coefficients and basis functions).

[2]High-order moments of the properties are used in [48]

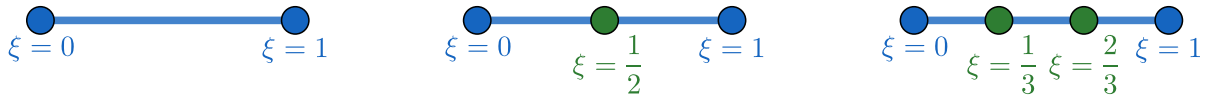

(a) $p = 1$ (b) $p = 2$ (c) $p = 3$

Figure 2.2: Information placement for a one-dimensional element.

Index	c_i	b_i
1	$q_{(\xi=0)}$	$1 - \xi$
2	$q_{(\xi=1)}$	ξ

(a) $p = 1$

Index	c_i	b_i
1	$q_{(\xi=0)}$	$1 - 3\xi + 2\xi^2$
2	$q_{(\xi=1/2)}$	$4\xi - 4\xi^2$
3	$q_{(\xi=1)}$	$-\xi + 2\xi^2$

(b) $p = 2$

Index	c_i	b_i
1	$q_{(\xi=0)}$	$1 - 5.5\xi + 9\xi^2 - 4.5\xi^3$
2	$q_{(\xi=1/3)}$	$9\xi - 22.5\xi^2 + 13.5\xi^3$
3	$q_{(\xi=2/3)}$	$-4.5\xi + 18\xi^2 - 13.5\xi^3$
4	$q_{(\xi=1)}$	$\xi - 4.5\xi^2 + 4.5\xi^3$

(c) $p = 3$

Table 2.1: Basis functions and coefficients for one-dimensional element reconstruction.

The order of accuracy of elements is determined by the amount of information available at each node, rather than solely by the number of nodes. For instance, a one-dimensional element with three nodes consists of two nodes located at each end and one in the middle. In this case, the value at the middle node and the first K derivatives (including the zeroth derivative) at each end (denoted as $\partial_k, k = 0 \ldots K$, where k ranges from 0 to K) are used together to reconstruct the element. This reconstruction allows for a polynomial approximation of order $3 + 2K$ within the element.

In principle, the required amount of information can be provided in almost any combina-

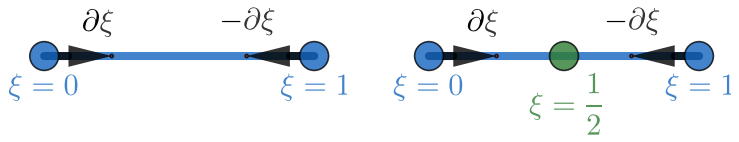

(a) $p = 3$ (b) $p = 4$

Figure 2.3: Hermitian information placement for a one-dimensional element.

Index	c_i	b_i
1	$q_{(\xi=0)}$	$1 - 3\xi^2 + 2\xi^3$
2	$q_{\xi(\xi=0)}$	$\xi - 2\xi^2 + \xi^3$
3	$q_{(\xi=1)}$	$3\xi^2 - 2\xi^3$
4	$-q_{\xi(\xi=1)}$	$\xi^2 - \xi^3$

(a) $p = 3$

Index	c_i	b_i
1	$q_{(\xi=0)}$	$1 - 11\xi^2 + 18\xi^3 - 8\xi^4$
2	$q_{\xi(\xi=0)}$	$\xi - 4\xi^2 + 5\xi^3 - 2\xi^4$
3	$q_{(\xi=1/2)}$	$16\xi^2 - 32\xi^3 + 16\xi^4$
4	$q_{(\xi=1)}$	$-5\xi^2 + 14\xi^3 - 8\xi^4$
5	$-q_{\xi(\xi=1)}$	$-\xi^2 + 3\xi^3 - 2\xi^4$

(b) $p = 4$

Table 2.2: Hermitian basis functions and coefficients for one-dimensional reconstruction.

tion, although at least one value must be given (or else there is no way to define conservation) and at least two locations must be used. In [65] three solution values and two solution gradients were combined to give fourth-order reconstructions ($p = 4$) and this has become somewhat standard in H-WENO methods.

It will not be attempted in this thesis to compare and evaluate every possibility. Heuristic considerations [25], such as compactness and centering with respect to the required information, are used to select a few promising possibilities. These are mostly analyzed in forms that could be of practical use, but sometimes in a simple context, more extreme possibilities will be explored.

2.5 Two-Dimensional Elements

A linear two-dimensional element is formed by three nodes, as illustrated in Figure 2.4, using a barycentric coordinate system. The adoption of this coordinate system ensures stability by virtue of providing a more orthogonal basis, as explained in Section 2.7.

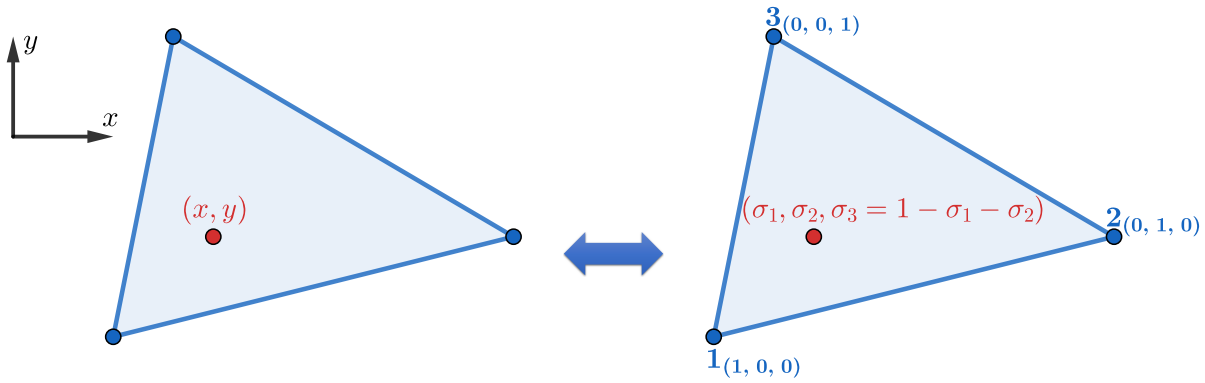

Figure 2.4: Barycentric representation of a two-dimensional triangular element.

The transformation from barycentric coordinates $\boldsymbol{\sigma} = (\sigma_1, \sigma_2, \sigma_3)^T$ to physical space co-

ordinates $\boldsymbol{x} = (x, y)^T$ is expressed as:

$$\boldsymbol{R\sigma} = \boldsymbol{x}, \tag{2.4}$$

where $\boldsymbol{R} = [\boldsymbol{r}_1|\boldsymbol{r}_2|\boldsymbol{r}_3]$ is the relation matrix with $\boldsymbol{r}_i = (x_i, y_i)^T$ representing the Cartesian coordinates of the triangle vertices. To ensure a unique and normalized conversion, the barycentric coordinates must satisfy the condition $\sigma_1 + \sigma_2 + \sigma_3 = 1$. This condition modifies the conversion relation to:

$$[1|\boldsymbol{R}^T]^T\boldsymbol{\sigma} = [1|\boldsymbol{x}^T]^T \longrightarrow \begin{bmatrix} 1 & 1 & 1 \\ x_1 & x_2 & x_3 \\ y_1 & y_2 & y_3 \end{bmatrix} \begin{pmatrix} \sigma_1 \\ \sigma_2 \\ \sigma_3 \end{pmatrix} = \begin{pmatrix} 1 \\ x \\ y \end{pmatrix} \tag{2.5}$$

The barycentric coordinates are thus the solution of the linear system

$$\begin{pmatrix} \sigma_1 \\ \sigma_2 \\ \sigma_3 \end{pmatrix} = \frac{1}{2A} \begin{bmatrix} x_2y_3 - x_3y_2 & y_2 - y_3 & x_3 - x_2 \\ x_3y_1 - x_1y_3 & y_3 - y_1 & x_1 - x_3 \\ x_1y_2 - x_2y_1 & y_1 - y_2 & x_2 - x_1 \end{bmatrix} \begin{pmatrix} 1 \\ x \\ y \end{pmatrix} \tag{2.6}$$

where $2A = \det\left([1|\boldsymbol{R}^T]^T\right) = x_1(y_2 - y_3) + x_2(y_3 - y_1) + x_3(y_1 - y_2)$ is twice the signed area of the triangle.

To improve the accuracy of an element, Eq. 2.1 suggests incorporating supplementary information while preserving symmetry in the degrees of freedom (i.e., maintaining the same degrees of freedom per sub-element). This concept is depicted in figures 2.5 and 2.6 for a two-dimensional element.

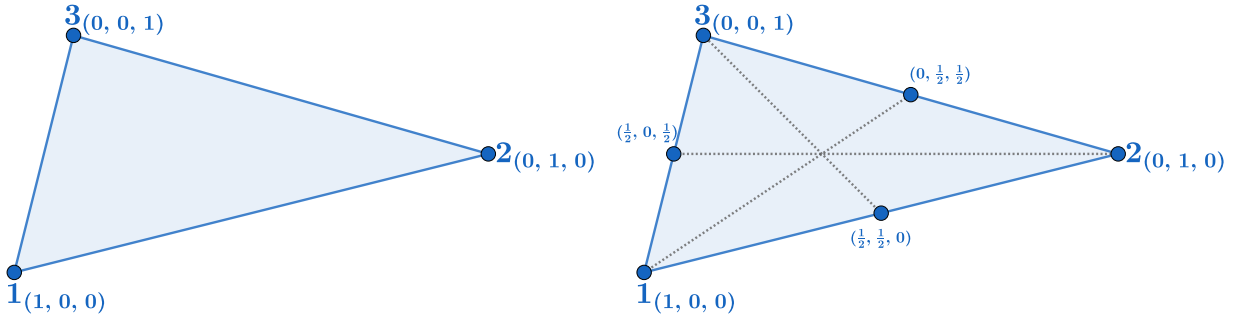

(a) $p = 1$ (b) $p = 2$

Figure 2.5: Information placement of a two-dimensional element.

In the context of a two-dimensional element, we encounter a noteworthy constraint in our attempts to enhance the accuracy. Lemma 1 establishes that a minimum of three nodes

Index	c_i	b_i
1	$q_{(1,0,0)}$	σ_1
2	$q_{(0,1,0)}$	σ_2
3	$q_{(0,0,1)}$	σ_3

(a) $p = 1$

Index	c_i	b_i
1	$q_{(1,0,0)}$	$\sigma_1^2 - \sigma_1(\sigma_2 + \sigma_3)$
2	$q_{(1/2,1/2,0)}$	$4\sigma_1\sigma_2$
3	$q_{(0,1,0)}$	$\sigma_2^2 - \sigma_2(\sigma_1 + \sigma_3)$
4	$q_{(0,1/2,1/2)}$	$4\sigma_2\sigma_3$
5	$q_{(0,0,1)}$	$\sigma_3^2 - \sigma_3(\sigma_1 + \sigma_2)$
6	$q_{(1/2,0,1/2)}$	$4\sigma_1\sigma_3$

(b) $p = 2$

Table 2.3: Coefficients and basis functions for two-dimensional reconstruction.

	c_i	b_i
Vertex v	q_v	$\sigma_v^2 + 2\sigma_v(\sigma_w + \sigma_x) - 2\sigma_w\sigma_x$
	Sq_v	$\sigma_v(\sigma_w + \sigma_x) - \sigma_w\sigma_x$

(a) $p = 2$

	c_i	b_i
Vertex v	q_v	$\sigma_v^4 + 4\sigma_v^2[\sigma_v(\sigma_w + \sigma_x) - \sigma_w\sigma_x] - 5\sigma_v^2(\sigma_w^2 + \sigma_x^2)$
	$Sq_{v\to w}$	$\sigma_v^3\sigma_w - 0.5\sigma_v\sigma_w\sigma_x(\sigma_v - \sigma_w + \sigma_x) - \sigma_v^2\sigma_w^2$
Midpoint vw	q_{vw}	$16\sigma_v\sigma_w\sigma_x(\sigma_v + \sigma_w - \sigma_x) + 16\sigma_v^2\sigma_w^2$
	Sq_{vw}	$4\sigma_v\sigma_w\sigma_x(\sigma_x + \sigma_w - \sigma_x)$

(b) $p = 4$

Table 2.4: Coefficients and basis functions for two-dimensional hermitian reconstruction. The values of c_i can be found in figure 2.6.

is necessary to construct a linear element ($p = 1$). To achieve a higher order of accuracy i.e., $p = 2$, we require an additional DOF_{add} of $6 - 3 = 3$. Preserving symmetry mandates the equal distribution of these three additional degrees of freedom among all sub-elements. However, since the number of sub-elements is either one (representing the two-dimensional element as a whole) or three (corresponding to one- and zero-dimensional elements), adding just one extra degree of freedom to the element itself, such as an element average, would violate the symmetry requirement.

To address this challenge, two approaches are illustrated in Figure 2.5b and Figure 2.6a for the scenario where $p = 2$. In the former figure, the extra degrees of freedom are distributed along the edges, while in the latter figure, they are added at the vertices in the form of gradients (Hermite element), effectively accommodating the required increase in accuracy without violating symmetry.

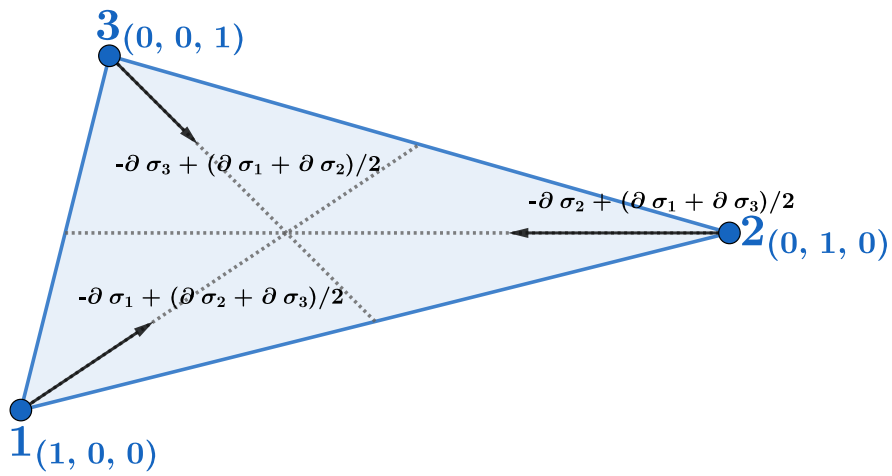

(a) $p = 2$

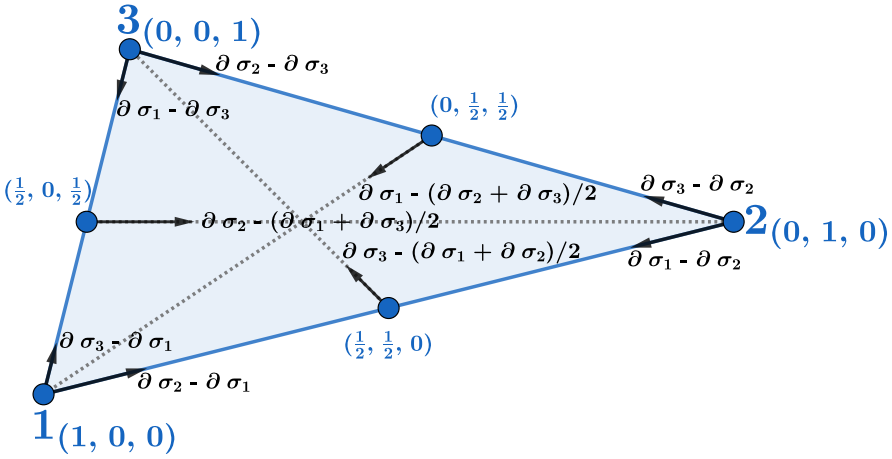

(b) $p = 4$

Figure 2.6: Hermite information placement of a two-dimensional element.

Within Hermite elements, the orientation of gradient directions is chosen deliberately to yield a streamlined algebraic formulation for expressing the basis functions. This decision leads to reduced computational overhead during basis function computations. For instance, consider the element shown in Figure 2.6b. Initially, the approach involved imposing normal gradients at each midpoint, aiming to ensure consistent normal gradients along all edges to enhance continuity. However, this approach resulted in complex algebraic expressions. Consequently, we opted to prescribe the gradient along the median of the element, yielding more manageable algebraic manipulation.

Table 2.3 and 2.4 present the associated coefficients and basis functions for each element reconstruction. Refer to appendix A for a detailed explanation of the derivation.

2.6 Three-Dimensional Elements

Transitioning to higher dimensions introduces a greater consideration of realistic problems, simultaneously leading to an exponential growth in the complexity of the underlying foundations.

A three-dimensional element, depicted in Figure 2.7, is formed by four nodes and represented using a barycentric coordinate system.

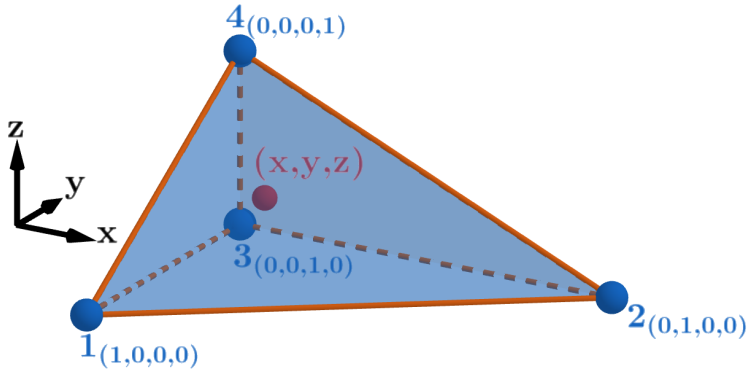

Figure 2.7: Barycentric representation of a three-dimensional element. A point in physical space, denoted as $\boldsymbol{x} = (x, y, z)$, is represented using barycentric coordinates $\boldsymbol{\sigma} = (\sigma_1, \sigma_2, \sigma_3, \sigma_4)$, satisfying the constraint $\sigma_1 + \sigma_2 + \sigma_3 + \sigma_4 = 1$.

Similarly, as demonstrated in Equation 2.4, for a three-dimensional element, the transformation from barycentric coordinates $\boldsymbol{\sigma} = (\sigma_1, \sigma_2, \sigma_3, \sigma_4)^T$ to physical space coordinates $\boldsymbol{x} = (x, y, z)^T$ is expressed as

$$[1|\boldsymbol{R}^T]^T\boldsymbol{\sigma} = [1|\boldsymbol{x}^T]^T \longrightarrow \begin{bmatrix} 1 & 1 & 1 & 1 \\ x_1 & x_2 & x_3 & x_4 \\ y_1 & y_2 & y_3 & y_4 \\ z_1 & z_2 & z_3 & z_4 \end{bmatrix} \begin{pmatrix} \sigma_1 \\ \sigma_2 \\ \sigma_3 \\ \sigma_4 \end{pmatrix} = \begin{pmatrix} 1 \\ x \\ y \\ z \end{pmatrix} \tag{2.7}$$

where $\boldsymbol{R} = [\boldsymbol{r}_1|\boldsymbol{r}_2|\boldsymbol{r}_3|\boldsymbol{r}_4]$ is the relation matrix with $\boldsymbol{r}_i = (x_i, y_i, z_i)^T$ representing the Cartesian coordinates of the four vertices of the three-dimensional element. The barycentric coordinates σ_1, σ_2, σ_3, and σ_4 satisfy the constraint $\sigma_1 + \sigma_2 + \sigma_3 + \sigma_4 = 1$.

Improving the accuracy of higher-dimensional elements presents greater challenges due to the increased degrees of freedom and the growing number of sub-elements, as indicated by Lemma 2 and Theorem 1. This complexity makes it more difficult to assign the additional degrees of freedom DOF_{add} in Equation 2.1 equally without violating the symmetry. Figure 2.8 demonstrates three-dimensional elements exhibiting higher accuracy.

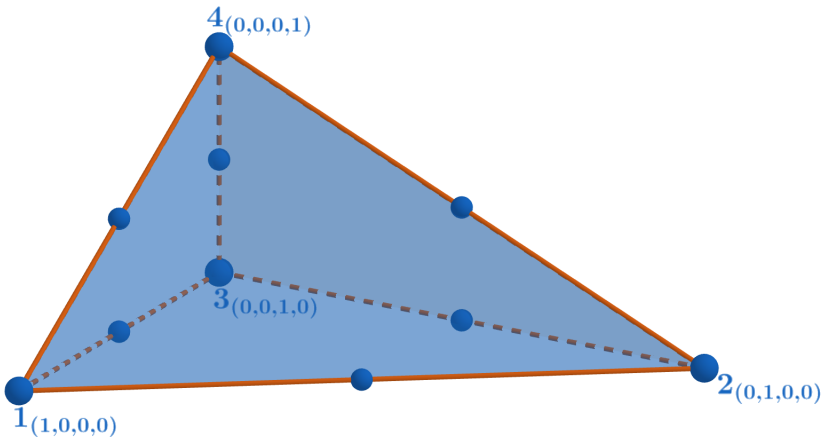

(a) $p = 2$

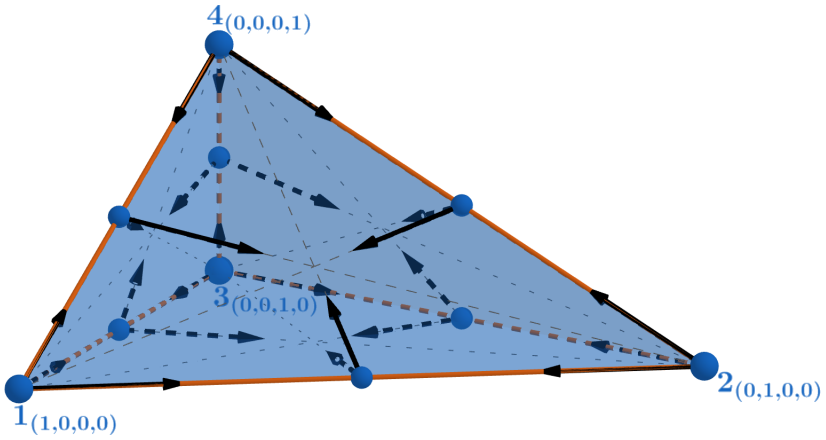

(b) $p = 4$

Figure 2.8: Information placement within a three-dimensional element. For $p = 4$, an additional degree of freedom exists, representing the element average. Gradients are indicated by black arrows. Refer to table 2.5 for the corresponding values.

Table 2.6 displays the corresponding basis functions and coefficients for the three-dimensional elements depicted in this figure (see appendix A for derivation).

2.7 Numerical Sensitivity

Numerical sensitivity plays a pivotal role in assessing the impact of even slight discrepancies within the data on the intricacies of the reconstruction process. It not only provides a metric for measuring the extent of such influences but also serves as a discerning gauge to determine the susceptibility of the reconstruction to the presence of inaccuracies embedded within the data. In essence, numerical sensitivity unravels the intricate relationship between

	Information	$\boldsymbol{c_i}$
Vertex v	q_v	q_v
	$Sq_{v\to w}$	$(\partial\sigma_w - \partial\sigma_v)_{(q_v)}$
Midpoint vw**, triangle** vwx	q_{vw}	q_{vw}
	Sq_{vw}	$[\partial\sigma_x - (\partial\sigma_v + \partial\sigma_w)/2]_{(q_{vw})}$

Table 2.5: Coefficients for information placement within a three-dimensional element ($p = 4$).

	$\boldsymbol{c}_i$	$\boldsymbol{b_i}$
Vertex v	q_v	$\sigma_v^2 - \sigma_v(\sigma_w + \sigma_x + \sigma_y)$
Midpoint vw	q_{vw}	$4\sigma_v\sigma_w$

(a) $p = 2$

	$\boldsymbol{c_i}$	$\boldsymbol{b_i}$
Vertex v	q_v	$\sigma_v^4 + 4\sigma_v^3(\sigma_w + \sigma_x + \sigma_y) - 5\sigma_v^2(\sigma_w^2 + \sigma_x^2 + \sigma_y^2)$ $- 4\sigma_v^2(\sigma_w\sigma_x + \sigma_w\sigma_y + \sigma_x\sigma_y) - 12\sigma_v\sigma_w\sigma_x\sigma_y$
	$Sq_{v\to w}$	$\sigma_v^3\sigma_w - \sigma_v^2\sigma_w^2 - 0.5(\sigma_x + \sigma_y)(\sigma_v^2\sigma_w - \sigma_v\sigma_w^2)$ $- 0.5\sigma_v\sigma_w(\sigma_x^2 + \sigma_y^2)$
Midpoint vw**, triangle** vwx	q_{vw}	$16\sigma_v^2\sigma_w^2 + 16(\sigma_x + \sigma_y)(\sigma_v^2\sigma_w + \sigma_v\sigma_w^2)$ $- 16\sigma_v\sigma_w(\sigma_x^2 + \sigma_y^2) - 128\sigma_v\sigma_w\sigma_x\sigma_y$
	Sq_{vw}	$4\sigma_v\sigma_w\sigma_x(\sigma_v + \sigma_w - \sigma_x) - 8\sigma_v\sigma_w\sigma_x\sigma_y$
Element Average	$\bar{q}$	$1680\sigma_v\sigma_w\sigma_x\sigma_y$

(b) $p = 4$

Table 2.6: Coefficients and basis functions for three-dimensional reconstruction. The c_i can be found in figure 2.8.

the accuracy of the reconstruction and the potential perturbations within the input data introduced by machine precision, offering valuable insights into the robustness and reliability of the overall methodology.

Equation 2.2 presents the reconstruction process for property q. This process involves projecting q onto a set of basis functions B_p, accommodating elements of arbitrary dimensions and orders.

The basis function b_i is derived through the methodology elucidated in Appendix A and is expressed as

$$b_i = \boldsymbol{\lambda}_i \cdot \boldsymbol{\varphi} \tag{2.8}$$

Here, $\boldsymbol{\lambda}_i$ signifies the reconstruction parameters vector for the ith basis function, while $\boldsymbol{\varphi}$ represents the vector of basis features, each possessing a length of $\binom{p+n}{p}$.

The inner product of the basis features across an n-dimensional domain $\mathbf{\Omega}$ is defined as

$$\langle \varphi_i, \varphi_j \rangle_{\mathbf{\Omega}} = \int \int \cdots \int_{\mathbf{\Omega}} \varphi_i \varphi_j \, d\mathbf{\Omega} \tag{2.9}$$

The collinearity between two basis features is then determined by:

$$\langle \varphi_i \parallel \varphi_j \rangle_{\mathbf{\Omega}} = \frac{|\langle \varphi_i, \varphi_j \rangle_{\mathbf{\Omega}}|}{\sqrt{\langle \varphi_i, \varphi_i \rangle_{\mathbf{\Omega}}} \sqrt{\langle \varphi_j, \varphi_j \rangle_{\mathbf{\Omega}}}} \tag{2.10}$$

Here, the value of $\langle \varphi_i \parallel \varphi_j \rangle_{\mathbf{\Omega}}$ ranges between 0 and 1, where 0 indicates that φ_i and φ_j are orthogonal, and 1 indicates that they are collinear.

A set of basis features is characterized as orthogonal if, for every $i \neq j$, the collinearity of any two distinct basis features equals zero.

$$\langle \varphi_i \parallel \varphi_j \rangle_{\mathbf{\Omega}} = 0 \quad \text{for} \quad i \neq j \tag{2.11}$$

The orthogonality of a set of basis features significantly impacts the sensitivity of reconstruction. When a set of basis functions is orthogonal, it means that the functions are mutually independent and have minimal overlap in the space they span. This property has profound implications for the accuracy and stability of reconstruction processes. While the exact orthogonality of basis features isn't a strict prerequisite for the reconstruction process, the degree of orthogonality significantly influences its stability. As the level of orthogonality decreases—reflected by increasing deviations from 0 in $\langle \varphi_i \parallel \varphi_j \rangle_{\mathbf{\Omega}}$ for $i \neq j$—the reconstruction becomes more susceptible to instability.

To illustrate this phenomenon, in one-dimensional space, within domain $\mathbf{\Omega} = [0, 1]$ consider the basis features used for reconstructing a polynomial of order p. These are in fact the monomial functions;

$$\boldsymbol{\varphi} = (1, \xi, \xi^2, \ldots, \xi^p) \tag{2.12}$$

In this context, the collinearity between features i and j within the element can be described as

$$\langle \xi^i \parallel \xi^j \rangle_{\mathbf{\Omega}} = \frac{\langle \xi^i, \xi^j \rangle_{\mathbf{\Omega}}}{\sqrt{\langle \xi^i, \xi^i \rangle_{\mathbf{\Omega}}} \sqrt{\langle \xi^j, \xi^j \rangle_{\mathbf{\Omega}}}} = \frac{\sqrt{2i+1}\sqrt{2j+1}}{1+i+j} \quad \text{for} \quad i, j = 0, 1, \cdots, p \tag{2.13}$$

As the parameter p increases, the collinearity of higher-order basis features tends to approach unity (≈ 1). This trend leads to a substantial overlap in the space covered by each individual feature, thereby causing instability in the reconstruction procedure. Put differently, the higher-order components within the features become tightly grouped, leading to a reduction

in their distinctiveness and independence. This phenomenon is visualized in Figure 2.9. From this we reach the well-known conclusion that the monomials themselves do not make a good basis for polynomial reconstruction, and this provides the motivation for the various orthogonal polynomials [66].

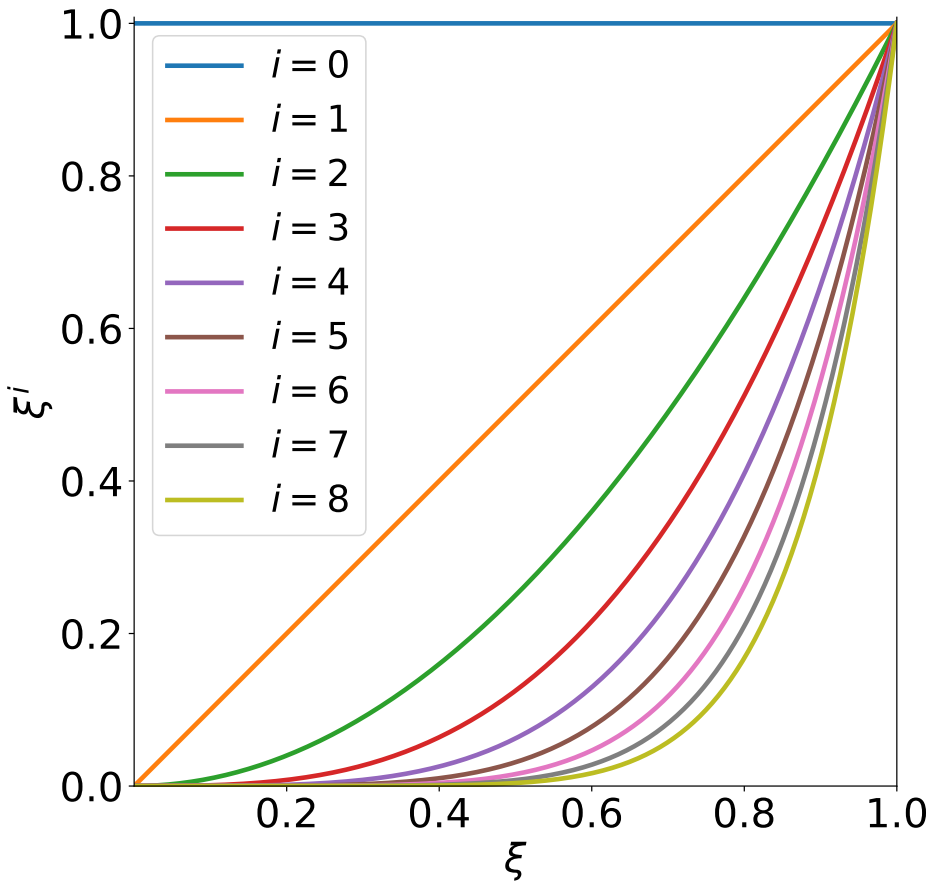

Figure 2.9: Collapse of orthogonality: Illustration of increasing collinearity with growing p.

To shed further light on this matter, we quantify how the degree of orthogonality among a set of basis features contributes to the instability of a scheme.

Resuming from Equation 2.2, which delineates the reconstruction process, we proceed by

substituting Equation 2.8 with the expression b_i, thus yielding

$$\begin{aligned} q &= \sum_{i=1}^{\binom{p+n}{p}} c_i b_i = \sum_{i=1}^{\binom{p+n}{p}} c_i \boldsymbol{\lambda}_i \cdot \boldsymbol{\varphi} = \sum_{i=1}^{\binom{p+n}{p}} \sum_{j=1}^{\binom{p+n}{p}} c_i \lambda_{ij} \varphi_j \\ &= \sum_{j=1}^{\binom{p+n}{p}} \sum_{i=1}^{\binom{p+n}{p}} c_i \lambda_{ij} \varphi_j = \sum_{j=1}^{\binom{p+n}{p}} \varphi_j \sum_{i=1}^{\binom{p+n}{p}} c_i \lambda_{ij} = \sum_{j=1}^{\binom{p+n}{p}} \lambda_j^* \varphi_j \end{aligned} \tag{2.14}$$

where

$$\lambda_j^* = \sum_{i=1}^{\binom{p+n}{p}} c_i \lambda_{ij} \tag{2.15}$$

In this expression, λ_{ij} denotes the reconstruction parameter corresponding to basis function i and feature j.

As an illustrative example, within the context of a one-dimensional space, Equation 2.14 takes on the following form

$$q(\xi) = \sum_{i=1}^{p+1} c_i b_i(\xi) = \sum_{i=0}^{p} \lambda_i^* \xi^i, \tag{2.16}$$

The reconstruction of property q on an element involves the interpolation and/or extrapolation of data within that element. The reconstruction parameters $\boldsymbol{\lambda}^*$ for this interpolation and/or extrapolation is achieved through

$$\boldsymbol{A}\boldsymbol{\lambda}^* = \boldsymbol{q} \tag{2.17}$$

where $\boldsymbol{A}$ represents the coefficient matrix and $\boldsymbol{q}$ represents the data vector. For instance, in one-dimensional space, Equation 2.17 corresponding to a second-order element ($p = 2$) can be expressed as:

$$\begin{bmatrix} 1 & 0 & 0 \\ 1 & \frac{1}{2} & \frac{1}{4} \\ 1 & 1 & 1 \end{bmatrix} \begin{pmatrix} \lambda_0^* \\ \lambda_1^* \\ \lambda_2^* \end{pmatrix} = \begin{pmatrix} q_{(\xi=0)} \\ q_{(\xi=1/2)} \\ q_{(\xi=1)} \end{pmatrix} \tag{2.18}$$

at which rows of matrix $\boldsymbol{A}$ is computed by

$$\boldsymbol{A}_{(\xi)} = \begin{bmatrix} 1 & \xi & \xi^2 \end{bmatrix} \quad \text{for} \quad \xi = 0, \frac{1}{2}, 1 \tag{2.19}$$

Equation 2.17 is solved to determine the reconstruction parameters. A reconstruction is considered well-conditioned when small errors in the data vector $\boldsymbol{q}$ lead to small variations

in the reconstruction parameters $\boldsymbol{\lambda}^*$. These errors arise due to the limitations of machine precision. However, if the reconstruction is ill-conditioned, these errors will exponentially amplify with each iteration over time.

In order to conduct a more thorough analysis of the categorization of a reconstruction as well- or ill-conditioned, we direct our attention towards elucidating the manner in which variations in the data vector $\boldsymbol{q}$ manifest within the reconstruction parameters vector $\boldsymbol{\lambda}^*$. Let's consider a perturbation in the data vector $\boldsymbol{q}$, denoted as $\Delta\boldsymbol{q}$. This perturbation leads to a corresponding change in the reconstruction parameters, denoted as $\Delta\boldsymbol{\lambda}^*$. We can express the perturbed equation as:

$$\boldsymbol{A}(\boldsymbol{\lambda}^* + \Delta\boldsymbol{\lambda}^*) = \boldsymbol{q} + \Delta\boldsymbol{q} \tag{2.20}$$

Expanding the left-hand side using the distributive property of matrix multiplication

$$\boldsymbol{A}\boldsymbol{\lambda}^* + \boldsymbol{A}\Delta\boldsymbol{\lambda}^* = \boldsymbol{q} + \Delta\boldsymbol{q} \tag{2.21}$$

Subtracting Equation 2.17 from this perturbed equation

$$\boldsymbol{A}\Delta\boldsymbol{\lambda}^* = \Delta\boldsymbol{q} \tag{2.22}$$

Now, we're interested in the relationship between the magnitudes of $\Delta\boldsymbol{q}$ and $\Delta\boldsymbol{\lambda}^*$. We'll denote the norms of these vectors as $||\Delta\boldsymbol{q}||$ and $||\Delta\boldsymbol{\lambda}^*||$, respectively.

Utilizing the properties of norms and given that matrix $\boldsymbol{A}$ is nonsingular—a necessary condition, as otherwise Equation 2.17 remains unsolvable

$$\boldsymbol{A}\boldsymbol{\lambda}^* = \boldsymbol{q} \Rightarrow ||\boldsymbol{q}|| \leq ||\boldsymbol{A}|| \cdot ||\boldsymbol{\lambda}^*|| \tag{2.23}$$

$$\boldsymbol{A}\Delta\boldsymbol{\lambda}^* = \Delta\boldsymbol{q} \Rightarrow \Delta\boldsymbol{\lambda}^* = \boldsymbol{A}^{-1}\boldsymbol{q} \Rightarrow ||\Delta\boldsymbol{\lambda}^*|| \leq ||\boldsymbol{A}^{-1}|| \cdot ||\Delta\boldsymbol{q}|| \tag{2.24}$$

By multiplying Equation 2.23 with Equation 2.24 and subsequently dividing both sides by $||\boldsymbol{q}|| \cdot ||\boldsymbol{\lambda}^*||$:

$$\frac{||\Delta\boldsymbol{\lambda}^*||}{||\boldsymbol{\lambda}^*||} \leq ||\boldsymbol{A}|| \cdot ||\boldsymbol{A}^{-1}|| \frac{||\Delta\boldsymbol{q}||}{||\boldsymbol{q}||} \tag{2.25}$$

Now, recall that the condition number of matrix $\boldsymbol{A}$ is given by $\kappa(\boldsymbol{A}) = ||\boldsymbol{A}|| \cdot ||\boldsymbol{A}^{-1}||$. Therefore:

$$\frac{||\Delta\boldsymbol{\lambda}^*||}{||\boldsymbol{\lambda}^*||} \leq \kappa(\boldsymbol{A}) \frac{||\Delta\boldsymbol{q}||}{||\boldsymbol{q}||} \tag{2.26}$$

In Equation 2.26, the value $||\Delta\boldsymbol{q}||/||\boldsymbol{q}||$ represents the relative alteration in the data, while the quantity $||\Delta\boldsymbol{\lambda}^*||/||\boldsymbol{\lambda}^*||$ signifies the ensuing relative change in the reconstruction. Utilizing relative changes holds the advantage of dimensionlessness, rendering them impervious to

overall scale factors. The inequality elucidates that the condition number functions as an amplification factor for relative errors. Perturbations in the data can lead to modifications in the reconstruction that are magnified by a factor of $\kappa(\boldsymbol{A})$. This marks the culmination of our classification of well- and ill-conditioned reconstructions. A reconstruction is labeled as well-conditioned when the condition number $\kappa(\boldsymbol{A})$ approaches 1. On the contrary, a reconstruction is deemed ill-conditioned when $\kappa(\boldsymbol{A})$ significantly exceeds 1.

Table 2.7 provides condition numbers for various one-dimensional elements, illustrating how the numerical stability exponentially deteriorates with increasing order of element accuracy. It further emphasizes that the Hermite reconstruction not only enhances the stability threshold of the numerical algorithm but also exhibits significantly better numerical stability compared to standard reconstructions on the same degree of freedom.

	Standard	**Hermitian**
$\boldsymbol{p=1}$	2.6	–
$\boldsymbol{p=2}$	15.1	–
$\boldsymbol{p=3}$	98.9	23.8
$\boldsymbol{p=4}$	686.4	283.1

Table 2.7: Condition numbers for different elements in one-dimensional space.

To address the instability linked with higher-order elements, a strategy involves applying Gram-Schmidt orthogonalization to the basis features. For instance, in the context of a quadratic reconstruction ($p = 2$) for a one-dimensional element, instead of employing $\boldsymbol{\varphi} = (1, \xi, \xi^2)$, one can opt for shifted Legendre polynomials $\boldsymbol{\varphi} = (1, 2\xi - 1, 6\xi^2 - 6\xi + 1)$ to achieve this. Nevertheless, employing this approach in higher dimensions with enhanced accuracy can lead to notable computational costs. Alternatively, using more symmetric coordinate systems such as barycentric coordinates can help reduce the condition number without incurring significant computational costs. These coordinate systems provide a more orthogonal set of basis features, leading to a reduced condition number of the reconstruction and thus greater stability. Table 2.8 presents a comparison of the condition numbers for two-dimensional Hermite triangular elements in both Cartesian and barycentric coordinate systems. In this table, it is demonstrated that for a linear reconstruction ($p = 1$), the basis functions exhibit orthogonality when employing a barycentric coordinate system. Conversely, while a Cartesian coordinate system maintains stability, it does not yield orthogonality. For quartic reconstruction ($p = 4$), the condition number in the Cartesian coordinate system surpasses that of the barycentric system by an order of magnitude. According to findings from the experiment [1], this increased condition number in the linear acoustic solver, to be discussed in Chapter 3, renders it unstable. This instability propels the adoption of the

barycentric coordinate system as the preferred choice for presenting our higher-dimensional elements.

	Cartesian	**Barycentric**
$\boldsymbol{p=1}$	3.7	1.0
$\boldsymbol{p=2}$	16.4	11.0
$\boldsymbol{p=4}$	1592.0	216.2

Table 2.8: Condition numbers for different Hermite elements in two-dimensional space.

2.8 Grids

By connecting the nodes of adjacent elements, a mesh or grid is formed, enabling the entire domain to be discretized into a collection of interconnected elements.

a system of equations can be effectively solved by leveraging a grid. Typically, these equations are derived from conservation laws, necessitating the transfer of information between adjacent elements. In this context, an element of dimensionality m is considered to have neighboring elements that share $(m-1)$-dimensional sub-elements. It is essential to note that information can only be transferred between such $(m-1)$-dimensional sub-elements. Thus, maintaining a connection between elements becomes crucial.

To achieve this, a graph data structure is constructed, representing the grid. In this graph, each element is represented as a node, and edges are defined to connect two m-dimensional elements that share an $(m-1)$-dimensional sub-element. This has been shown in figure 2.10 By organizing the problem in this manner, the efficient transfer of information and solving of the system of equations can be facilitated.

Here, the information will be updated through a graph traversal process, which demonstrates an efficient time complexity of $\mathcal{O}(n)$, where n represents the number of elements. This traversal is crucial for updating the information associated with each element. Algorithm 2.1 provides a detailed description of this efficient traversal approach.

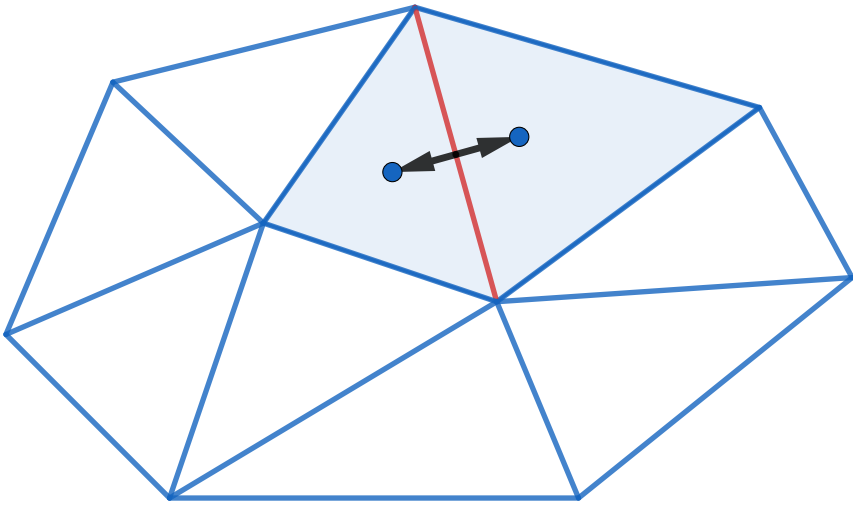

Figure 2.10: Schematic representation of a grid as a graph data structure.

Algorithm 2.1 Grid Traversal

Require: Grid G with n elements and information associated with each element.
Ensure: Updated information for all elements in the grid.

```
1: function GridDFS(element)
2: Mark element as visited.
3: Update the information associated with element.
4: for each neighbor e of element do
5:    if e is not visited then
6:       GridDFS(e)
7:    end if
8: end for
9: end function
10: GridDFS(element) {Start the recursive GridDFS from a chosen starting element.}
```

CHAPTER 3

Acoustics: Coarse Grids with a High-Order Method

The Euler equations constitute a fundamental system of three-dimensional partial differential equations that describe the dynamics of inviscid fluid flow. These equations hold significant importance in the field of fluid dynamics and find wide-ranging applications in both scientific research and engineering. In response to the complexities inherent in the Euler equations, Eymann et al. [67] have proposed an innovative approach involving the decomposition of these equations into distinct advective and acoustics components in multi-dimensional settings. Within this framework, they introduce a cutting-edge technique known as Active Flux, a promising and novel method for addressing the solution for each component.

This is predicated on the hypothesis that to ensure accuracy, and more specifically bandwidth, it is very important that all information flow is correctly modeled. Roe [25] believes that this is the way to construct schemes that enjoy wide bandwidth, which in many cases is more important than high formal accuracy. The ingredients for this are continuous reconstruction, analysis at the PDE level to a desired order, appropriate stencil choice and fully discrete timestepping. The resulting method therefore deviates from current practice in numerous ways. Since optimal stencils are very different for acoustic and advective behavior, different stencils must be used for different modes of information. The decomposition cannot be directly performed on the equations in conservation form, but can be imposed by finding the fluxes in an evolutionary manner that distinguishes the two effects. This leads to the method being called the Active Flux. Acoustic and advective effects are then computed almost independently

In this chapter, our primary focus lies in addressing the acoustics component, which presents notable challenges. Our research is dedicated to achieving heightened accuracy in numerical solutions of the acoustic equations while simultaneously maintaining the same storage requirements, thereby obviating the need for reduced timesteps. This endeavor aims to contribute to the advancement of numerical simulations in fluid dynamics, thereby

enhancing our understanding and analysis of various real-world flow situations.

3.1 Governing Equations

For completeness, we start with the unsteady Euler equations that govern the dynamics of ideal compressible flows and are expressed in a conservative vector form

$$\rho_t + \nabla \cdot (\rho \mathbf{u}) = 0 \tag{3.1}$$

$$(\rho \boldsymbol{u})_t + \nabla \cdot (\rho \mathbf{u} \times \mathbf{u}) = -\nabla p \tag{3.2}$$

$$(\rho E)_t + \nabla \cdot [\mathbf{u}\,(\rho E + p)] = 0 \tag{3.3}$$

where ρ represents density, $\boldsymbol{u}$ denotes the velocity vector, and p stands pressure. The total energy per unit volume, E, is also defined as

$$E = e + \frac{1}{2}|\mathbf{u}|^2 \tag{3.4}$$

with e being the internal energy per unit volume.

The equation of state also is given by

$$p = \rho e(\gamma - 1) \tag{3.5}$$

where γ is the specific heat ratio, a fundamental property of the fluid influencing its thermodynamic behavior under compressible conditions. These equations describe the conservation of mass, momentum, and energy, respectively, in the flow field

Nonconservative systems play a significant role when it comes to achieving accurate numerical discretization. To address this, a Lax-Wendroff type discretization method is applied to the nonconservative system, particularly to the physical disturbance systems that are distinctly present within it. This approach offers valuable insights into the temporal evolution of each physical disturbance, contributing to a more intuitive understanding of their behavior over time.

Below is the representation of the nonconservative Euler system

$$\rho_t + \boldsymbol{u} \cdot \nabla \rho + \rho \nabla \cdot \boldsymbol{u} = 0 \tag{3.6}$$

$$\boldsymbol{u}_t + \boldsymbol{u} \cdot \nabla \boldsymbol{u} + \frac{1}{\rho} \nabla \rho = \mathbf{0} \tag{3.7}$$

$$p_t + \boldsymbol{u} \cdot \nabla p + \gamma p \nabla \cdot \boldsymbol{u} = 0 \tag{3.8}$$

Introducing entropy as a measure of system disorder linked to the dispersion of energy,

$$s = C_v \log \frac{p}{\rho^\gamma} + C \tag{3.9}$$

Under isentropic conditions, it implies

$$\left.\frac{\partial p}{\partial \rho}\right|_{s=\text{constant}} \equiv a^2 = \frac{\gamma p}{\rho} \tag{3.10}$$

Here a^2 represents the square of the speed of sound in the system.

Equations 3.6 - 3.8 can be expressed in matrix form as

$$\boldsymbol{q}_t + \mathcal{A}_\mathcal{D}(\boldsymbol{q}) + \mathcal{A}_\mathcal{C}(\boldsymbol{q}) = 0 \tag{3.11}$$

Here, $\boldsymbol{q} = (\rho, u, v, w, p)^T$ represents the vector of nonconservative variables. The operators $\mathcal{A}_\mathcal{D}$ and $\mathcal{A}_\mathcal{C}$ correspond to the advective and acoustic operators, respectively.

The advective operator $\mathcal{A}_\mathcal{D}$ is given by

$$\mathcal{A}_\mathcal{D} = \begin{bmatrix} \mathbf{u}\cdot\nabla & 0 & 0 & 0 & 0 \\ 0 & \mathbf{u}\cdot\nabla & 0 & 0 & 0 \\ 0 & 0 & \mathbf{u}\cdot\nabla & 0 & 0 \\ 0 & 0 & 0 & \mathbf{u}\cdot\nabla & 0 \\ 0 & 0 & 0 & 0 & \mathbf{u}\cdot\nabla \end{bmatrix} \tag{3.12}$$

and the expression for the acoustic operator $\mathcal{A}_\mathcal{C}$ is as follows

$$\mathcal{A}_\mathcal{C} = \begin{bmatrix} 0 & \rho\partial_x & \rho\partial_y & \rho\partial_z & 0 \\ 0 & 0 & 0 & 0 & \frac{1}{\rho}\partial_x \\ 0 & 0 & 0 & 0 & \frac{1}{\rho}\partial_y \\ 0 & 0 & 0 & 0 & \frac{1}{\rho}\partial_z \\ 0 & \rho a^2\partial_x & \rho a^2\partial_y & \rho a^2\partial_z & 0 \end{bmatrix} \tag{3.13}$$

This matrix representation decomposes the nonconservative Euler equations into the advective and acoustic components, allowing for a more insightful analysis of the system's dynamics. This approach has been used in [43] and [44] to compute the flow due to a translating vortex and also past a lifting airfoil. In this thesis, we will only be concerned with the acoustic subsystem but we will also consider its extension to linear elastodynamics.

By linearizing the acoustic subsystem, we can express the linearized acoustic part of the

Euler equations as follows

$$\boldsymbol{q}_t + a_0 \mathcal{L}_{\mathcal{A}_\mathcal{C}}(\boldsymbol{q}) = \mathbf{0} \tag{3.14}$$

where a_0 is wave speed which in general may be a function of time and space and $\mathcal{L}_{\mathcal{A}_\mathcal{C}}$ is the linearized acoustic spatial gradient matrix

$$\mathcal{L}_{\mathcal{A}_\mathcal{C}} = \begin{bmatrix} 0 & \partial_x & \partial_y & \partial_z \\ \partial_x & 0 & 0 & 0 \\ \partial_y & 0 & 0 & 0 \\ \partial_z & 0 & 0 & 0 \end{bmatrix} \tag{3.15}$$

It's noteworthy that if the coefficient a_0 is not constant, Equation 3.14 can give rise to vorticity $\boldsymbol{\omega} = \nabla \times \boldsymbol{u}$ according to

$$\partial_t \boldsymbol{\omega} + \nabla a_0 \times \nabla p = 0 \tag{3.16}$$

Equation 3.16 is derived by taking the curl of Equation 3.14.

In Equation 3.14, the primitive variables $\boldsymbol{q}$ are nondimensionalized using a_0 and constant density, ρ_0, and will be displayed as

$$\boldsymbol{q} = \begin{pmatrix} p/(\rho_0 a_0^2) \\ u/a_0 \\ v/a_0 \\ w/a_0 \end{pmatrix} \tag{3.17}$$

Henceforth, we adopt the convention of utilizing the variables in their normalized form. As an instance, p signifies the normalized pressure, namely $p/(\rho_0 a_0^2)$, within the context of this discussion.

For this specific subset of problems, it is possible to obtain an exact solution for updating the pressure and velocity over time.

3.2 Exact Solutions

Equation 3.14 possesses a formal solution that is defined by

$$\boldsymbol{q}(t, \boldsymbol{x}) = \exp(-a_0 \mathcal{L}_{\mathcal{A}_\mathcal{C}}) \boldsymbol{q}(0, \boldsymbol{x}) = \sum_{p=0}^{\infty} \frac{(-a_0 \mathcal{L}_{\mathcal{A}_\mathcal{C}} t)^p}{p!} \boldsymbol{q}(0, \boldsymbol{x}) \tag{3.18}$$

A fascinating and valuable characteristic of the gradient matrix $\mathcal{L}_{\mathcal{A}_\mathcal{C}}$ is its fulfillment of

$$\mathcal{L}_{\mathcal{A}_\mathcal{C}}^{p+2} = \nabla^2 \mathcal{L}_{\mathcal{A}_\mathcal{C}}^{p} \quad \text{for} \quad p > 2 \tag{3.19}$$

where ∇^2 denotes the Laplacian operator in three-dimensional space.

By utilizing this distinct property of $\mathcal{L}_{\mathcal{A}_\mathcal{C}}$, we can transform Equation 3.18 into a series of odd and even terms, which are further expanded using Equation 3.14 as a basis.

$$\begin{aligned}
\boldsymbol{q}(t) &= \boldsymbol{q}(0) - \sum_{p=2p-1}^{\infty} \frac{(a_0 \mathcal{L}_{\mathcal{A}_\mathcal{C}} t)^p}{p!} \boldsymbol{q}(0) + \sum_{p=2p}^{\infty} \frac{(a_0 \mathcal{L}_{\mathcal{A}_\mathcal{C}} t)^p}{p!} \boldsymbol{q}(0) \\
&= \boldsymbol{q}(0) - a_0 \mathcal{L}_{\mathcal{A}_\mathcal{C}} t \sum_{p=2p-1}^{\infty} \frac{(a_0 \mathcal{L}_{\mathcal{A}_\mathcal{C}} t)^{p-1}}{p!} \boldsymbol{q}(0) + (a_0 \mathcal{L}_{\mathcal{A}_\mathcal{C}} t)^2 \sum_{p=2p}^{\infty} \frac{(a_0 \mathcal{L}_{\mathcal{A}_\mathcal{C}} t)^{p-2}}{p!} \boldsymbol{q}(0) \\
&= \boldsymbol{q}(0) - a_0 \mathcal{L}_{\mathcal{A}_\mathcal{C}} t \left\{ \sum_{p=2p-1}^{\infty} \frac{(a_0 t)^{p-1}}{p!} \nabla^{p-1} \right\} \boldsymbol{q}(0) + (a_0 \mathcal{L}_{\mathcal{A}_\mathcal{C}} t)^2 \left\{ \sum_{p=2p}^{\infty} \frac{(a_0 t)^{p-2}}{p!} \nabla^{p-2} \right\} \boldsymbol{q}(0) \\
&= \boldsymbol{q}(0) - t \left\{ \sum_{p=0}^{\infty} \frac{(a_0 t)^{2p}}{(2p+1)!} \nabla^{2p} \right\} a_0 \mathcal{L}_{\mathcal{A}_\mathcal{C}} \boldsymbol{q}(0) + t^2 \left\{ \sum_{p=0}^{\infty} \frac{(a_0 t)^{2p}}{(2p+2)!} \nabla^{2p} \right\} a_0^2 \mathcal{L}_{\mathcal{A}_\mathcal{C}}^2 \boldsymbol{q}(0) \\
&= \boldsymbol{q}(0) + t \left\{ \sum_{p=0}^{\infty} \frac{(a_0 t)^{2p}}{(2p+1)!} \nabla^{2p} \right\} q_t(0) + t^2 \left\{ \sum_{p=0}^{\infty} \frac{(a_0 t)^{2p}}{(2p+2)!} \nabla^{2p} \right\} \boldsymbol{q}_{tt}(0)
\end{aligned} \tag{3.20}$$

Concurrently, Darboux's equation is given by

$$\partial_{rr} M_r\{f\}(\boldsymbol{x}) + \frac{2}{r} \partial_r M_r\{f\}(\boldsymbol{x}) = M_r\{\nabla^2 f\}(\boldsymbol{x}) \tag{3.21}$$

and it holds true for any function $f(\boldsymbol{x})$ that has been obtained as the spherical mean of some other, sufficiently smooth, function.

This equation has a solution represented by

$$M_r\{f\}(\boldsymbol{x}) = \frac{\sinh(\nabla r)}{\nabla r} f(\boldsymbol{x}) \tag{3.22}$$

In Equation 3.22, $M_r\{f\}(\boldsymbol{x})$ represents the spherical means of a function f, defined as

$$M_r\{f\}(\boldsymbol{x_0}) = \frac{1}{4\pi r^2} \iint_{\partial B_r(\boldsymbol{x_0})} f(\mathbf{y})\, dS(\mathbf{y}) \tag{3.23}$$

where the spherical means compute the average value of function $f(\boldsymbol{x})$ over the surface area $\partial B_r(\boldsymbol{x_0})$ of the influence sphere $B_r(\boldsymbol{x_0})$ with radius r centered at $\boldsymbol{x_0}$.

The odd terms in Equation 3.20 can then be computed as follows:

$$M_R\{f\}(\boldsymbol{x}) = \sum_{p=0}^{\infty} \frac{(a_0 t)^{2p}}{(2p+1)!} \nabla^{2p} \tag{3.24}$$

where, the radius of the spherical means is denoted as $R = a_0 t$.

This phenomenon arises from the fact that the spherical means formula can be represented as a series of point evaluations involving increasing powers of the Laplacian operator. This property becomes evident when we expand the spherical means formula as follows:

$$M_r\{f\}(\boldsymbol{x_0}) = \frac{1}{4\pi r^2} \iint_{\partial B_r(\boldsymbol{x_0})} f(\mathbf{y})\, dS(\mathbf{y}) = \frac{1}{4\pi r^2} \sum_{p=0}^{\infty} \frac{(-1)^p}{(2p)!} r^{2p} \nabla^{2p} f(\boldsymbol{x_0}) \tag{3.25}$$

This expression illustrates how the spherical means of the function f at the point $\boldsymbol{x_0}$ can be computed by evaluating the function f at that point and its higher-order Laplacian derivatives, which are determined by the powers of ∇^2 in the series.

Subsequently, we may incorporate the derived expression directly into the subsequent integral, resulting in a term that corresponds to the even components in Equation 3.20.

$$\begin{aligned} \frac{2}{R^2} \int_0^R r M_r\{f\}(\boldsymbol{x})\, dr &= \frac{2}{R} \int_0^R \frac{r \sinh(\nabla r)}{\nabla r} f(\boldsymbol{x})\, dr \\ &= \frac{2\cosh(\nabla R) - 1}{\nabla^2 R^2} f(\boldsymbol{x}) \\ &= 2 \sum_{p=0}^{\infty} \frac{(a_0 t)^2}{(2p+2)!} \nabla^{2p} f(\boldsymbol{x}) \end{aligned} \tag{3.26}$$

Thus, we can represent the formal solution to the linear acoustics system using Equations 3.24 and 3.26 as follows:

$$\boldsymbol{q}(t, \boldsymbol{x}) = \boldsymbol{q}(0, \boldsymbol{x}) + t M_R\{\boldsymbol{q}_t\}(0, \boldsymbol{x}) + \frac{1}{a_0^2} \int_0^R r M_r\{\boldsymbol{q}_{tt}\}(0, \boldsymbol{x})\, dr \tag{3.27}$$

this applies to all components of $\boldsymbol{q}$.

To determine the first component, p, we begin by taking the second time-derivative of the pressure equation in Equation 3.14:

$$p_{tt} - a_0^2 \nabla^2 p = 0 \tag{3.28}$$

As a result, we can express $p(t, \boldsymbol{x})$ as:

$$p(t, \boldsymbol{x}) = p(0, \boldsymbol{x}) + tM_R\{p_t\}(0, \boldsymbol{x}) + \int_0^R rM_r\{\nabla^2 p\}(0, \boldsymbol{x})\, dr \tag{3.29}$$

Upon combining the first and third terms, we obtain the well-known exact solution for the scalar wave equation, as commonly found in textbooks on partial differential equations [68, 64].

$$p(t, \boldsymbol{x}) = [tM_R\{p\}(0, \boldsymbol{x})]_t + tM_R\{p_t\}(0, \boldsymbol{x}) \tag{3.30}$$

A different representation of the preceding expression can be attained through the expansion of the first term, wherein the time derivative is replaced by a derivative with respect to R. Subsequently, the time derivative can be substituted with spatial derivatives obtained from the pressure equation in Equation 3.14, as originally derived by Eymann [69].

$$\begin{aligned} p(t, \boldsymbol{x}) &= M_R\{p\}(0, \boldsymbol{x}) + R[M_R\{p\}(0, \boldsymbol{x})]_R + tM_R\{p_t\}(0, \boldsymbol{x}) \\ &= M_R\{p\}(0, \boldsymbol{x}) + R[M_R\{p\}(0, \boldsymbol{x})]_R - RM_R\{\nabla \cdot \boldsymbol{u}\}(0, \boldsymbol{x}) \end{aligned} \tag{3.31}$$

It was subsequently pointed out by Barsukow et al. [70] that a variation of this formula is valid in the sense of distributions. The practical implications of this have yet to be fully worked out.

A similar simplification process can be applied to the velocity components of $\boldsymbol{q}$ by utilizing the second time-derivative of the velocity equations in Equation 3.14.

$$\boldsymbol{u}_{tt} - a_0^2 \nabla^2 u - a_0^2 \nabla \times \nabla \times \boldsymbol{u} = \boldsymbol{0} \tag{3.32}$$

This results in the following expression for $\boldsymbol{u}(t, \boldsymbol{x})$:

$$\begin{aligned} \boldsymbol{u}(t, \boldsymbol{x}) = M_R\{\boldsymbol{u}\}(0, \boldsymbol{x}) &+ R[M_R\{\boldsymbol{u}\}(0, \boldsymbol{x})]_R - RM_R\{\nabla p\}(0, \boldsymbol{x}) \\ &+ \int_0^R rM_r\{\nabla \times \nabla \ \times \boldsymbol{u}\}(0, \boldsymbol{x})\, dr \end{aligned} \tag{3.33}$$

Considering the volume integral for an arbitrary velocity field $\boldsymbol{u}(\boldsymbol{x})$

$$\boldsymbol{V} = \iiint_\Omega \nabla \times \nabla \times \boldsymbol{u}\, dV \tag{3.34}$$

We can apply the generalized form of Stokes' equations to obtain

$$\boldsymbol{V} = \iiint_{\Omega} \nabla \times \nabla \times \boldsymbol{u}\, dV = \oiint_{\partial\Omega} \hat{\boldsymbol{n}} \times (\nabla \times \boldsymbol{u})\, dS \tag{3.35}$$

By using the classic Stokes' theorem, we recognize that the flux integral of a curl field over a closed surface is zero due to the absence of a boundary for a closed surface. Consequently

$$\boldsymbol{V} = -\oiint_{\partial\Omega} \nabla \times (\boldsymbol{u} \times \hat{\boldsymbol{n}})\, dS = -\int_{0} (\boldsymbol{u} \times \hat{\boldsymbol{n}})\, ds = \boldsymbol{0} \tag{3.36}$$

Next, we establish a relationship between the radial change in the volume integral and the spherical means integral

$$\boldsymbol{V}_r = 4\pi r^2 M_r\{\nabla \times \nabla \times \boldsymbol{u}\}(\boldsymbol{x}) = 0 \tag{3.37}$$

This leads to the conclusion that $M_r\{\nabla \times \nabla \times \boldsymbol{u}\}(\boldsymbol{x}) = 0$, thereby eliminating the integral term in Equation 3.33.

Ultimately, the exact solution to Equation 3.14 can be expressed as follows

$$\boldsymbol{q}(t, \boldsymbol{x}) = M_R\{\boldsymbol{q}\}(0, \boldsymbol{x}) + R[M_R\{\boldsymbol{q}\}(0, \boldsymbol{x})]_R - RM_R\{\mathcal{L}_{\mathcal{A}_\mathcal{C}} \boldsymbol{q}\}(0, \boldsymbol{x}) \tag{3.38}$$

Visually, this has the appearance of a Lax-Wendroff expansion and can be used to derive one if the spherical means are evaluated to low order. If the spherical means are evaluated with increasing accuracy, the accuracy of the formula increases correspondingly. The second term contains the effects of all odd time derivatives, and the third term the effects of all even time derivatives.

Hermite elements employ gradients among their degrees of freedom. This gives rise to the requirement for an exact solution concerning the gradients of $\boldsymbol{q}(t, \boldsymbol{x})$. Given the linear nature of the spherical means integral $M_r\{f\}(\boldsymbol{x})$ and the linearized acoustic spatial gradient operator $\mathcal{L}_{\mathcal{A}_\mathcal{C}}$, it becomes feasible to differentiate Equation 3.38 to derive an exact solution for gradients.

$$\boldsymbol{q}_{x_i}(t, \boldsymbol{x}) = M_R\{\boldsymbol{q}_{x_i}\}(0, \boldsymbol{x}) + R[M_R\{\boldsymbol{q}_{x_i}\}(0, \boldsymbol{x})]_R - RM_R\{\mathcal{L}_{\mathcal{A}_\mathcal{C}} \boldsymbol{q}_{x_i}\}(0, \boldsymbol{x}) \tag{3.39}$$

Higher-order gradients can also be derived by taking successive derivatives, effectively obtaining a derivative of a derivative, as demonstrated in the differentiation of Equation 3.39.

3.3 Numerical Solutions on Coarse Grids

The conservation law equations are expressed as:

$$\boldsymbol{Q}_t + \sum_{i=1}^{3} (\boldsymbol{f}_i)_{x_i} = \mathbf{0} \tag{3.40}$$

In this equation, $\boldsymbol{Q}$ represents the vector of conservative variables, and $\boldsymbol{f}_i$ denotes the flux in the direction x_i

The Finite Volume Methods (FVM) are widely used numerical discretization techniques for solving conservation laws. They divide the computational domain into discrete control volumes, preserving essential physical quantities like mass, momentum, and energy. FVM's accuracy lie in approximating fluxes across control volume interfaces, considering neighboring variables and gradients. Their adaptability to complex geometries makes them a preferred choice in various computational simulations, ensuring robustness and accuracy in analyzing intricate scientific problems. However, the unstructured discretization nature limits FVM's development for higher accuracy. Unstructured grids, in particular, pose challenges in finding neighbors of neighbors. Furthermore, this is not the only concern; even if efficient algorithms are developed to address the computation of fluxes with a larger stencil, the method should still remain fully-discrete and explicit. The reason is that although the numerical stencil must, clearly, enclose the analytical domain of dependence to prevent instability, a numerical stencil that is too large will include data that has no relevance to the solution, which results either in instability or in a very dissipative scheme. Additionally, any semi-discrete method adds to its stencil at each stage and will eventually take most of its data from outside the true domain of dependence, unless the time step is made very small. Hence, although semi-discrete methods do allow us to obtain high formal accuracy for long waves, they are of little use with regard to obtaining well-behaved mid- and high-frequency behavior.

The Active Flux method presents a novel approach to address the issues faced by current high-order methods, as mentioned earlier. The scheme's name reflects its distinct feature of updating interface values independently from conserved quantities. This is achieved by computing an *active flux* directly from edge values, taking into account both previous cell values and previous edge values. It is essential to note that the interface update does not necessarily need to be conservative. Instead, the requirement is for the fluxes to be consistent, allowing for the use of any suitable method to generate an interface update. For instance, Equation 3.40 can also be expressed in terms of primitive variables, which are often easier

to nonconservatively solve and can be employed for the interface update.

$$\boldsymbol{q}_t + \sum_{i=1}^{3} \boldsymbol{A}_i^{\boldsymbol{q}} \boldsymbol{q}_{x_i} = \boldsymbol{0} \tag{3.41}$$

In this equation, $\boldsymbol{q}$ denotes the vector of primitive variables, and $\boldsymbol{A}_i^{\boldsymbol{q}}$ represents the coefficient matrices associated with the primitive form of the conservation laws.

Unlike the FVM, which rely more on inter-element communication, the AF method's strength lies in its ability to generate flux values from interface data, resulting in a conservative scheme. The AF method operates primarily within individual elements, minimizing the need for extensive communication between neighboring elements. This flexibility in selecting the interface update method also allows for the integration of multidimensional physics.

In the AF method, the solution of conservation laws unfolds in four distinct stages.

1. **Reconstruction:** The initial step of the AF method is to perform a reconstruction of primitive variables $\boldsymbol{q}$ within an element. This choice guarantees the scheme's exactness for data with the order of reconstruction.

2. **Evolution:** In the second stage, the AF method updates the primitive variables at the element interface using any **consistent** and appropriate method. The method need not be conservative, offering the advantage of selecting an update method that accurately represents physical processes in multidimensions.

3. **Conservation:** The third stage involves constructing average fluxes from the interface data by integrating along the element's interfaces, utilizing a high-order approximation compatible with the reconstruction. These fluxes are then used to update the conserved element-average, akin to finite volume methods.

4. **Correction:** The fourth and final stage, if necessary, corrects the interface values to ensure that the reconstruction's average aligns with the element average updated in stage three. It's important to note that due to the non-conservative nature of the evolution stage, this alignment is not automatically satisfied. Explicit enforcement becomes essential, particularly when the element reconstruction lacks a degree of freedom as the element average.

This is depicted schematically in Figure 3.1. Algorithm 3.1 also demonstrates the modifications to Algorithm 2.1 required to adapt it for different stages of the active flux method. These updates are carried out through grid traversal procedures. Note that in this algorithm, stages one and two are combined into a single function.

Algorithm 3.1 Active Flux

Require: Grid G with n elements and information associated with each element.
Ensure: Numerically solve conservation laws.

function InterfaceUpdate(*element*)
Mark *element* as visited.
Reconstruct the solution within *element*.
Update *element*'s contribution to the interfaces.
for each neighbor e of *element* **do**
  if e is not visited **then**
    InterfaceUpdate(e)
  end if
end for
end function
function Conserve(*element*)
Mark *element* as visited.
for each face f of *element* **do**
  if f is not visited **then**
    Mark f as visited.
    Compute the average flux at f.
    Add/subtract the appropriate residual value to *elemnt*/neighboring *element* interfaced with f.
  end if
end for
for each neighbor e of *element* **do**
  if e is not visited **then**
    Conserve(e)
  end if
end for
end function
function Correct(*element*)
Mark *element* as visited.
Calculate the difference between the element average updated from conservation and the reconstruction's average.
Incorporate *element*'s contribution into the interface correction.
for each neighbor e of *element* **do**
  if e is not visited **then**
    Correct(e)
  end if
end for
end function
Call InterfaceUpdate with an starting *element*.
Call Conserve with an starting *element*.
Call Correct with an starting *element*.

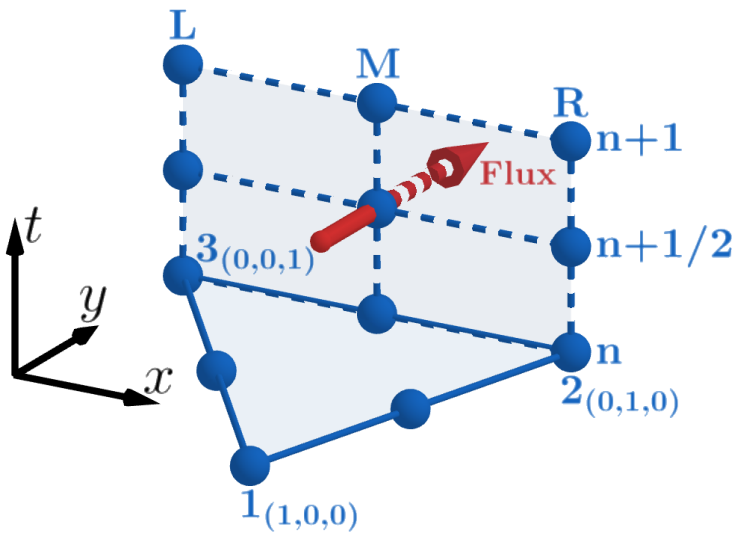

Figure 3.1: Schematic representation of Active Flux Element.

3.3.1 One Dimension

Let's begin by performing a preliminary analysis of linear acoustics in one-dimensional space written in conservative form as

$$\boldsymbol{q}_t + \boldsymbol{f}_x = \mathbf{0} \tag{3.42}$$

where $\boldsymbol{q} = (p, u)^T$ is the conserved vector, and $\boldsymbol{f} = a_0(u, p)^T$ is conservative flux function with constant wave-speed a_0.

The solution $\boldsymbol{q} = \boldsymbol{q}(t, x)$ to Eq. 3.42 undergoes spatial and temporal evolution within an arbitrary spatial domain Ω, which is divided into N non-overlapping elements denoted as

$$\Omega_i = \{x | x_i < x < x_{i+1}\}, \quad \Omega = \bigcup_{i=1}^{N} \Omega_i \tag{3.43}$$

Similar to the approach described in Section 2.4 for a single element, we utilize a mapping technique to streamline the representation of the solution within these elements. This mapping transforms the physical space x within each element Ω_i into a reference space ξ using the equation

$$\xi = \frac{x - x_i}{x_{i+1} - x_i} = \frac{1}{\Delta x}(x - x_i) \tag{3.44}$$

where $\Delta x = x_{i+1} - x_i$ represents the element length (refer to figure 3.2).

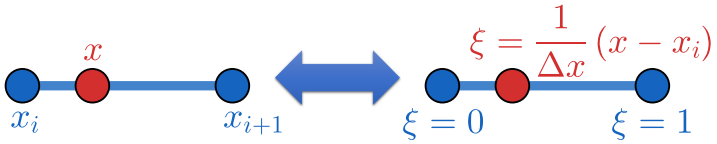

Figure 3.2: Mapping from physical space to reference space for one-dimensional element.

3.3.1.1 Reconstruction

Within the element Ω_i, the solution $\boldsymbol{q}$ is reconstructed through data interpolation using a polynomial of degree p, exclusively within the confines of Ω_i, and holding a value of zero outside of this element. Employing explicit methods in evolution stage, we analyze the problem within each element Ω_i, which computes a new solution $\boldsymbol{q}_i^{n+1}$ based on the old solution $\boldsymbol{q}_i^n$ with an accuracy of $(p+1)$-th order. Consequently, for this computation, it is necessary to have $p+1$ pieces of information available at time-level n to ensure the accuracy of the method.

In the context of one-dimensional space, this interpolation process is achieved through a set of basis functions denoted as $B_p = \{b_i(\xi)\}$, which collectively constitute a complete set of polynomials of degree p. The set B_p consists of $p+1$ basis functions. The approximation of $\boldsymbol{q}$ is then performed by projecting the data onto these basis functions B_p, leading to the representation

$$\boldsymbol{q}(\xi) = \sum_{i=1}^{p+1} \boldsymbol{c}_i b_i(\xi) \tag{3.45}$$

In the given equation, $\boldsymbol{c}_i$ denotes the coefficient associated with the basis function b_i, enabling us to reconstruct the solution $\boldsymbol{q}$ within the element Ω_i. Refer to Figure 2.2 and 2.3, as well as Table 2.1 and 2.2 for detailed information on the various element types, their coefficients, and corresponding basis functions.

The selection of elements depends on the accuracy requirements, offering various options like incorporating Hermite elements alongside standard elements. The utilization of Hermite elements allows the inclusion of gradients as additional information to enrich the element, resulting in improved stability and efficiency in finding the solution. A comprehensive explanation of these distinct element choices is provided in Chapter 2. In the present chapter, our primary focus lies in the exploration and evaluation of highly accurate elements that facilitate acoustic analysis on coarse grids.

3.3.1.2 Evolution

During the evolution stage, we adhere to the methodology given in Section 3.2 for obtaining the exact solutions of the linear acoustic equations. In the context of one-dimensional space, utilizing Equation 3.14, we reduce $\mathcal{L}_{\mathcal{A}_\mathcal{C}}$ to accommodate the one-dimensional nature of the problem.

$$\mathcal{L}_{\mathcal{A}_\mathcal{C}{}^{1D}} = \begin{bmatrix} 0 & \partial_x \\ \partial_x & 0 \end{bmatrix} \tag{3.46}$$

Here, the spherical means integral adopts a straightforward form, reducing to

$$M_R\{f\}(x) = \frac{1}{2R}\int_{-R}^{R} f(x)dx \tag{3.47}$$

This simplification leads to the expressions for the exact solutions as presented in equation 3.38

$$p(t,x) = \frac{1}{2}[p(0,R) + p(0,-R) - u(0,R) + u(0,-R)] \tag{3.48}$$

$$u(t,x) = \frac{1}{2}[u(0,R) + u(0,-R) - p(0,R) + p(0,-R)] \tag{3.49}$$

These expressions serve as the basis for the independent update method utilized during the evolution stage. It's worth noting the linear characteristic of Equation 3.48 and Equation 3.49, which permits differentiation of the primitive variables, of any order and in any direction, thereby providing the necessary gradient update expressions, obey the same governing equations, for Hermite-type elements.

3.3.1.3 Conservation

This stage entails the numerical solution of the conservation law equation represented by Equation 3.42. The computation of the average flux $\bar{\boldsymbol{f}}_i = (1/\Delta t)\int_{t^n}^{t^n+\Delta t} \boldsymbol{f}_i\, dt$ at interface i requires a numerical integration technique of adequate accuracy, consistent with the precision of the reconstruction.

For a second-order element, the application of Simpson's rule yields the calculation of the average flux as

$$\bar{\boldsymbol{f}} = \frac{1}{6}[\boldsymbol{f}^n + 4\boldsymbol{f}^{n+\frac{1}{2}} + \boldsymbol{f}^{n+1}] \tag{3.50}$$

On the other hand, employing a fourth-order element involves the utilization of the

Gauss–Lobatto rule, resulting in

$$\bar{\boldsymbol{f}} = \frac{1}{12}\left[\boldsymbol{f}^n + 5\left(\boldsymbol{f}^{n+\frac{1-\sqrt{1/5}}{2}} + \boldsymbol{f}^{n+\frac{1+\sqrt{1/5}}{2}}\right) + \boldsymbol{f}^{n+1}\right] \tag{3.51}$$

These computed average flux values are subsequently used to update the conserved element-average in a manner akin to FV methods, as expressed by

$$\bar{\boldsymbol{q}}_i^{n+1} = \bar{\boldsymbol{q}}_i^n - \frac{\Delta t}{\Delta x}(\bar{f}_{i+1} - \bar{f}_i) \tag{3.52}$$

3.3.1.4 Correction

In general, inconsistency arise between the element average of the reconstructed $\boldsymbol{q}_i$ described by Equation 3.45 and the one deduced from the conservation law as expressed in Equation 3.52. This incongruity stems from the selection of an *independent* update method, which does not necessarily maintain conservation. This inconsistency within element Ω_i is defined as

$$d\bar{\boldsymbol{q}}_i = \bar{\boldsymbol{q}}_i - \sum_{j=1}^{p+1} \boldsymbol{c}_j \int_0^1 b_j(\xi)\, d\xi \tag{3.53}$$

To ensure conservation, it is imperative that

$$\sum_{i=1}^{N} d\bar{\boldsymbol{q}}_i \Delta x_i = 0 \tag{3.54}$$

Notably, the achievement of conservation does not mandate eliminating inconsistency for each individual element ($d\bar{\boldsymbol{q}}_i = 0$ for $i = 1, 2, ..., N$). Nevertheless, this practice still upholds conservation as it satisfies Equation 3.54.

In the most recent formulation, conservation is enforced by distributing the inconsistency across the information within each element. For instance, consider element Ω_i having $p+1$ degrees of freedom, including values $\boldsymbol{q}_{i_{(j)}}$ and gradients $\partial\boldsymbol{q}_{i_{(j)}}$ at location j. The inconsistency $d\bar{\boldsymbol{q}}_i$ is exclusively distributed to the values

$$\boldsymbol{q}_{i_{(j)}} := \boldsymbol{q}_{i_{(j)}} + \alpha_{i_{(j)}} d\bar{\boldsymbol{q}}_i \tag{3.55}$$

Here, the corrector weights $\alpha_{i_{(j)}}$ are determined based on the requirement of conservation law [71]

$$\sum_{j=\text{value basis only}} \alpha_{i_{(j)}} \int_0^1 b_j(\xi)\, d\xi = 1 \tag{3.56}$$

The selection of corrector weights is not universally unique and depends on the degree of freedom within the element. For elements with interior degrees of freedom, $\alpha_{i_{(j)}}$ at interfaces are set to zero to prevent discontinuities. However, for elements having degrees of freedom only at interfaces, $\alpha_{i_{(j)}}$ cannot be zero. This circumstance introduces a discontinuity at the interfaces, which is resolved by averaging the shared values of neighboring elements

$$\boldsymbol{q}_i := \boldsymbol{q}_i + \frac{\alpha_{i_{(j=left)}} d\bar{\boldsymbol{q}}_i \Delta x_i + \alpha_{i-1_{(j=right)}} d\bar{\boldsymbol{q}}_{i-1} \Delta x_{i-1}}{\Delta x_i + \Delta x_{i-1}} \tag{3.57}$$

3.3.1.5 Smooth Solution

Our initial findings revolve around the evaluation of the accuracy offered by the different one-dimensional element types introduced in Chapter 2. To conduct this assessment, we utilize a smooth solution based on the initial conditions outlined by Lukacova-Medivid'ova, Morton, and Warnecke [72]. Although this solution is initially presented in two dimensions and will be further explored in Section 3.3.2.6, we adapt it to a one-dimensional context for our present testing purposes.

$$\begin{aligned} p(0,x) &= \frac{1}{a_0}\sin(2\pi x) \\ u(0,x) &= 0 \end{aligned} \tag{3.58}$$

The sine waves problem possesses an analytical solution in one-dimensional space, characterized by the presence of standing waves.

$$\begin{aligned} p(t,x) &= \frac{1}{a_0}\cos(2\pi a_0 t)\sin(2\pi x) \\ u(t,x) &= -\frac{1}{a_0}\sin(2\pi a_0 t)\cos(2\pi x) \end{aligned} \tag{3.59}$$

The computations are conducted within the domain $\Omega = [-1/2, 1/2]$, with a wave speed of $a_0 = 1$. To establish a Courant number, we introduce a length scale by considering the number of elements. Consequently, with N elements, the length scale is defined as $L = 1/N$. Figure 3.3 illustrates the outcomes of simulations conducted over 2008 temporal iterations using a Courant number of 0.8. This figure depicts the performance of various element types. It is evident that a standard element with $p = 2$ (depicted in Figure 2.2b) exhibits comparatively subpar performance when contrasted with the other two Hermite elements outlined in Figure 2.3.

An important observation is that the Hermite element with $p = 3$ in this context lacks interior degrees of freedom. Therefore, conservation is attained through the utilization of

Equation 3.57, elucidated in Section 3.3.1.4, during the corrector stage. In contrast, the other two elements encompass interior nodes, and conservation is established by distributing the discrepancy exclusively to the interior nodes. This approach avoids compelling the resolution of potential discontinuities.

Figure 3.4 displays the L_2 error computed after one complete period ($t = 1/a_0$) as a function of the mesh size. The Courant number was selected as 0.8, considering the aforementioned mesh size specification. Notably, the Hermite element with $p = 4$ method exhibits exceptional precision (approximately 0.01% error) with four cells per wavelength. This stands in contrast to the standard element with $p = 2$, which yields an error of about 1% under the same conditions of elements per wavelength.

The derivatives of a numerical solution often exhibit an order of accuracy one less than that of the point values. To address this, we multiplied the errors by Δx when plotting them (essentially representing the value error resulting from a gradient error). The presented outcomes demonstrate highly encouraging results, which motivate us to further explore the application of Hermite elements in higher dimensions. This extension of the concept will be deliberated in Section 3.3.2.

3.3.1.6 Non-Simple Wave

We employ a non-simple wave problem to evaluate the performance of the elements, where both characteristic variables vary across the domain.

$$\begin{aligned} p(0,x) &= \frac{1}{4} + \frac{1}{80}\sin(2\pi x) \\ u(0,x) &= \frac{1}{4} - \frac{1}{10}\sin(\pi x) \end{aligned} \tag{3.60}$$

In this scenario, the solution becomes slightly more intricate. However, the exact solution continues to maintain a simple form owing to the linear nature of the underlying problem.

$$p(t,x) = \frac{1}{2}[p(0,x+a_0t) + p(0,x-a_0t) - u(0,x+a_0t) + u(0,x-a_0t)] \tag{3.61}$$

$$u(t,x) = \frac{1}{2}[u(0,x+a_0t) + u(0,x-a_0t) - p(0,x+a_0t) + p(0,x-a_0t)] \tag{3.62}$$

The identical numerical setup that was applied to the smooth problem is also utilized for the non-simple wave problem. The only difference in this case is that the domain is expanded to $\Omega = [0, 2]$.

Figure 3.5 provides a comparative analysis between the exact and numerical results for various element types at $t = 10.9$. Notably, the differences are more discernible in the case

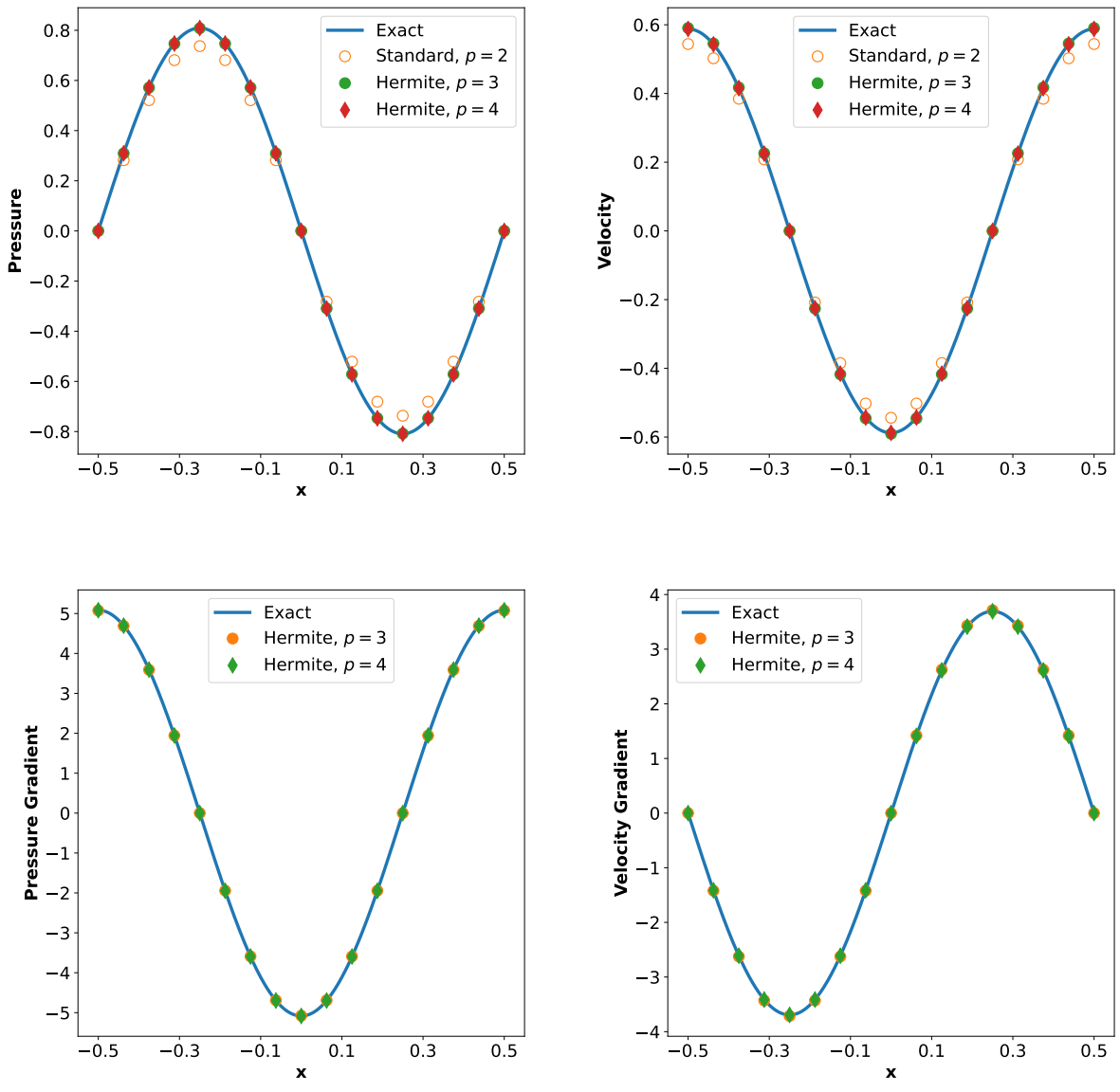

Figure 3.3: Pressure and velocity solutions for the one-dimensional smooth wave problem after completing 2008 temporal iterations considering different element types. Refer to Figures 2.2 and 2.3 for visual representations of the elements.

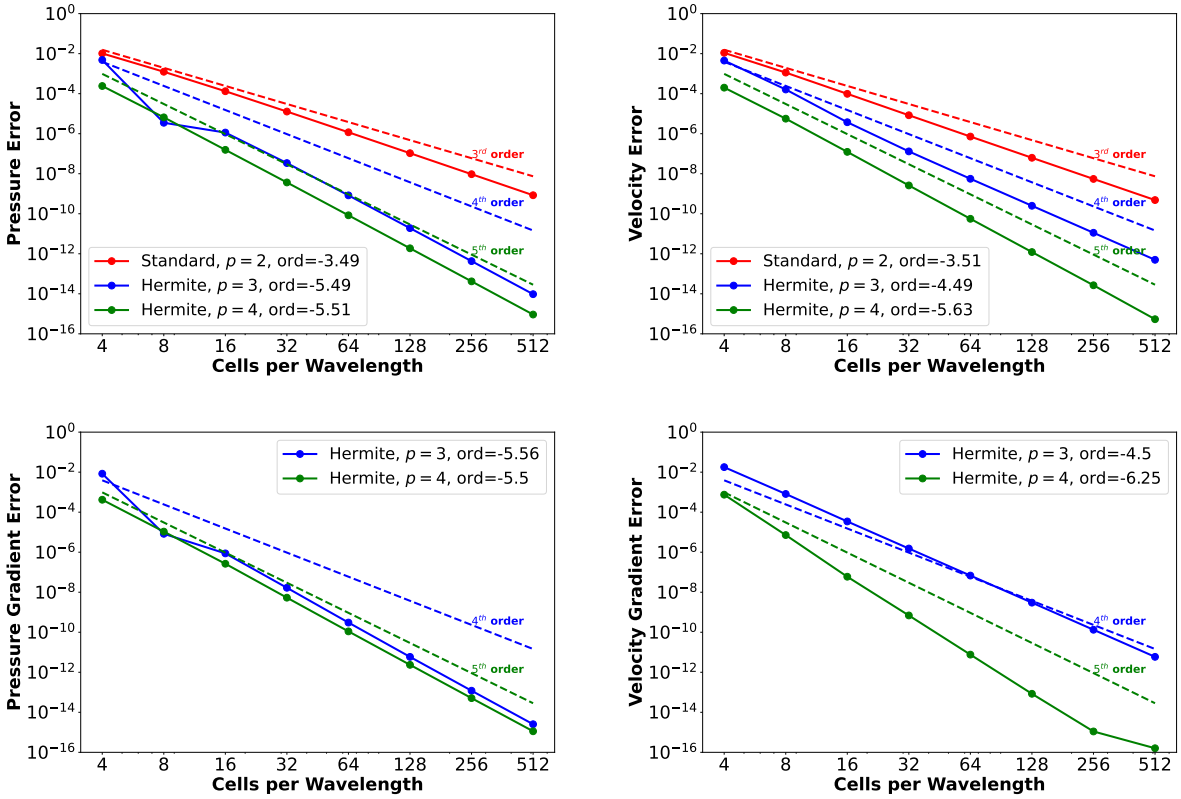

Figure 3.4: Errors after evolution over one period for the one-dimensional smooth wave problem. The gradient errors are computed as Δx multiplied by the Gradient Error value.

of the standard element with $p = 2$. This discrepancy can be attributed to the presence of a higher-frequency pressure wave, which results in increased dissipation within this particular element. In contrast, the Hermite elements exhibit remarkably favorable outcomes, showcasing excellent agreement with the exact solution.

This discrepancy in accuracy highlights the influence of the chosen element type on the numerical results, particularly in scenarios involving variations in characteristic variables across the domain. It's important to consider the implications of these findings in the context of computational acoustics simulations in multi-dimensions.

3.3.1.7 Square Wave

Upon confirming that the Active Flux solver consistently generates nearly indistinguishable outcomes for smooth scenarios, particularly when employing high-order elements such as Hermite elements, it is now imperative to subject these elements to examination under discontinuous conditions. To this end, we consider the initial configuration involving a basic square wave profile, formulated as follows:

Let the initial conditions be defined as

$$\begin{aligned} p(0,x) &= \begin{cases} 1 & \text{if } -1 \leq x \leq 1 \\ 0 & \text{elsewhere} \end{cases} \\ u(0,x) &= 0 \end{aligned} \tag{3.63}$$

The computational domain $\Omega = [-2, 2]$, discretized into 40 elements spanning the domain. Once again, it is noteworthy that due to the linearity of the governing equations, the exact solution possesses a straightforward representation as articulated in Equation 3.61 and Equation 3.62. Employing a Courant number of 0.6, we proceed to evaluate the propagation of waves in the system.

Figure 3.6 presents a visual representation of the wave's propagation at $t = 12$. It's important to note that due to the periodic nature of the domain boundaries, the compression wave departing from the leading boundary undergoes re-entry at the opposing end. By the time $t = 12$ is reached, the wave has completed a three full cycle and returned to its original position, aligning with the initial conditions.

The observations from the figure reveal that the Hermite element with a polynomial order of $p = 4$ closely approximates the exact results, capturing the inherent discontinuities with impressive accuracy. In comparison, the standard element featuring a polynomial order of $p = 2$ exhibits superior performance when contrasted with the exact solution. This particular test case also serves as a foundational benchmark to contextualize our outcomes in

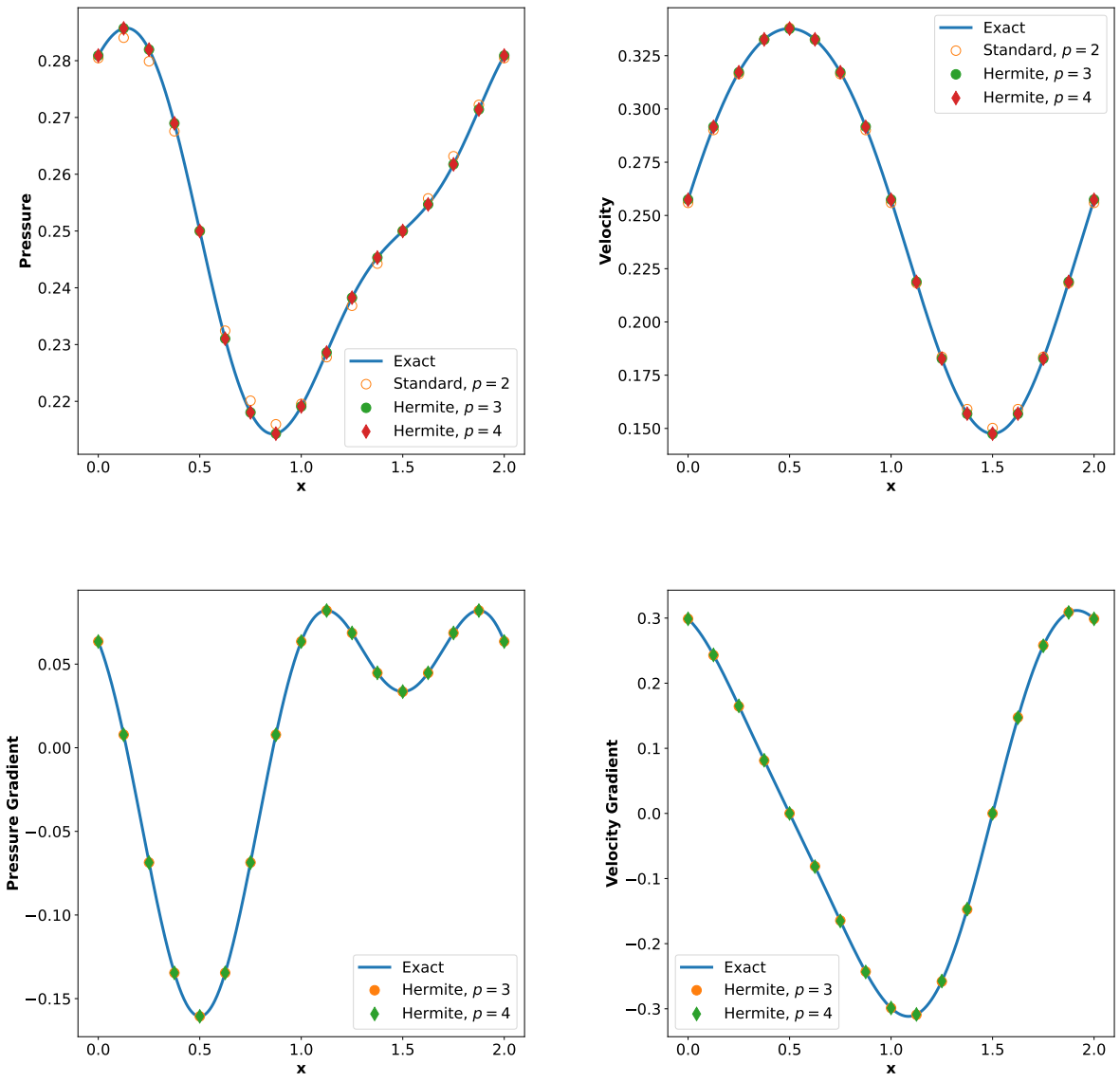

Figure 3.5: Pressure and velocity solutions for the one-dimensional non-simple wave problem at $t = 10.9$ considering different element types. Refer to Figures 2.2 and 2.3 for visual representations of the elements.

multi-dimensional settings against those established in the one-dimensional realm. This comparative assessment is visually depicted in Figure 3.13, which contrasts the two-dimensional outcomes with their one-dimensional counterparts. This augmentation provides valuable insights into the method's efficacy across varying dimensions and complexities.

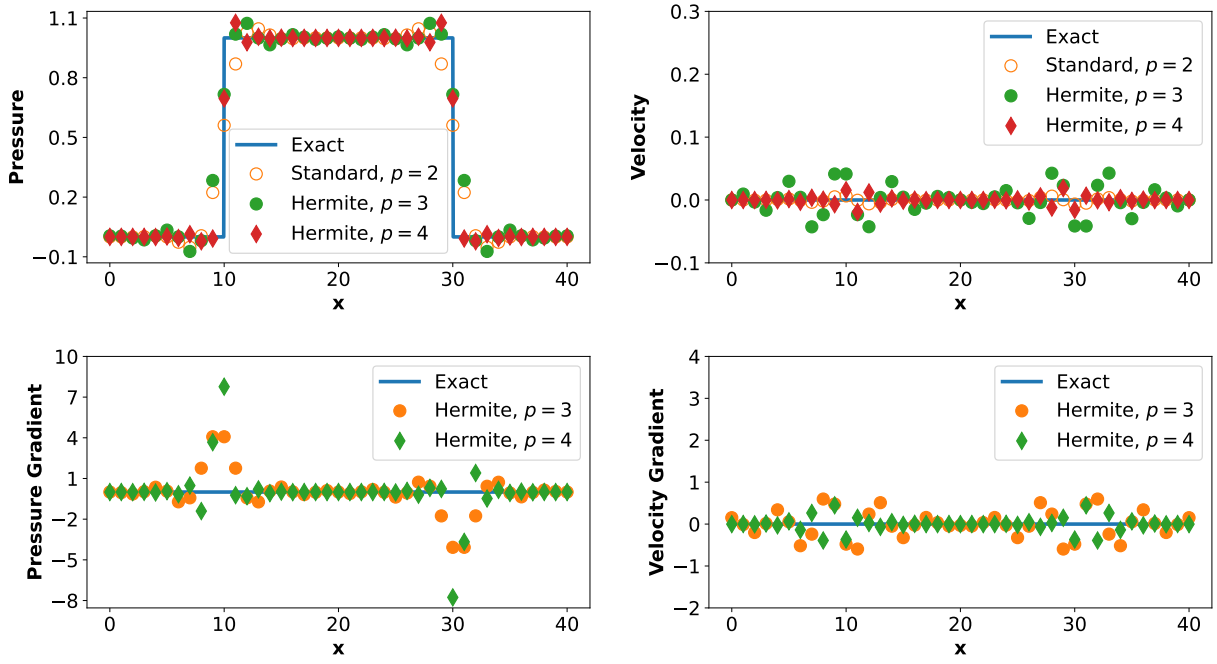

Figure 3.6: Pressure and velocity solutions for the one-dimensional square wave problem at $t = 12$ considering different element types. Refer to Figures 2.2 and 2.3 for visual representations of the elements.

3.3.2 Two Dimensions

In this section, our focus shifts towards the design of a multidimensional scheme, a logical progression built upon the insights derived from our comprehensive one-dimensional analysis. As elucidated in Chapter 2, our investigation demonstrated a systematic approach for establishing the parameters necessary to achieve arbitrary accuracy and dimensionality within an element definition. This chapter also underscored the intricate nature of the challenges that emerge as accuracy and dimensionality are augmented. The growth in the number of degrees of freedom, coupled with the various possibilities for their placement within the element, magnifies the complexity of the system.

Extending our endeavor to encompass a systematic array of schemes with arbitrary accuracy and dimensionality presents an even more intricate landscape to navigate. Nevertheless, within the forthcoming sections, we shall meticulously expound upon a two-dimensional

method of fifth-order, a method that not only presents a comprehensive formulation but also holds the potential for further extensions. Our pursuit is to replicate the efficacy of the fifth-order Active Flux method, a technique that has exhibited commendable performance within the realm of one-dimensional simulations. Furthermore, its inherent advantages become even more pronounced in the context of higher dimensions.

To facilitate a comparative analysis, we juxtapose our fifth-order approach with the third-order method, achieved by selectively omitting gradient information. Although, admittedly, our engagement with higher-order methods initially bore a sense of caution, we firmly assert the feasibility of venturing into these more ambitious frontiers. This belief stems from the robust foundation of understanding we have established, coupled with the promising outcomes that our meticulous exploration of the Active Flux method has yielded.

Linear acoustics in a two-dimensional spatial domain can be expressed in a conservative form as

$$\boldsymbol{q}_t + \sum_{i=1}^{2} (\boldsymbol{f}_i)_{x_i} = \boldsymbol{0} \tag{3.64}$$

Here, the vector $\boldsymbol{q} = (p, u, v)^T$ represents the conserved quantities associated with the system. The conservative flux functions, $\boldsymbol{f}_i$, are defined as:

$$\boldsymbol{f}_1 = a_0 \begin{pmatrix} u \\ p \\ 0 \end{pmatrix} \quad \text{and} \quad \boldsymbol{f}_2 = a_0 \begin{pmatrix} v \\ 0 \\ p \end{pmatrix} \tag{3.65}$$

where the constant wave-speed is represented by a_0.

In the context of two-dimensional space, the solution $\boldsymbol{q} = \boldsymbol{q}(t, \boldsymbol{x})$, to Equation 3.64 evaluates over time and space within a defined spatial domain $\boldsymbol{\Omega}$. This domain is discretized into N non-overlapping two-dimensional triangular elements. To define these elements, a barycentric coordinate system is employed, as elaborated upon in Section 2.5. This strategic selection is employed to uphold the stability of the reconstruction process through the utilization of a basis that possesses enhanced orthogonality for the interpolation procedure.

3.3.2.1 Reconstruction

Within element $\boldsymbol{\Omega}_i$, the solution $\boldsymbol{q}_i^n$ at time level n is reconstructed using a polynomial of degree p. To facilitate this process, a set of basis functions denoted as $B_p = \{b_i(\sigma_1, \sigma_2, \sigma_3)\}$, with a cardinality of $(p+1)(p+2)/2$, is employed. This collection constitutes a complete ensemble of polynomials of degree p, aligning with the analogous strategy in one-dimensional

space. Consequently, the representation of $\boldsymbol{q}$ is achieved through its projection onto B_p.

$$\boldsymbol{q} = \sum_{i=1}^{(p+1)(p+2)/2} \boldsymbol{c}_i b_i, \tag{3.66}$$

Here, $\boldsymbol{c}_i$ corresponds to the coefficient associated with the basis function b_i, as detailed in Table 2.3 and Table 2.4. This formulation indicates that at time level n, there exist $(p+1)(p+2)/2$ individual pieces of information available for the reconstruction process, as illustrated in Figure 2.5 and Figure 2.6.

3.3.2.2 Evolution

Similar to our approach for the one-dimensional problem, we adhere to the guidelines introduced in Section 3.2 to derive exact solutions for the linear acoustic equations, this time in the context of two dimensions during the evaluation stage. Consequently, this simplifies $\mathcal{L}_{\mathcal{AC}}$ in Equation 3.14 to the form

$$\mathcal{L}_{\mathcal{AC}^{2D}} = \begin{bmatrix} 0 & \partial_x & \partial_y \\ \partial_x & 0 & 0 \\ \partial_y & 0 & 0 \end{bmatrix} \tag{3.67}$$

In this configuration, the three-dimensional sphere of influence, as described by Equations 3.23, transforms into two-dimensional spherical means using the method of descent [64] as a particular scenario wherein the z-coordinate has no influence. This transformation results in the sphere of influence taking the shape of a disc, where the function is averaged over the surface area of the disc.

$$M_R\{f\}(x_0, y_0) = \frac{1}{2\pi R} \int_{\theta_P}^{\theta_Q} \int_0^R f(x_0 + r\cos\theta, y_0 + r\sin\theta) \frac{r}{\sqrt{R^2 - r^2}}\, dr\, d\theta \tag{3.68}$$

Within the Active Flux framework, the integration of two-dimensional spherical means takes place across discs having a radius of $R = a_0 \Delta t$, which are centered on degrees of freedom established by the element. This process is depicted in Figure 3.7. The procedure entails carrying out a partial integration of the disc individually within each element. The range of angular integration is determined by the intersection of the integral disc with the edges of the element. At each vertex, both a starting angle θ_P and an ending angle θ_Q are defined, subject to the condition $\theta_Q > \theta_P$. For edge nodes, solely θ_P is necessary since $\theta_Q - \theta_P = \pi$ is always inferred based on the geometry.

The exact solution is approximated through the reconstruction of elements, followed by the utilization of Equation 3.38, and if necessary, Equation 3.39 for Hermite elements. At

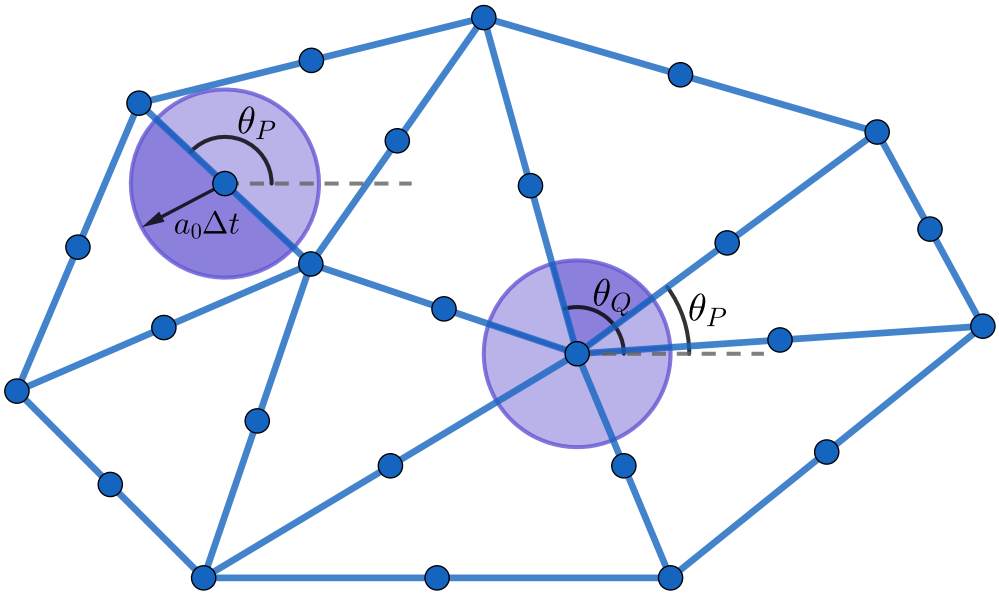

Figure 3.7: Integration of spherical means in two-dimensional space

the node (x_j, y_j), the contribution of the solution state q to the spherical means integral is computed from each of the neighboring elements. Similar to the seemingly distinct Godunov method, **we determine the exact solution for approximating data**. This implies that Equation 3.68 takes the form

$$\begin{aligned} M_R\{q\}(x_j, y_j) &= \frac{1}{2\pi R}\int_0^{2\pi}\int_0^R q(x_j + r\cos\theta, y_j + r\sin\theta)\frac{r}{\sqrt{R^2 - r^2}}\,dr\,d\theta \\ &= \frac{1}{2\pi R}\sum_{i=1}^{(p+1)(p+2)/2} c_i \int_0^{2\pi}\int_0^R b_i(\sigma_1, \sigma_2, \sigma_3)\frac{r}{\sqrt{R^2 - r^2}}\,dr\,d\theta \end{aligned} \tag{3.69}$$

The integral presented in Equation 3.69 might initially appear complex. However, taking into account that the basis functions $b_i(\sigma_1, \sigma_2, \sigma_3)$ are polynomial expressions in barycentric coordinates that possess linear correlation with the Cartesian coordinates (x, y) through Equation 2.6, and then transforming to polar coordinates as,

$$x = x_j + r\cos\theta \tag{3.70}$$

$$y = y_j + r\sin\theta \tag{3.71}$$

the integrals that need to be computed are of the form

$$I_{(p_1,p_2)} = \int_{\theta_P}^{\theta_Q}\int_0^R \frac{(r\cos\theta)^{p_1}\,(r\sin\theta)^{p_2}}{\sqrt{R^2 - r^2}}\,dr d\theta \quad \text{and} \quad 0 \le p_1 + p_2 \le p \tag{3.72}$$

that can be found in inexpensive closed form as

$$I_{(p_1,p_2)} = R^{(p_1+p_2)}\Bigg(a_0(\theta_Q - \theta_P) + \sum_{i=1}^{p_1+p_2} a_i\left[\cos(i\theta_Q) - \cos(i\theta_P)\right] + b_i\left[\sin(i\theta_Q) - \sin(i\theta_P)\right]\Bigg) \tag{3.73}$$

where a_i and b_i are constant coefficients of the i^{th} term as detailed in Table B.1. For a more comprehensive understanding of the derivations and coefficients, refer to Appendix B.

The evolution stage is designed as a loop over elements, facilitating the update of information at each degree of freedom. During the processing of a specific element, there is no inherent requirement to possess knowledge regarding the geometry of neighboring elements or the data they encompass. This design characteristic significantly contributes to mitigating any computational intricacies that our method might introduce.

3.3.2.3 Conservation

Following the evolution stage, where the values at the degrees of freedom are updated, the fluxes described by Equation 3.65 are time-averaged to update the element-average, as governed by Equation 3.64. It is essential for the time-average order of the fluxes to align with the one utilized for element reconstruction.

Refer to Figure 3.1, for a second-order element ($p = 2$), employing Simpson's rule in two dimensions is performed as

$$\bar{\boldsymbol{f}} = \frac{1}{6}\left(\underline{\boldsymbol{f}}^n + 4\underline{\boldsymbol{f}}^{n+\frac{1}{2}} + \underline{\boldsymbol{f}}^{n+1}\right) \quad \text{with} \quad \underline{\boldsymbol{f}}^n = \frac{1}{6}\left(\boldsymbol{f}_L^n + 4\boldsymbol{f}_M + \boldsymbol{f}_R^n\right) \tag{3.74}$$

while for a fourth-order element ($p = 4$), the Gauss–Lobatto rule is utilized to average the fluxes.

$$\bar{\boldsymbol{f}} = \frac{1}{12}\left[\underline{\boldsymbol{f}}^n + 5\left(\underline{\boldsymbol{f}}^{n+\frac{1-\sqrt{1/5}}{2}} + \underline{\boldsymbol{f}}^{n+\frac{1+\sqrt{1/5}}{2}}\right) + \underline{\boldsymbol{f}}^{n+1}\right]$$
$$\text{with} \quad \underline{\boldsymbol{f}}^n = \frac{1}{60}\left(14(\boldsymbol{f}_L^n + \boldsymbol{f}_R^n) + \boldsymbol{f'}_L^n + \boldsymbol{f'}_R^n + 32\boldsymbol{f}_M\right) \tag{3.75}$$

In Equation 3.75, $\boldsymbol{f'}$ is the flux derivative along the edge pointing to the midpoint of the edge.

Subsequently, these averaged fluxes are employed to update the element-averages in a

manner akin to the FV method:

$$\bar{\boldsymbol{q}}^{n+1} = \bar{\boldsymbol{q}}^{n} - \frac{\Delta t}{\boldsymbol{\Omega}_i} \sum_{j=1}^{3} (\bar{\boldsymbol{f}}_j \cdot \hat{n}_j) l_j \tag{3.76}$$

Here, $\boldsymbol{\Omega}_i$ signifies the area of element i, while $\hat{n}_j$ and l_j correspond to the normal vector and length associated with edge j respectively. This equation embodies the conservation law presented by Equation 3.64 governing the update of element-averages.

3.3.2.4 Correction

As also observed in one-dimensional elements, as detailed in Section 3.3.1.4, the utilization of the *independent* update approach during the evolution stage does not inherently guarantee that the element-average obtained from the conservation stage will match the average derived from the reconstruction process. This characteristic will be extended to two-dimensional elements as well. The resulting inconsistency can be quantified as

$$d\bar{\boldsymbol{q}}_i = \bar{\boldsymbol{q}}_i - \frac{1}{\boldsymbol{\Omega}_i} \sum_{j=1}^{(p+1)(p+2)/2} \boldsymbol{c}_j \iint_{\boldsymbol{\Omega}_i} \boldsymbol{b}_j \, d\boldsymbol{\Omega} \tag{3.77}$$

To ensure conservation, we adhere to the same principles as outlined in the one-dimensional case in Section 3.3.1.4.

Conservation must be enforced to ensure

$$\sum_{i=1}^{N} d\bar{\boldsymbol{q}}_i \boldsymbol{\Omega}_i = 0 \tag{3.78}$$

with N representing the total number of elements.

Through the distribution of this inconsistency across the information within each element,conservation, as expressed in Equation 3.78, is upheld. Considering that an element $\boldsymbol{\Omega}_i$ encompasses $(p+1)(p+2)/2$ degrees of freedom, encompassing both values $\boldsymbol{q}_{i_{(j)}}$ and gradients $\partial \boldsymbol{q}_{i_{(j)}}$ at the location j, the inconsistency $d\bar{\boldsymbol{q}}_i$ is allocated solely to the values in the following manner

$$\boldsymbol{q}_{i_{(j)}} := \boldsymbol{q}_{i_{(j)}} + \alpha_{i_{(j)}} d\bar{\boldsymbol{q}}_i \tag{3.79}$$

where $\alpha_{i_{(j)}}$ is a correction weight that is determined to satisfy the fundamental conservation

criterion, as highlighted by He et al. [71]:

$$\frac{1}{\boldsymbol{\Omega}_i} \sum_{j=\text{value basis only}} \alpha_{i_{(j)}} \iint_{\boldsymbol{\Omega}_i} \boldsymbol{b}_j \, d\boldsymbol{\Omega} = 1 \tag{3.80}$$

This actually adjusts the reconstructed $\boldsymbol{q}_i$ by shifting it orthogonally in the spatial domain. Nevertheless, this process introduces discontinuities at element interfaces due to the fact that, in general, $d\bar{\boldsymbol{q}}_i \neq d\bar{\boldsymbol{q}}_j$ for $i \neq j$.

To mitigate this, the modified values of neighboring elements at shared locations are averaged. Assuming that Eq. 3.79 has altered the values of $\boldsymbol{q}_{i_{(j)}}$ for s elements at the common location j, the $\boldsymbol{q}_{i_{(j)}}$ at this specific location is averaged as

$$\boldsymbol{q}_{i_{(j)}} := \frac{\sum_{i=1}^{s} \boldsymbol{q}_{i_{(j)}} \boldsymbol{\Omega}_i}{\sum_{i=1}^{s} \boldsymbol{\Omega}_i} \tag{3.81}$$

This approach ensures conservation in Eq. 3.78 without introducing any discontinuities.

3.3.2.5 Boundary Conditions

Frequently, boundary conditions such as radiative (open), interfaces, etc., are responsible for considerable numerical inaccuracies observed in computational acoustics or computational fluid dynamics methods [73].

For instance, the radiation condition is among the most difficult boundary conditions to handle. This is where the method should allow the outgoing wave to exit the domain without unwanted reflections within the domain. Several kinds of open boundary conditions have been established to address the open-domain issue. These include far-field asymptotic solutions [74], the buffer zone technique [75], the perfectly matched layer technique [76], and characteristic-based inflow and outflow boundary conditions [77]. The latter is favorable for upwinding-feature schemes and usually functions optimally when the wave angle is perpendicular to the boundary. However, its performance may decline when the wave angle strays from normal, resulting in errors as much as $3-5$ percent for larger incidence angles [78, 79].

The active flux method inherently handles boundary conditions by utilizing its built-in features. It accomplishes this by computing the spherical means over the disc of influence, which are determined based on the requirements of the boundary condition. These conditions can include, open, and interface boundaries.

In Figure 3.8, the illustration demonstrates that individual cells in the simulation can have distinct propagation speeds. This is noticeable from the varying radii of integration domains around the nodes in two different materials. A modified version of this technique is

employed at open boundaries, where contributions from outside the domain are disregarded. This is due to the fact that no elements, including ghost elements, are positioned beyond the domain boundary. It should be noted that this approach is consistent with the concept of placing ghost elements with $a_0 = 0$.

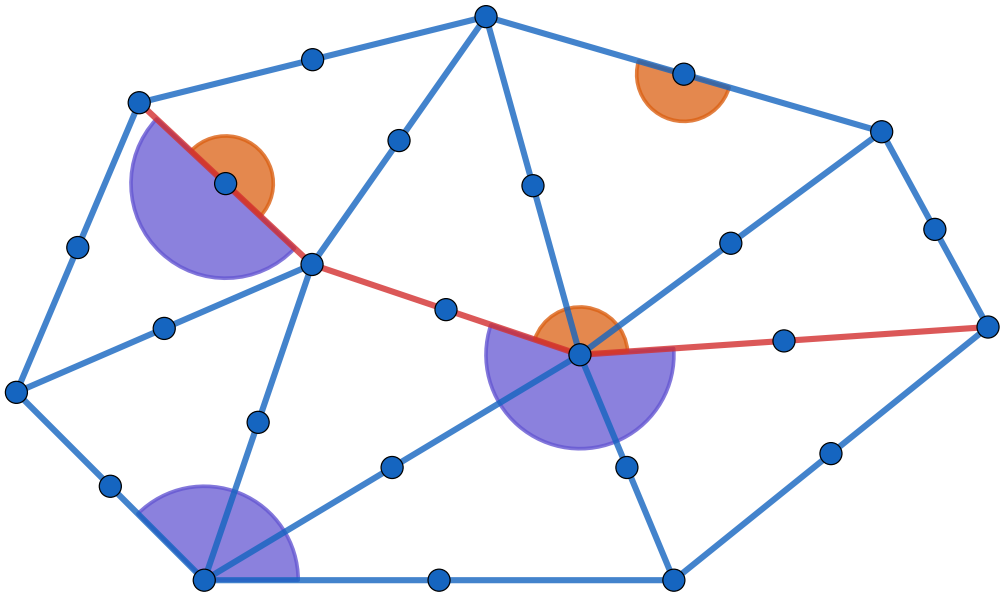

Figure 3.8: Node location and regions of dependence. The sound speed is smaller in the uppermost four elements

We have determined that there is no necessity for incorporating absorbing layers or similar devices in our simulations. While this radiation condition is not flawless, it is important to recognize that there is no existing local boundary condition that can precisely simulate an unbounded domain with more than one dimension. The quest for a suitable practical methodology in this regard has a lengthy history [78]. A recent and comprehensive review from the perspective of elastic waves can be found in [80]. Despite its imperfections, our proposed radiation condition performs just as well or even better than the approximations currently in use. Additionally, we can demonstrate that it does not require the utilization of excessively large domains.

3.3.2.6 Smooth Solution

We initially evaluate the accuracy of the AF scheme using a smooth solution with a fourth-order Hermite element ($p = 4$) presented in Figure 2.6b. This choice is expected to yield fifth-order accuracy since the dominant error term is of order five. We adopt the initial

conditions suggested by Lukacova-Medivid'ova, Morton, and Warnecke. [72].

$$p(x, y, 0) = \frac{1}{a_0}[\sin(2\pi x) + \sin(2\pi y)]$$
$$u(x, y, 0) = v(x, y, 0) = 0 \tag{3.82}$$

The double sine waves problem possesses an analytical solution comprising standing waves.

$$p(x, y, t) = \frac{1}{a_0}\cos(2\pi a_0 t)[\sin(2\pi x) + \sin(2\pi y)]$$
$$u(x, y, t) = \frac{1}{a_0}\sin(2\pi a_0 t)\cos(2\pi x)$$
$$v(x, y, t) = \frac{1}{a_0}\sin(2\pi a_0 t)\cos(2\pi y) \tag{3.83}$$

The calculations are performed within a square domain of length 1, utilizing a fully unstructured grid with a sound speed set to $a_0 = 1$. To establish a Courant number, we introduce a length scale derived from the number of elements. In the case of a square $n \times n$ grid, the element count would be $N = 2n^2$, and the length scale can be expressed as $L = n^{-1}$. For general grids, we assume a relationship $L = (N/2)^{-1/2}$.

Figure 3.9 illustrates the temporal evolution of a double sine pressure pulse with a periodic boundary condition.

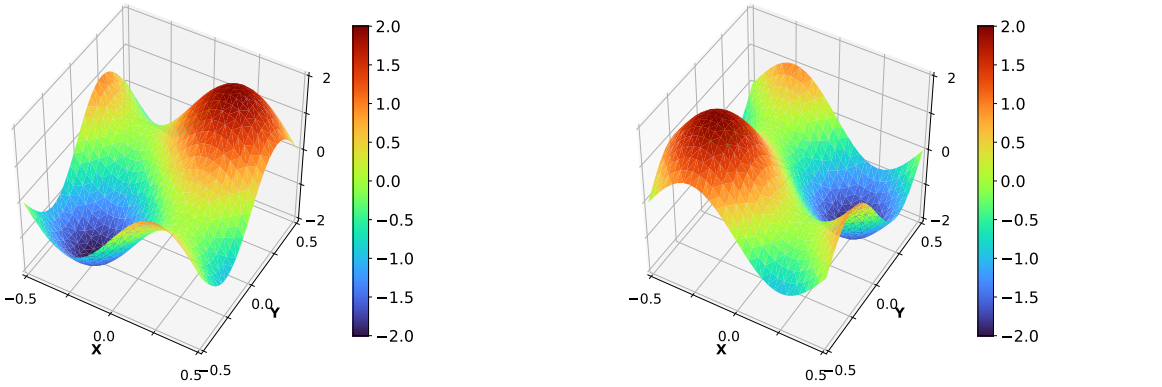

$t = 0.0$ **$t = 0.5$**

Figure 3.9: Active Flux pressure solution for double sine pulse after half a period.

Figure 3.10 displays the L_2 error after a single full period ($t = 1/a_0$) as a function of the mesh size. A Courant number of 0.5 was employed, based on the defined mesh size relationship. Remarkably, the fifth-order method demonstrated remarkable accuracy ($\approx 1\%$)

with just two cells per wavelength, corresponding to a mesh of four squares divided into eight elements. The more ambitious target of 0.1% error is attained with a configuration of nine cells divided into 18 elements, surpassing even the performance of the one-dimensional case. For comparative purposes, the results obtained from the third-order scheme that excludes all gradient information are also presented. These findings suggest that the third-order approach could prove highly valuable as well.

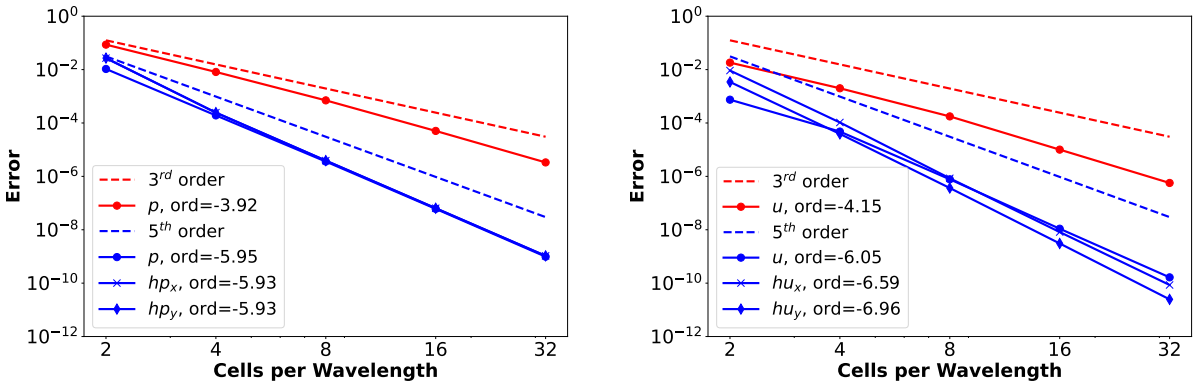

Figure 3.10: Errors after evolution over one period; **left**: pressure, **right**: u-velocity. The results for $\partial_x v, \partial_y v$ are almost the same as those for $\partial_y u, \partial_x u$

It's a common observation that the derivatives of a numerical solution often exhibit an order of accuracy that's one less than the order of accuracy of the point values themselves. To account for this discrepancy, we plotted the errors multiplied by a characteristic mesh size, essentially representing the value error induced by a gradient error.

Interestingly, the measured orders of accuracy for the point values of pressure exceeded our initial expectations. Instead of the anticipated three and five, we observed values of almost four and nearly six for the respective cases. This suggests that the accuracy of our derivatives is actually three and five.

Furthermore, in a somewhat surprising turn, when we measured errors stemming from velocity gradients using the same approach, we obtained slopes of slightly above four and even almost seven(!). While we're unsure if this can be attributed to any specific feature of the problem, these results are indeed encouraging, particularly in the context of extending the methodology to Navier-Stokes equations.

Even when utilizing merely two cells per wavelength, the complete fifth-order scheme showcases remarkable graphical precision, achieving accuracy better than one percent. The third-order approach also maintains its accuracy, being almost five percent precise. These results don't run counter to the Shannon limit, which dictates a minimum of two points

per wavelength, as our inclusion of edge midpoints effectively halves the cell size. Furthermore, this limit doesn't extend to Hermitian schemes that offer supplementary, independent information, encompassing both values and gradients.

The accuracy of the gradients exhibits a noticeable sensitivity to the Courant number. In Figure 3.11, the errors for both schemes are plotted against the Courant number for a mesh with 16 points per wavelength. The depicted range ends at $CFL = 0.7$ and 0.82 due to the stability limits, beyond which the plots cease. Within the stable Courant number range, the accuracy of the gradients experiences a shift of approximately one order of magnitude. This effect is more pronounced than in one dimension, but even the lower accuracy values remain quite satisfactory.

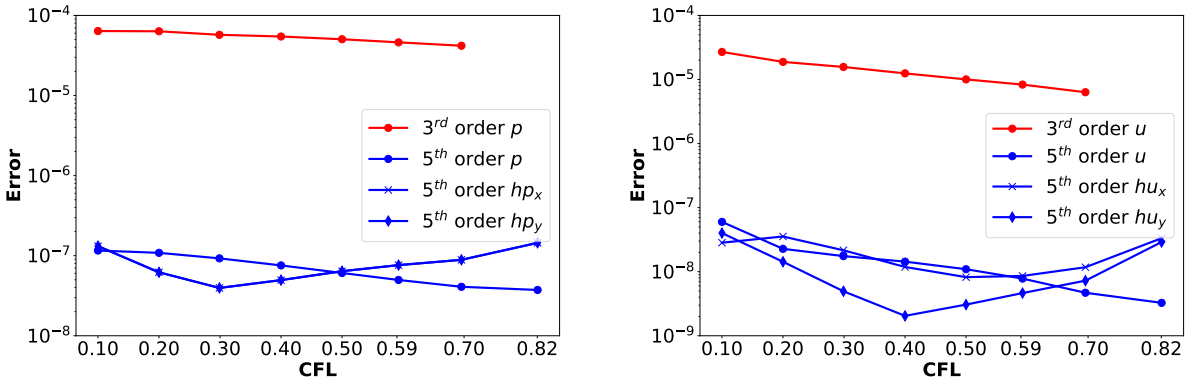

Figure 3.11: Errors after evolution over one period for **16** cells per wavelength; **left**: pressure, **right**: u-velocity. The results for $\partial_x v, \partial_y v$ are almost the same as those for $\partial_y u, \partial_x u$.

3.3.2.7 Square Waves

While in one dimension, the advection of a square wave provided valuable insights into the resolution capabilities of each scheme, the situation is different in the context of acoustics. In one dimension, this scenario could be reduced to an advection problem for each Riemann invariant. However, in the two-dimensional acoustics scenario, a perfect correspondence between the behavior and resolution characteristics might not be readily expected.

We present a problem that combines one-dimensional initial data with a solution implemented on a regular rectangular two-dimensional grid. This choice is motivated by the challenge of initializing discontinuous data on entirely unstructured grids. The problem setup, as presented by Figure 3.12, involves an initially quiescent fluid ($t = 0$) with an elevated pressure in the central half. Following the initiation of discontinuities, outward compression waves and inward rarefaction waves propagate ($t = 0.5$), reaching the boundaries by $t = 1$.

Due to the periodic boundaries, the compression wave departing from the front boundary re-enters at the top, and by $t = 2$, it has advanced a quarter of the domain's length. As time progresses to $t = 4$, the compression wave returns to its initial position, yielding a final solution matching the initial conditions.

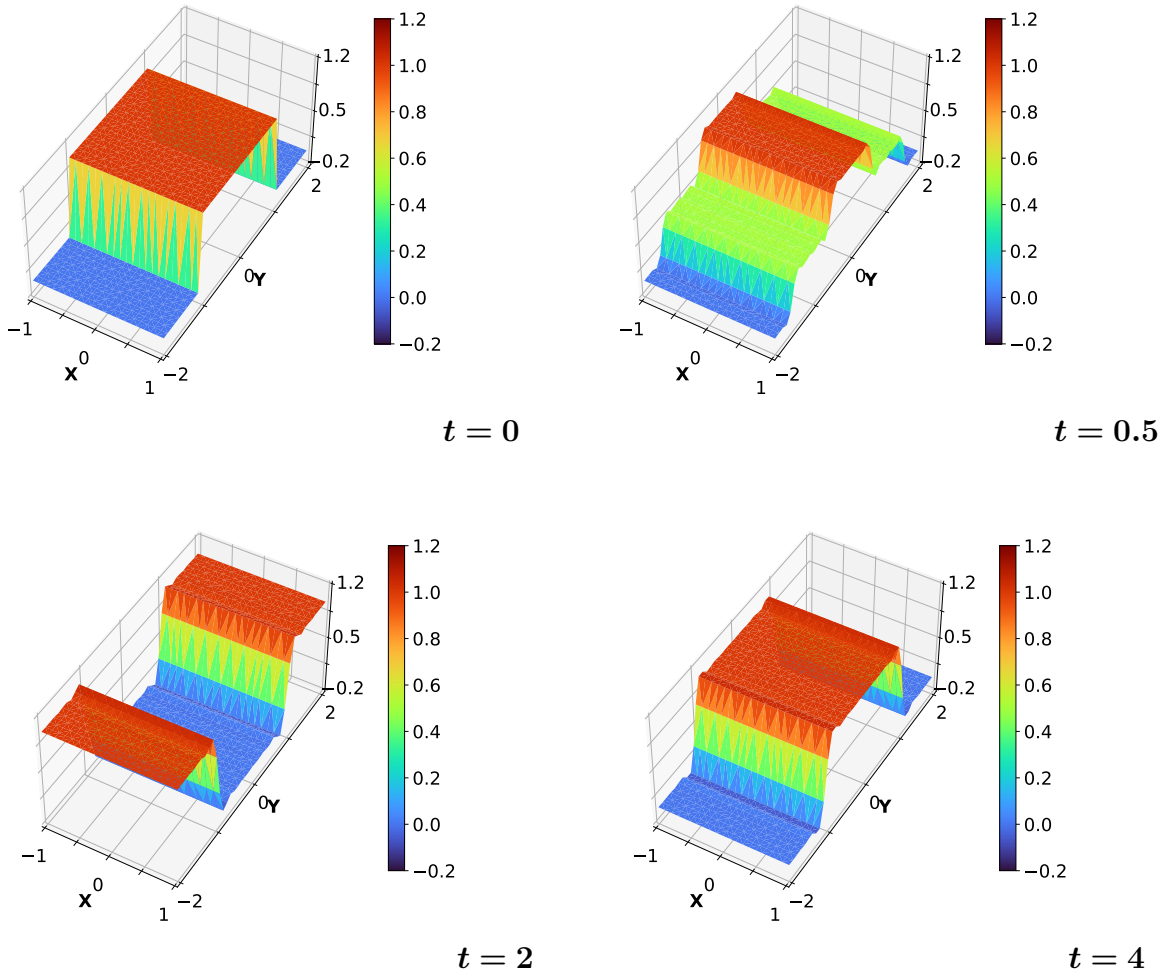

Figure 3.12: Two-dimensional square wave propagated over twice its length as captured by Active Flux of fifth-order accuracy.

Examining Figure 3.13, we observe that the solutions exhibit a slightly diminished accuracy compared to their one-dimensional counterparts. A general observation might suggest that within each shock transition, the third-order scheme roughly contains seven points instead of four. However, for the fifth-order scheme, the agreement is remarkably close. Importantly, there is no detectable error in the phase of the waves; they have precisely returned to their initial positions.

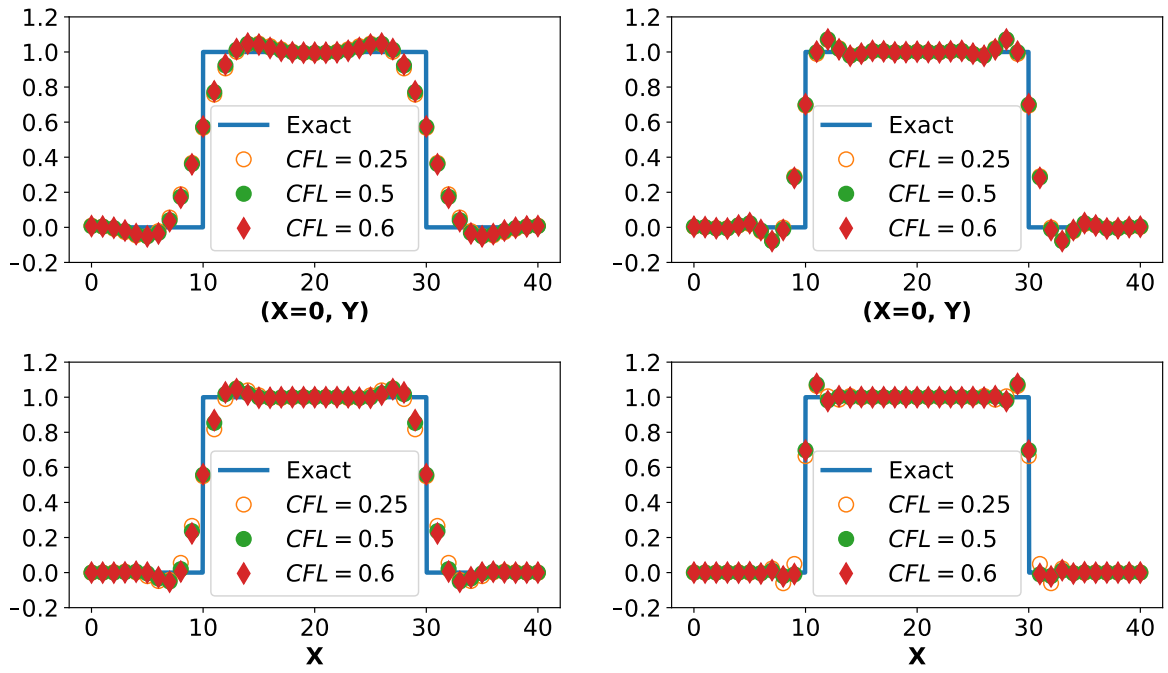

Figure 3.13: Two-dimensional square pressure waves (top) along the centerline $(x = 0, y)$ and one-dimensional square pressure waves (bottom), both propagated over three times their length as captured by Active Flux of (left) 3rd and (right) 5th-order accuracy.

3.3.2.8 Radiation Conditions

Our third test scenario is chosen specifically to showcase the distinctive characteristics of this scheme near boundaries. This concept has been previously introduced in relation to Figure 3.8. The primary premise is that there are no elements whatsoever outside the designated domain. Boundary vertices are exclusively updated by elements located within the boundary. We operate under the assumption that if elements were present outside the boundary, either their internal gradients would be exceedingly small or they would only generate outgoing waves, which we can afford to disregard. Given this presumption, it isn't necessary to position the boundary at an extensive distance. The domain under consideration is a simple square, and the mesh is composed of 15×15 squares, each bisected by the same diagonal.

Figure 3.14 illustrates the progression of events. In the upper left corner, we visualize the initial data $(t = 0)$ featuring a narrow Gaussian hill captured over a 3×3 cell path. To the right, we observe the outgoing circular wave just before reaching the boundary, maintaining its compact support. Moving to the bottom half of the figure, the solution at a later time $(t = 2)$ is presented. The effect of wall boundary conditions on the left side of the domain is manifested through the presence of numerous waves. On the right side, the outcome of our straightforward radiation condition, which nullifies incoming contributions to the spherical

mean, is evident; the remaining disturbance is eradicated.

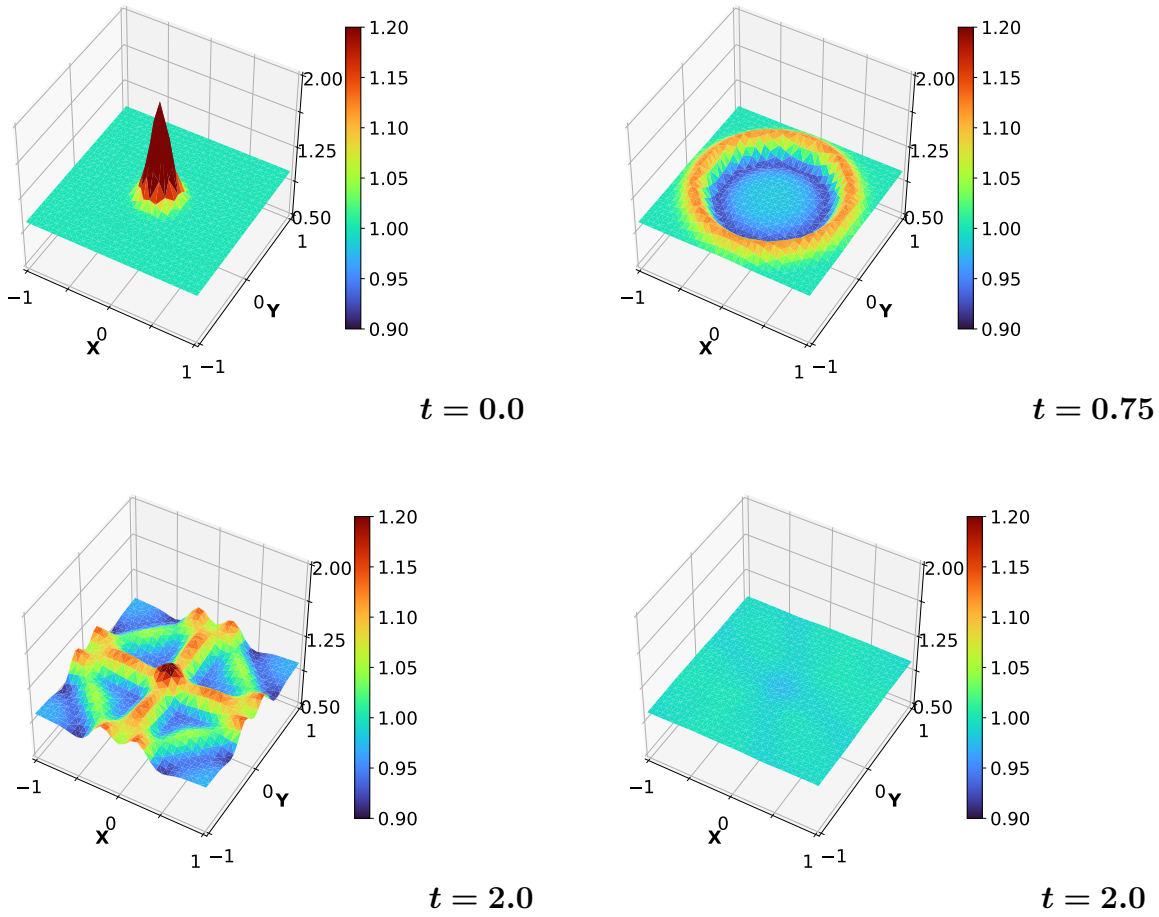

Figure 3.14: Active Flux pressure solution for Gaussian pulse; **top left:** initial conditions, **top right:** just before exit, **bottom left:** periodic boundary, **bottom right:** open boundary.

3.3.2.9 Multiple Materials and Vorticity

Our fourth test problem, as depicted in Figure 3.15, serves to highlight the effectiveness of the interface condition. In this scenario, the domain takes the form of a rectangle with an aspect ratio of 2. Each half of the domain features a different propagation speed, with a speed of 1.0 at the top and 2.5 at the bottom. It's important to note that in a one-dimensional acoustic setting, a change in wave speed doesn't impact the eigenvectors of the system. Consequently, simple waves passing through an interface merely alter their velocity and are not reflected. This conclusion holds true in higher dimensions as well, provided that

the wave arrives at an almost normal angle. If the incidence is notably oblique, there will naturally be some reflection at the original speed.

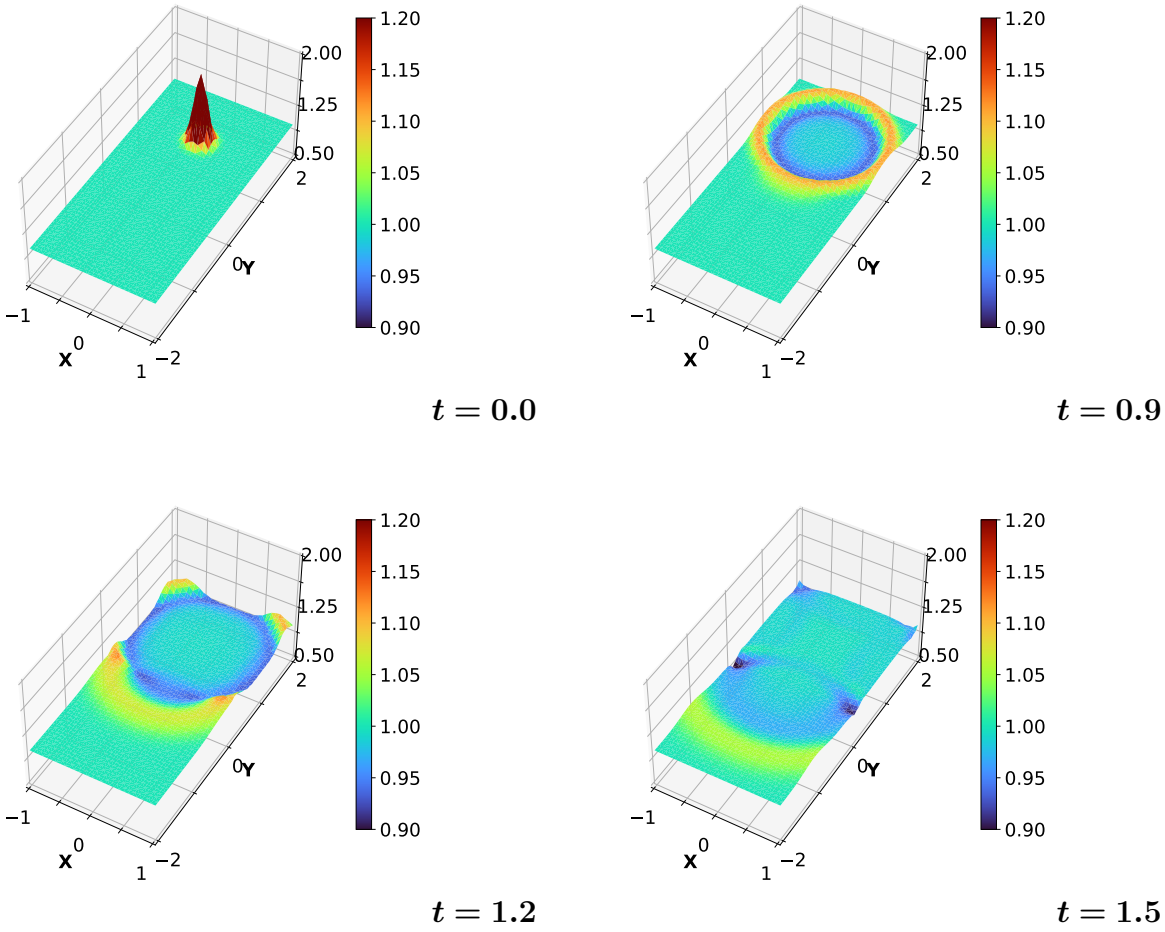

Figure 3.15: Active Flux pressure solution for Gaussian pulse; **top left:** initial condition, **top right:** wave starting to cross boundary, **bottom left:** wave continues in faster material, and **bottom right:** a very weak wave reflects in the original material (and would not exist in one dimension).

In our fourth test problem, the mesh consists of 14×30 squares divided by their NE/SW diagonals. We employ the same Gaussian hill to initiate the problem in the upper half of the domain (top left). At $t = 0.9$ (top right), the wave is on the cusp of leaving the slow material. By $t = 1.2$ (bottom left), it has crossed parts of the boundary. In regions where we have implemented a radiation condition (left, right, and top), no reflections are evident.

Along the boundary $y = 0$ with the faster material, the wave propagates at an increased speed. There is no discernible reflection back into the slow material because the wave crosses the boundary almost perpendicularly. At $t = 1.5$ (bottom right), this portion of the wave

continues, but we begin to observe some reflection from the more oblique parts of the wave. Additionally, we can see two "dimples" in the pressure field, situated close to but not exactly at the boundaries. These dimples result from vortices generated at the interface. Similar to the initial conditions, these features exhibit a well-defined width of approximately two cells.

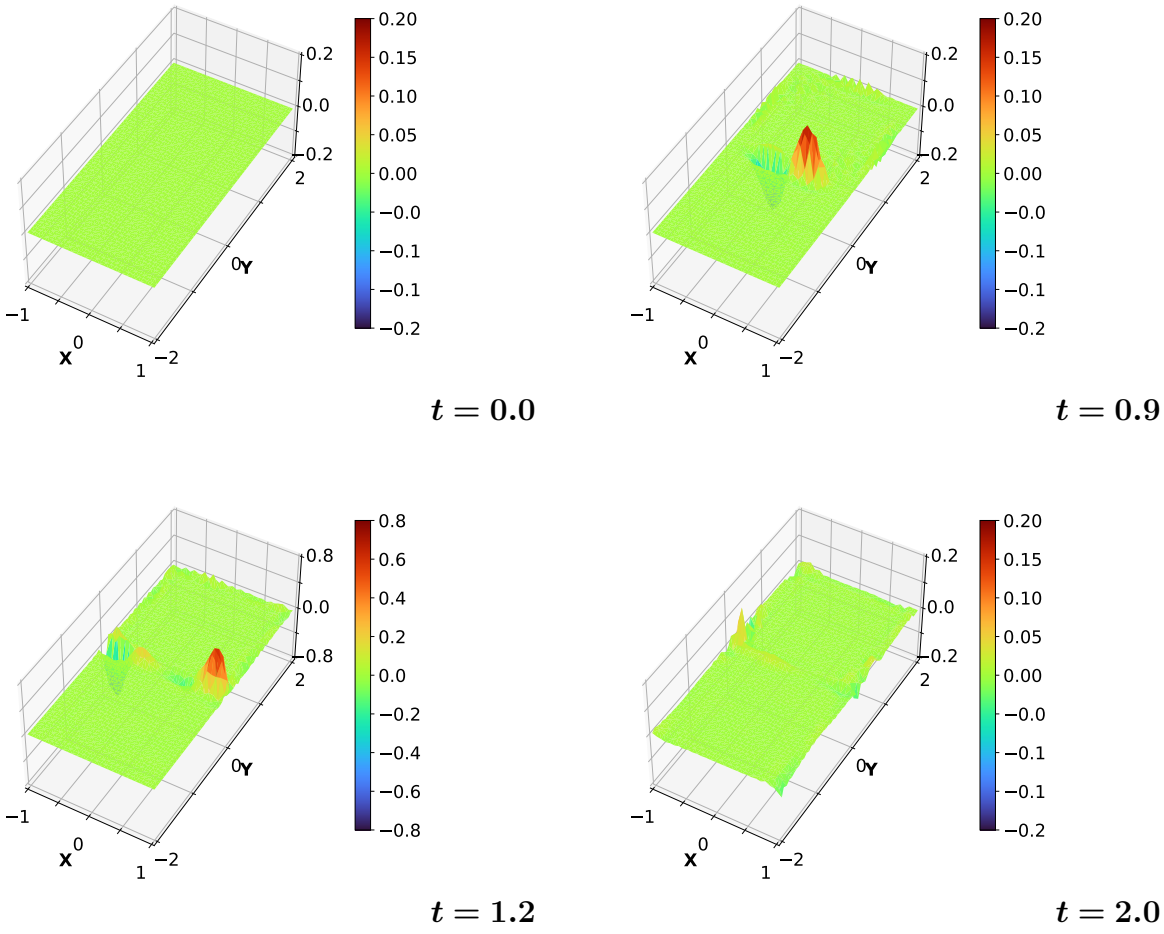

Figure 3.16: Active Flux Vorticity for Gaussian pulse; **top left:** initial condition, **top right:** wave starting to cross the interface, small vorticity just visible. **bottom left:** vorticity strengthens and moves outward, **bottom right:** vorticity has left the domain. Notice the different vertical scales.

In Figure 3.16, we examine the vorticity in the simulation. At $t = 0.0$, the vorticity is naturally absent. By $t = 0.9$, the flow remains irrotational, except where it has begun to cross into the second material. Here, vorticity is generated at a rate of $\nabla a_0 \times \nabla p = \partial_y a_0 \cdot \partial_x p$. Initially, very little vorticity is produced because $\partial_x p$ is very small. However, if we focus on a specific location along the interface, we observe a pressure gradient that changes sign as the wave passes, resulting in the creation and subsequent destruction of vorticity (Figure

3.16). This transient vorticity gives the appearance of a pair of vortices with opposite signs moving outward from initial positions near the center.

In the final image at $t = 2$, we plot the vorticity and observe that it has disappeared. If we had refined the mesh in the vicinity of the interface, ∇a_0 would have been larger, resulting in more intense vorticity production within a smaller region.

CHAPTER 4

Elastodynamics: Hermite Methods for Elastic Wave Propagation

Acoustic waves within an isotropic medium, uniformly travel in all directions at a constant speed. It is increasingly recognized that in such scenarios, employing conventional one-dimensional upwinding methods yields little to no discernible advantage, primarily due to the upwind dissipation matrix being a mere scalar. Lung et al. [81] demonstrated that a suitably parameterized Lax-Wendroff method can yield exceptional outcomes, encompassing the exact preservation of the vorticity constraint and optimal isotropic behavior[1]

The situation becomes more intricate in the context of elastodynamics, where we encounter a dual isentropic problem. This comprises P-waves, generating oscillations perpendicular to the wavefront and traveling at speed a_P, and S-waves, creating oscillations parallel to the wavefront and moving at speed a_S, approximately half the speed of the P-waves. Due to the differing magnitudes of these wavespeeds and the dependence of optimal dissipation on the Courant number, the dissipation matrix is no longer scalar. Consequently, it becomes imperative to treat each type of wave uniquely. Fortunately, in linear elastodynamics, both types of waves can be described through separate second-order wave equations. These equations govern a scalar potential for irrotational P-waves and a vector potential for solenoidal S-waves. These waves essentially operate independently within the domain's interior, with coupling usually occurring only at the boundaries, where the prescribed behavior typically pertains to both types of waves causing them to interact.

Nakazawa [82] conducted a Helmholtz decomposition to separate the elastodynamic equations into two distinct first-order systems, with each system exclusively addressing either P-waves or S-waves. Subsequently, the upwind leapfrog method [83] was applied independently to each system. For this purpose, a mesh of size h was employed for P-waves, while a

[1] A similar scenario arises when considering Maxwell's equations, which encompass a pair of isotropic problems—one for the electric field and another for the magnetic field. In both cases, the wavespeed remains constant, resulting in the dissipation matrix once again being scalar in nature.

mesh of size $h/2$ was used for S-waves. This mesh configuration ensured that each wave was computed with an approximately optimal Courant number. The results presented in this thesis are notably well-defined and encompass a range of scenarios, including wave reflection problems and situations involving Rayleigh, Stoneley, Lamb, and Love waves.

In this chapter, each system is solved using the high-order AF method introduced in Chapter 3. In our numerical setup, we exclusively consider open boundaries where the coupling between the two systems does not occur. These open boundaries are managed using the built-in capabilities of the AF method. We may provide information about the treatment of free and rigid boundaries in the near future. The rates of stress are calculated using the gradient update of the Hermite element, which imposes no additional computational load.

4.1 Helmholtz Decomposition

Let $\bar{\boldsymbol{u}}(t, \boldsymbol{x})$, represent~~ing~~ the displacement of a material particle situated at position $\boldsymbol{x}$, and $\boldsymbol{\sigma}(t, \boldsymbol{x})$, represent~~ing~~ the Cauchy stress tensor. We make the assumption that the material is homogeneous and isotropic, and the equations governing the evolution of displacement are those of linear elasticity

$$\rho \bar{\boldsymbol{u}}_{tt} = \nabla \cdot \boldsymbol{\sigma} \tag{4.1}$$

where, ρ represents the material density, which is assumed to remain constant. The stress tensor is related to the strain tensor through the equation

$$\boldsymbol{\sigma} = \lambda(\nabla \cdot \bar{\boldsymbol{u}})\boldsymbol{I} + 2\mu\boldsymbol{\epsilon} \tag{4.2}$$

Here, λ and μ are the Lamé parameters, which are related to Young's modulus E and Poisson's ratio ν by

$$\lambda = \frac{\nu E}{(1+\nu)(1-2\nu)} \quad \text{and} \quad \mu = \frac{E}{2(1+\nu)} \tag{4.3}$$

and the strain tensor $\boldsymbol{\epsilon}$ is given by

$$\boldsymbol{\epsilon} = \frac{1}{2}(\boldsymbol{\mathcal{D}}^T + \boldsymbol{\mathcal{D}}) \quad \text{with} \quad \boldsymbol{\mathcal{D}} = \nabla \bar{\boldsymbol{u}} \tag{4.4}$$

Elastodynamics equations can also be expressed as a first-order system, taking the form

$$\bar{\boldsymbol{u}}_t = \boldsymbol{u} \tag{4.5}$$

$$\rho \boldsymbol{u}_t = \nabla \cdot \boldsymbol{\sigma} \tag{4.6}$$

$$\boldsymbol{\sigma}_t = \lambda(\nabla \cdot \boldsymbol{u})\boldsymbol{I} + 2\mu\dot{\boldsymbol{\epsilon}} \tag{4.7}$$

Here, $\boldsymbol{u}$ represents the velocity field, and $\dot{\boldsymbol{\epsilon}}$ denotes the rate of strain tensor, defined as

$$\dot{\boldsymbol{\epsilon}} = \frac{1}{2}(\dot{\boldsymbol{\mathcal{D}}}^T + \dot{\boldsymbol{\mathcal{D}}}) \quad \text{with} \quad \dot{\boldsymbol{\mathcal{D}}} = \nabla \boldsymbol{u} \tag{4.8}$$

Let's consider expressing the velocity vector $\boldsymbol{u}$ in terms of a scalar potential Φ and a vector potential $\boldsymbol{\Psi}$ [82]

$$\boldsymbol{u} = \nabla\Phi + \nabla \times \boldsymbol{\Psi} \tag{4.9}$$

In this expression, the first term corresponds to an irrotational component, while the second term represents a solenoidal component.

In accordance with the explanation provided in [84], the elastodynamic equation represented by Equation 4.1 is expressed as

$$\rho\bar{\boldsymbol{u}}_{tt} = (\lambda + 2\mu)\nabla(\nabla \cdot \bar{\boldsymbol{u}}) - \mu\nabla \times \nabla \times \bar{\boldsymbol{u}} \tag{4.10}$$

Consequently, substituting Equation 4.9 into Equation 4.10, we obtain

$$\nabla\left(a_P^2\nabla^2\Phi - \Phi_{tt}\right) - \nabla \times \left(a_S^2\nabla \times \nabla \times \boldsymbol{\Psi} + \boldsymbol{\Psi}_{tt}\right) = \boldsymbol{0} \tag{4.11}$$

For this equation to be satisfied, the P-wave equation

$$a_P^2\nabla^2\Phi = \Phi_{tt} \quad \text{with} \quad a_P = \sqrt{\frac{\lambda + 2\mu}{\rho}} \tag{4.12}$$

and the S-wave equation

$$a_S^2\nabla \times \nabla \times \boldsymbol{\Psi} = -\boldsymbol{\Psi}_{tt} \quad \text{with} \quad a_S = \sqrt{\frac{\mu}{\rho}} \tag{4.13}$$

are sufficient. By applying the well-known vector identity

$$\nabla \times \nabla \times \boldsymbol{\Psi} = \nabla(\nabla \cdot \boldsymbol{\Psi}) - \nabla^2\boldsymbol{\Psi} \tag{4.14}$$

to Equation 4.13, we transform the S-wave equation into

$$a_S^2\nabla^2\boldsymbol{\Psi} = \boldsymbol{\Psi}_{tt} \quad \text{with} \quad a_S = \sqrt{\frac{\mu}{\rho}} \tag{4.15}$$

Here, we require that $\nabla \cdot \boldsymbol{\Psi}$ remains constant. While this constant can have arbitrary values, it is often convenient to set it to zero. In the general representation of a vector field $\boldsymbol{u}$

by Equation 4.9, where $\nabla \cdot \boldsymbol{\Psi} = \mathbf{0}$, is commonly known as the Helmholtz decomposition. Through this decomposition, the original vector field is separated into two components: one originating from a scalar potential denoted by $\boldsymbol{u}_P = \nabla\Phi$, and the other from a vector potential represented by $\boldsymbol{u}_S = \nabla \times \boldsymbol{\Psi}$. The scalar potential is characterized by its irrotational nature: $\nabla \times \boldsymbol{u}_P = \mathbf{0}$, while the vector potential is divergence-free: $\nabla \cdot \boldsymbol{u}_S = 0$.

Equation 4.12 and Equation 4.15 represent well-known scalar wave equations that describe two types of waves, P- and S- waves, each propagating at distinct speeds, a_P and a_S, respectively. These waves propagate independently, with no interaction between them except at boundaries in the presence of heterogeneities.

4.1.1 Formulation in Two Dimensions

In this section, we specialize the equations to a two-dimensional scenario[2]. In two dimensions, the velocity components are expressed as

$$u = \Phi_x + \Psi_y \tag{4.16}$$

$$v = \Phi_y - \Psi_x \tag{4.17}$$

Here, Ψ represents the non-zero component of the vector potential $\boldsymbol{\Psi} = (0, 0, \Psi)$.

The expression for stress rates can also be formulated using potential functions, given by

$$\dot{\sigma}_{xx} = \lambda(u_x + v_y) + 2\mu u_x = \lambda\nabla^2\Phi + 2\mu(\Phi_{xx} + \Psi_{yx}) \tag{4.18}$$

$$\dot{\sigma}_{yy} = \lambda(u_x + v_y) + 2\mu v_y = \lambda\nabla^2\Phi + 2\mu(\Phi_{yy} - \Psi_{xy}) \tag{4.19}$$

$$\dot{\sigma}_{xy} = \mu(u_y + v_x) = \mu(2\Phi_{xy} + \nabla^2\Psi) \tag{4.20}$$

$$\dot{\sigma}_{yx} = \mu(v_x + u_y) = \mu(2\Phi_{yx} + \nabla^2\Psi) \tag{4.21}$$

These equations conform to the principle of angular momentum conservation, resulting in $\dot{\sigma}_{xy} = \dot{\sigma}_{yx}$.

Next, we will introduce additional variables, represented as σ and ω:

$$\sigma_t = (\lambda + 2\mu)(u_x + v_y) = (\lambda + 2\mu)\nabla^2\Phi \tag{4.22}$$

$$\omega_t = \mu(v_x - u_y) = -\mu\nabla^2\Psi \tag{4.23}$$

The variable σ is solely derived from Φ, making it associated with the P-wave system. Therefore, this variable signifies the compression or expansion of a material. Conversely, ω

[2]Moving forward, we will simplify our calculations by assuming that $\rho = 1$.

is linked to the S-wave system, and as such, it indicates the rotation along the z-axis of the material.

Using the new variables σ and ω, we can derive the first time derivatives of the velocity components. Beginning with Equation 4.16 and taking the second time derivative, we have

$$u_{tt} = (\Phi_x)_{tt} + (\Psi_y)_{tt} \tag{4.24}$$

By using Equations 4.12 and 4.15, along with Equations 4.22 and 4.23, we can express this equation as

$$u_{tt} = (a_P^2 \nabla^2 \Phi)_x + (a_S^2 \nabla^2 \Psi)_y = (\sigma_t)_x - (\omega_t)_y \tag{4.25}$$

Now, by integrating Equation 4.25 over time to obtain u_t, we get

$$u_t = \sigma_x - \omega_y \tag{4.26}$$

Similarly, starting from Equation 4.17, we obtain

$$v_t = \omega_x + \sigma_y \tag{4.27}$$

Hence, the expressions for the decomposed systems are as follows:

- P-wave subsystem

$$\partial_t \begin{pmatrix} \sigma \\ u_P \\ v_P \end{pmatrix} = \begin{bmatrix} 0 & a_P^2 \partial_x & a_P^2 \partial_y \\ \partial_x & 0 & 0 \\ \partial_y & 0 & 0 \end{bmatrix} \begin{pmatrix} \sigma \\ u_P \\ v_P \end{pmatrix} \tag{4.28}$$

- S-wave subsystem

$$\partial_t \begin{pmatrix} \omega \\ u_S \\ v_S \end{pmatrix} = \begin{bmatrix} 0 & -a_S^2 \partial_y & a_S^2 \partial_x \\ -\partial_y & 0 & 0 \\ \partial_x & 0 & 0 \end{bmatrix} \begin{pmatrix} \omega \\ u_S \\ v_S \end{pmatrix} \tag{4.29}$$

This completes Nakazawa's [82] two-dimensional decomposition of the elastodynamic equations that we will employ here [3].

In this decomposition, the calculation of stresses for the P-wave and S-wave subsystems can be carried out independently as secondary computations derived from the primary com-

[3]However, the complete three-dimensional decomposition in (4.12) and (4.13) is also amenable to treatment by the Active Flux technique, and we hope to report on this shortly.

putations in Equation 4.28 and 4.29.

$$\partial_t \begin{pmatrix} \sigma_{xx_P} \\ \sigma_{yy_P} \\ \sigma_{xy_P} \\ \sigma_{yx_P} \end{pmatrix} = \begin{bmatrix} a_P^2\partial_x & \alpha a_P^2\partial_y \\ \alpha a_P^2\partial_x & a_P^2\partial_y \\ a_S^2\partial_y & a_S^2\partial_x \\ a_S^2\partial_y & a_S^2\partial_x \end{bmatrix} \begin{pmatrix} u_P \\ v_P \end{pmatrix}, \quad \partial_t \begin{pmatrix} \sigma_{xx_S} \\ \sigma_{yy_S} \\ \sigma_{xy_S} \\ \sigma_{yx_S} \end{pmatrix} = \begin{bmatrix} a_P^2\partial_x & \alpha a_P^2\partial_y \\ \alpha a_P^2\partial_x & a_P^2\partial_y \\ a_S^2\partial_y & a_S^2\partial_x \\ a_S^2\partial_y & a_S^2\partial_x \end{bmatrix} \begin{pmatrix} u_S \\ v_S \end{pmatrix} \tag{4.30}$$

where α is given by

$$\alpha = 1 - 2\left(\frac{a_S}{a_P}\right)^2 \tag{4.31}$$

Lastly, this decomposition reassembles the variables $\boldsymbol{u}$ and $\boldsymbol{\sigma}$ using

$$\boldsymbol{u} = \boldsymbol{u}_P + \boldsymbol{u}_S \quad \text{and} \quad \boldsymbol{\sigma} = \boldsymbol{\sigma}_P + \boldsymbol{\sigma}_S \tag{4.32}$$

Equations 4.28 and 4.29 are independently solved as the primary calculations for the elastodynamic system, and the stresses may be subsequently computed as secondary calculations if required from Equation 4.30.

4.2 Hermite Active Flux Numerical Formulation

By taking Equation 4.28 and introducing the variable σ^* defined as

$$\sigma = -a_P\sigma^* \tag{4.33}$$

We can express it as

$$\partial_t \begin{pmatrix} \sigma^* \\ u_P \\ v_P \end{pmatrix} + a_P \begin{bmatrix} 0 & \partial_x & \partial_y \\ \partial_x & 0 & 0 \\ \partial_y & 0 & 0 \end{bmatrix} \begin{pmatrix} \sigma^* \\ u_P \\ v_P \end{pmatrix} = \mathbf{0} \tag{4.34}$$

Similarly, by introducing new variables ω^* and v_S^* defined as

$$\omega = a_S\omega^* \tag{4.35}$$

$$v_S = -v_S^* \tag{4.36}$$

We can rewrite Equation 4.29 as

$$\partial_t \begin{pmatrix} \omega^* \\ v_S^* \\ u_S \end{pmatrix} + a_S \begin{bmatrix} 0 & \partial_x & \partial_y \\ \partial_x & 0 & 0 \\ \partial_y & 0 & 0 \end{bmatrix} \begin{pmatrix} \omega^* \\ v_S^* \\ u_S \end{pmatrix} = \mathbf{0} \tag{4.37}$$

Equations 4.34 and 4.37 correspond to the familiar linear acoustics equations presented in Equation 3.14. In fact, these equations represent the splitting of an elastodynamic equation into two acoustic equations, each with its respective wave speed, namely, a_P and a_S. In this context, these equations are entirely decoupled, except at the boundaries, where the homogeneity of the system is lost. In boundary elements, both $\nabla \times \boldsymbol{u}_P$ and $\nabla \cdot \boldsymbol{u}_S$ are non-zero.

We employ the Hermite Active Flux method, as explained in Section 3.3.2, to solve both the P- and S- wave acoustic equations. This choice allows us to apply boundary conditions remotely without needing to handle the coupling of stresses at the boundaries, as demonstrated by Nakazawa [82]. Additionally, the Hermite method promptly provides us with the velocity gradients, enabling us to compute stress rates with the degree of freedom of the elements, as these gradients are directly related to the stress rates. In this context, we utilize Equations 4.18 through 4.21 instead of relying on the computationally expensive calculations in Equation 4.30.

4.3 Example Cases

In this section, we showcase numerical experiments aimed at illustrating the method's characteristics. We commence with wave interactions within a homogeneous material, proceed to waves traveling two distinct materials, and conclude with a test case where waves interact while traveling along the interface of two dissimilar materials.

The domain is rectangular with an aspect ratio of 1/2 and open boundaries. There are two available mesh options: a grid consisting of 60×30 squares, each subdivided by common diagonals, resulting in right triangles as the constituent elements of the grid, and an unstructured grid formed by using equilateral triangles. These mesh choices allow us to assess the numerical solver's performance under different element orientations concerning wave propagation. Both mesh configurations are illustrated in Figure 4.1. In all scenarios, we employ the fourth-order Hermite element ($p = 4$) presented in Figure 2.6b. Furthermore, we introduce a Gaussian pulse centered at (x_0, y_0) described by

$$g(\boldsymbol{x})_{(x_0,y_0)} = \exp\left(\frac{(x-x_0)^2 + (y-y_0)^2}{2\delta^2}\right) \tag{4.38}$$

This Gaussian pulse has a variance of $\delta = 0.1$ and is utilized to apply loading within the domain.

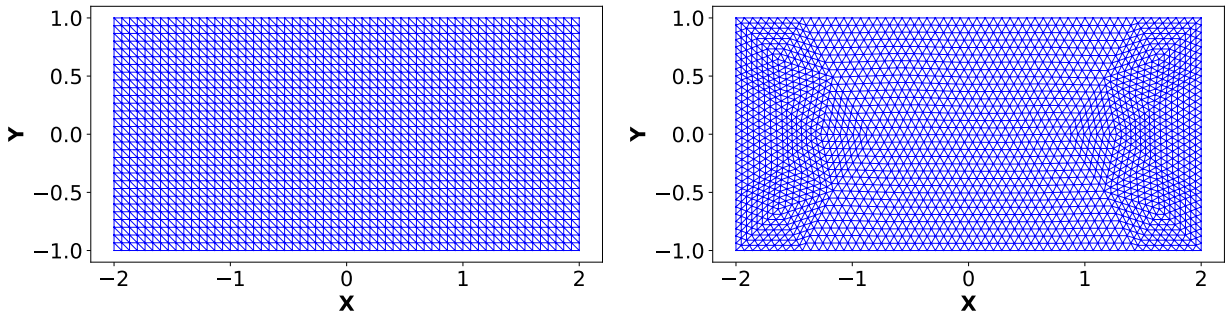

Figure 4.1: Structured (left) and unstructured (right) mesh configurations.

4.3.1 Wave Interaction

In the beginning, we examine wave interactions within a homogeneous material using the unstructured mesh depicted in Figure 4.1 (right grid). This material is defined by Lamé parameters as

$$\lambda = \mu = 1 \tag{4.39}$$

We define the initial loading using a Gaussian pulse described by Equation 4.38 applied at two distinct locations near the left and right ends of the domain.

$$\sigma^*(0, \boldsymbol{x}) = \omega^*(0, \boldsymbol{x}) = 1 + \frac{1}{4}\left(g(\boldsymbol{x})_{(-1,0)} + g(\boldsymbol{x})_{(1,0)}\right) \tag{4.40}$$

$$u_P(0, \boldsymbol{x}) = u_S(0, \boldsymbol{x}) = 0 \tag{4.41}$$

$$v_P(0, \boldsymbol{x}) = v_S^*(0, \boldsymbol{x}) = 0 \tag{4.42}$$

This initial condition generates both types of waves at the center of each subdomain. The results are presented in Figures 4.2, 4.3, 4.4, and 4.5.

Figure 4.2 illustrates the behavior of P-waves (σ) in the left-hand and S-waves (ω) in the right-hand contour plots over time. Initially (first row from top), these waves have different amplitudes due to distinct wave speeds: $a_P = 1.7$ for P-waves and $a_S = 1.0$ for S-waves.

Around $t = 0.45$ (second row from top), the P-waves reach each other at the line $(x = 0, y)$ and the open boundaries while the S-waves are approximately three-fifths of the way out of the domain. This is because S-waves travel at about 60% of the speed of P-waves.

At $t = 0.65$ (third row from top), the P-waves (left hand contour plot) collide in the center, leading to an interaction that amplifies them in that region while causing cancellation effects at the sides. The interactions between the velocity components and rates of stress are depicted in Figures 4.3 and 4.4, respectively. Because of the symmetric nature of the problem, this behavior is symmetrical around the line $(x, y = 0)$. It's worth noting that we

compute rates of stress using gradient updates from the Hermite AF method, where gradient information becomes immediately available during the reconstruction stage.

The interaction of S-waves occurs around $t = 1.25$ (fourth row from top), at which point the original P-waves have largely left the domain, but the waves arising from the collision remain and are about halfway out. Note that they are still P-waves, and therefore invisible in the right-hand contour plot.

Figure 4.5 provides an intriguing observation. As the P-waves exit the open boundaries (as evident in the second and third rows of the left contours), it becomes apparent that $\boldsymbol{u}_P$ does not exhibit irrotational behavior. Additionally, when the S-waves cross the open boundaries (as seen in the third and fourth rows of the right contours), $\boldsymbol{u}_S$ does not adhere to divergence-free characteristics. However, the magnitudes of these disturbances are extremely small. This phenomenon arises because of the differing wave speeds imposed by the open boundaries, where the wave speed of the material outside is, in effect, set to zero.

Specifically, at $t = 1.25$, as the P-wave exits the domain (fourth row from top of the left contours in Figure 4.2) around $x \approx 1.0$ and -1.0, $\nabla \times \boldsymbol{u}_P$ exhibits a non-zero value (third row from top of the left contours in Figure 4.5). Similarly, $\nabla \cdot \boldsymbol{u}_S$ also has a non-zero value (third row from top of the right contours in Figure 4.5) since the S-waves are leaving the domain while interacting along the center line $(x = 0, y)$ (fourth row from top of the right contours in Figure 4.2).

Additionally, at $t = 1.25$, there is a generation of a small-amplitude wave resulting from the interaction that takes place behind the P-waves (fourth row from top of the left contours in Figure 4.2). This phenomenon is also evident in the velocity components and the rate of stresses, as depicted in Figures 4.3 and 4.4, respectively. The faint crosses visible in the center of the departing P-waves (also visible at the next level in the departing S-waves) are the faint reflections of the original waves from the upper and lower boundaries. They are of very low amplitude, $\approx 0.1\%$ of the outgoing waves. Recall [78] that there is no local boundary condition that enforces perfectly non-reflecting behavior[4].

Finally, By $t = 2.0$, S-waves are still propagating through the domain, while the P-waves have left it (fifth row from top of the left and right contours, respectively, in Figure 4.2). There are still small-amplitude waves within the P-waves subsystem, primarily due to interactions and boundary effects. Note the scale of the data.

[4]For a recent, very comprehensive, review from the standpoint of elastic waves, see [80].

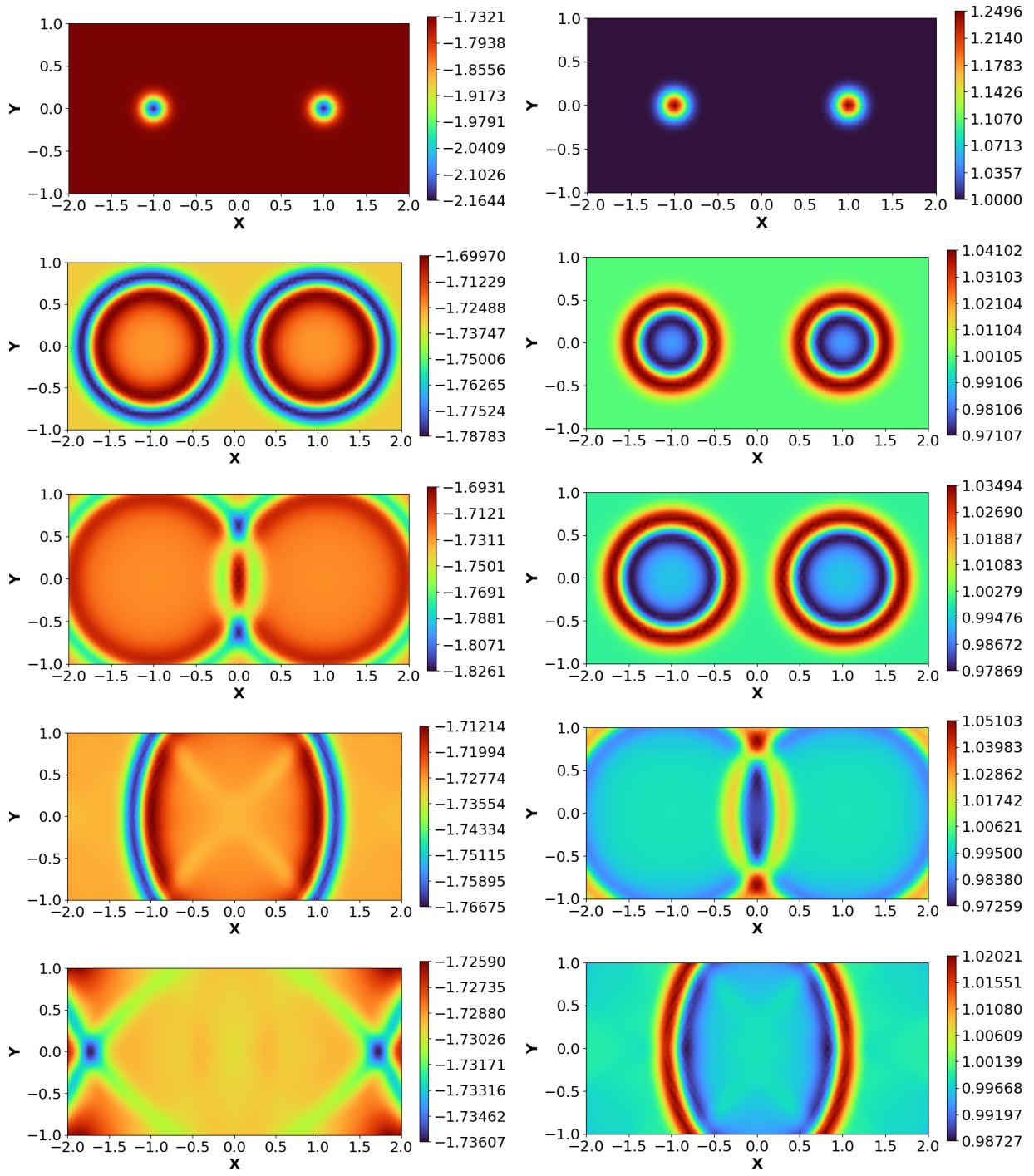

Figure 4.2: Temporal evolution of σ (left) and ω (right) during the propagation of an elastic wave under a dual-load condition; from top to bottom: $t = 0.0, 0.45, 0.65, 1.25, 2.0$.

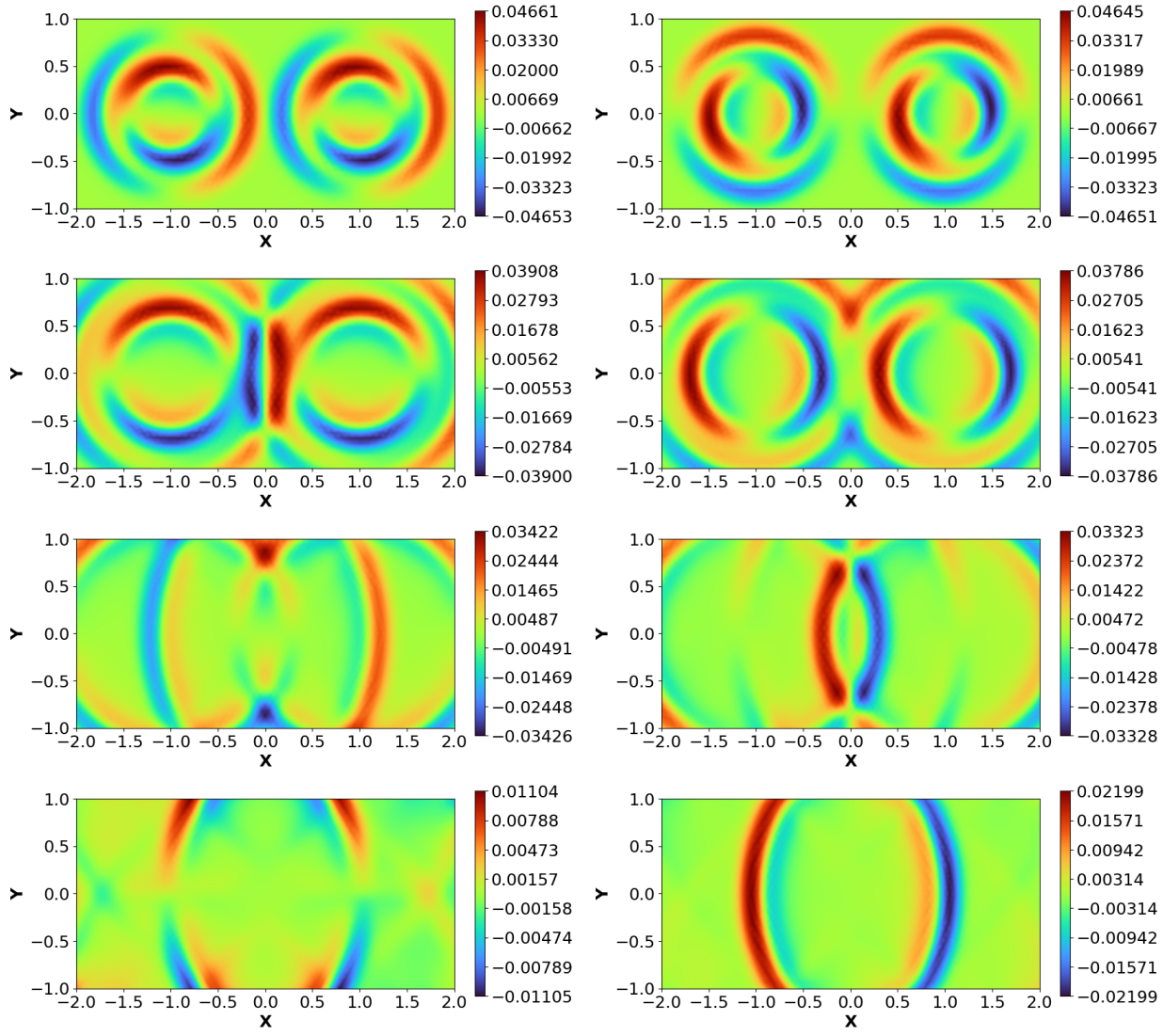

Figure 4.3: Temporal evolution of u (left) and v (right) during the propagation of an elastic wave under a dual-load condition; from top to bottom: $t = 0.45, 0.65, 1.25, 2.0$.

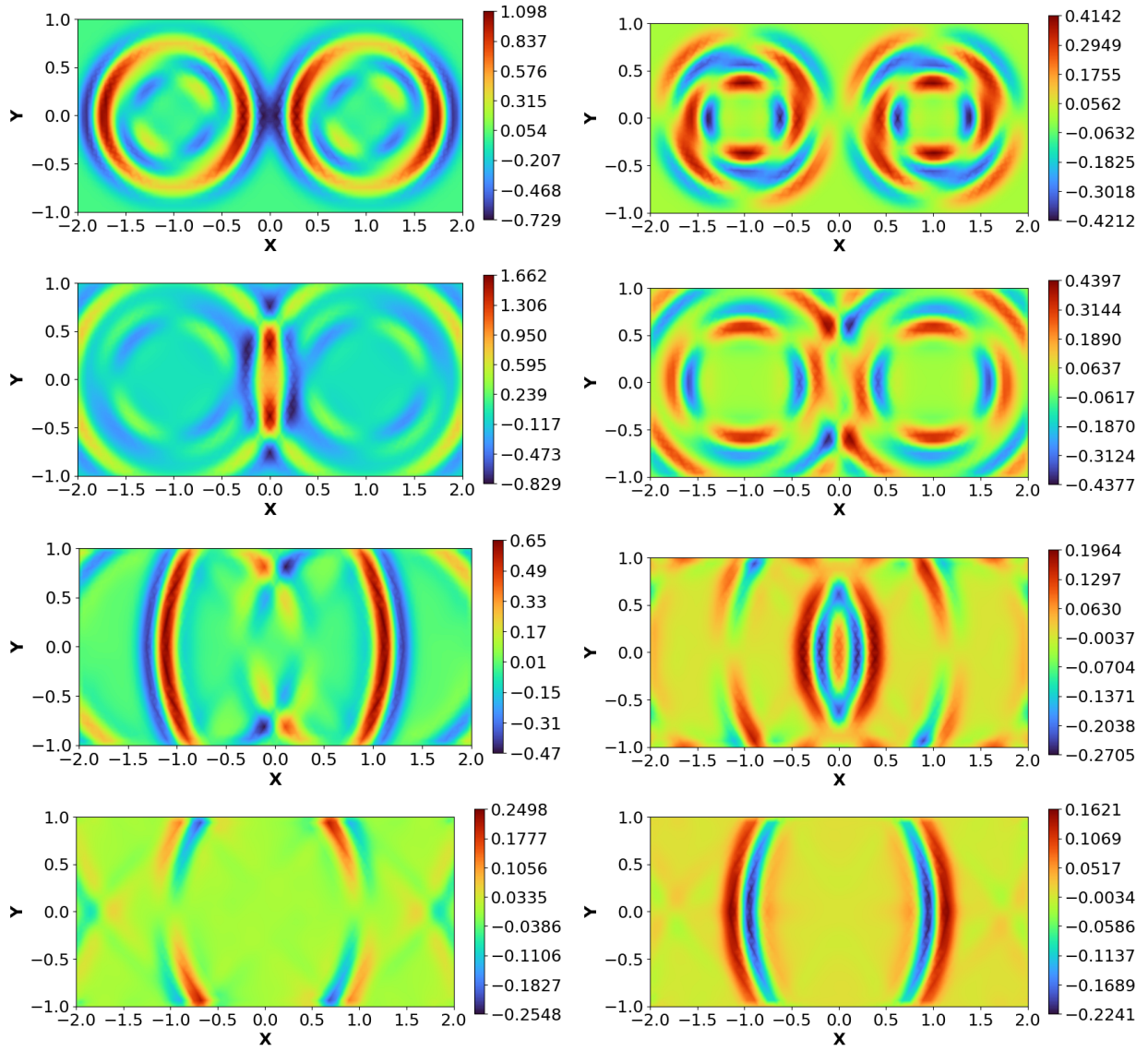

Figure 4.4: Temporal evolution of $\dot{\sigma}_{xx}$ (left) and $\dot{\sigma}_{xy}$ (right) during the propagation of an elastic wave under a dual-load condition; from top to bottom: $t = 0.45, 0.65, 1.25, 2.0$. The behavior of $\dot{\sigma}_{yy}$ closely resembles that of $\dot{\sigma}_{xx}$ but is oriented normal to the direction of $\dot{\sigma}_{xx}$ due to symmetry.

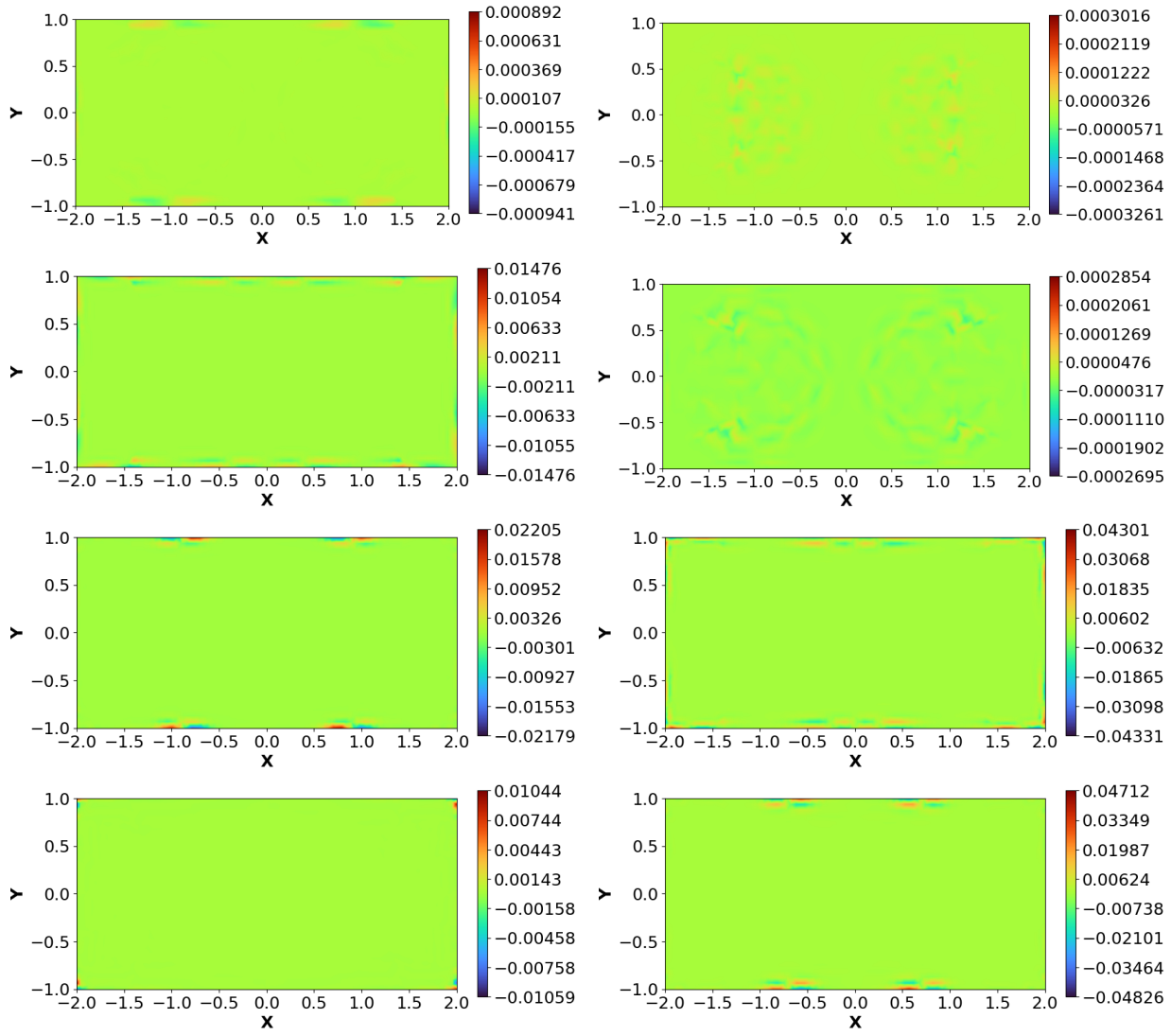

Figure 4.5: Temporal evolution of $\nabla \times \boldsymbol{u}_P$ (left) and $\nabla \cdot \boldsymbol{u}_S$ (right) during the propagation of an elastic wave under a dual-load condition; from top to bottom: $t = 0.45, 0.65, 1.25, 2.0$.

4.3.2 Wave Propagation through Multiple Materials

In Section 4.3.1, we observed that when waves exit the boundaries, vortices and divergence are generated due to the non-constant material properties across the boundaries. To shed further light on this phenomenon, we set up a problem where the boundary exists within the domain, creating an interface through which waves propagate in different materials. In this scenario, employing the structured mesh in Figure 4.1 (left grid), we establish an interface along the line $(x = 0, y)$, where the left and right sides have different material properties given by

$$\text{Left: } \begin{cases} \lambda = 1 \\ \mu = 1 \end{cases} \qquad \text{Right: } \begin{cases} \lambda = 1 \\ \mu = 2 \end{cases} \tag{4.43}$$

To isolate the effects of the material interface, we exclusively apply loading to the left side, defined as

$$\sigma^*(0, \boldsymbol{x}) = \omega^*(0, \boldsymbol{x}) = 1 + \frac{1}{4} g(\boldsymbol{x})_{(-1,0)} \tag{4.44}$$

$$u_P(0, \boldsymbol{x}) = u_S(0, \boldsymbol{x}) = 0 \tag{4.45}$$

$$v_P(0, \boldsymbol{x}) = v_S^*(0, \boldsymbol{x}) = 0 \tag{4.46}$$

The results are exhibited in Figures 4.6, 4.7, 4.8, and 4.9.

Figure 4.6 presents the evolution of P-waves (σ) and S-waves (ω) over time. At the initial time (first row), the distinct materials on each side lead to higher values of P-waves on the left side of the domain and higher values of S-waves on the right side of the domain.

Around $t = 0.4$ (second row from top), the P-wave reaches the interface (left contour plot), while the S-wave (right contour plot) continues to propagate through the left material without any boundary interaction. The P-wave interface interaction leads to a slight generation of vorticity (first row of the left contour plots of Figure 4.9). This phenomenon occurs because the P-wave system is responsible for generating vorticity. During this time, the S-wave shows no interaction resulting in zero divergence (first row of the right contour plots of Figure 4.9).

By the time $t = 0.6$ (third row from top), the P-wave (left contour plot) has crossed the interface and entered the right material, where the wave speed (a_P) is higher. This leads to an acceleration of the wave front. This phenomenon is also apparent in the velocity components and the rate of stresses, as illustrated in Figures 4.7 and 4.8, respectively. Notably, there are no reflections observed during this time as the wave crosses the right material perpendicularly. Observing Figure 4.9, it's apparent that the amplitude of vorticity increases as the P-wave passes through at $t = 0.6$ (second row). However, this generated vorticity will gradually decay and exit the domain as the wave continues to pass through the interface.

At around $t = 0.75$ (fourth row from top), the P-wave (left contour plot) is exiting the left-side material while it propagates at a different speed through the right-side material. There are no visible reflections due to the open boundaries and the interface. During this time, the S-wave (right contour plot) reaches the interface and begins to interact within the material regions with different properties. This is when we start to observe the generation of divergence (third row of the right contour plots of Figure 4.9).

At $t = 2.0$ (fifth row from top), the P-wave (left contour plot) has left the domain, and the vorticity within the domain has become minimal (fourth row of the left contour plots of Figure 4.9). However, the S-wave (right contour plot) is still traveling and is located approximately at $x = 1.0$ (fourth row of the right contour plots of Figure 4.9). Here, near the open boundary, we observe the presence of divergence, indicating the open boundary effects as the S-wave continues to propagate.

4.3.3 Wave Interaction through Multiple Materials

To comprehensively investigate the effect of wave interaction at material interfaces, we combine the problems discussed in Sections 4.3.1 and 4.3.2. Once again, utilizing the structured mesh in Figure 4.1 (left grid), we divide the domain into two materials

$$\text{Left: } \begin{cases} \lambda = 1 \\ \mu = 1 \end{cases} \qquad \text{Right: } \begin{cases} \lambda = 1 \\ \mu = 2 \end{cases} \tag{4.47}$$

We apply loading near both ends, on the left and right sides, using

$$\sigma^*(0, \boldsymbol{x}) = \omega^*(0, \boldsymbol{x}) = 1 + \frac{1}{4}\left(g(\boldsymbol{x})_{(-1,0)} + g(\boldsymbol{x})_{(1,0)}\right) \tag{4.48}$$

$$u_P(0, \boldsymbol{x}) = u_S(0, \boldsymbol{x}) = 0 \tag{4.49}$$

$$v_P(0, \boldsymbol{x}) = v_S^*(0, \boldsymbol{x}) = 0 \tag{4.50}$$

This setup allows us to thoroughly explore the consequences of wave interaction at material interfaces, considering varying material properties on both sides of the interface and applying loading conditions at multiple locations within the domain. The results are depicted in Figures 4.10, 4.11, 4.12, and 4.13.

Figure 4.10 illustrates the evolution of P-waves (left contour plots) and S-waves (right contour plots) as they propagate through two distinct materials. Notably, each wave system interacts with waves of the same type at the interface between these materials, revealing complex wave behavior and interactions.

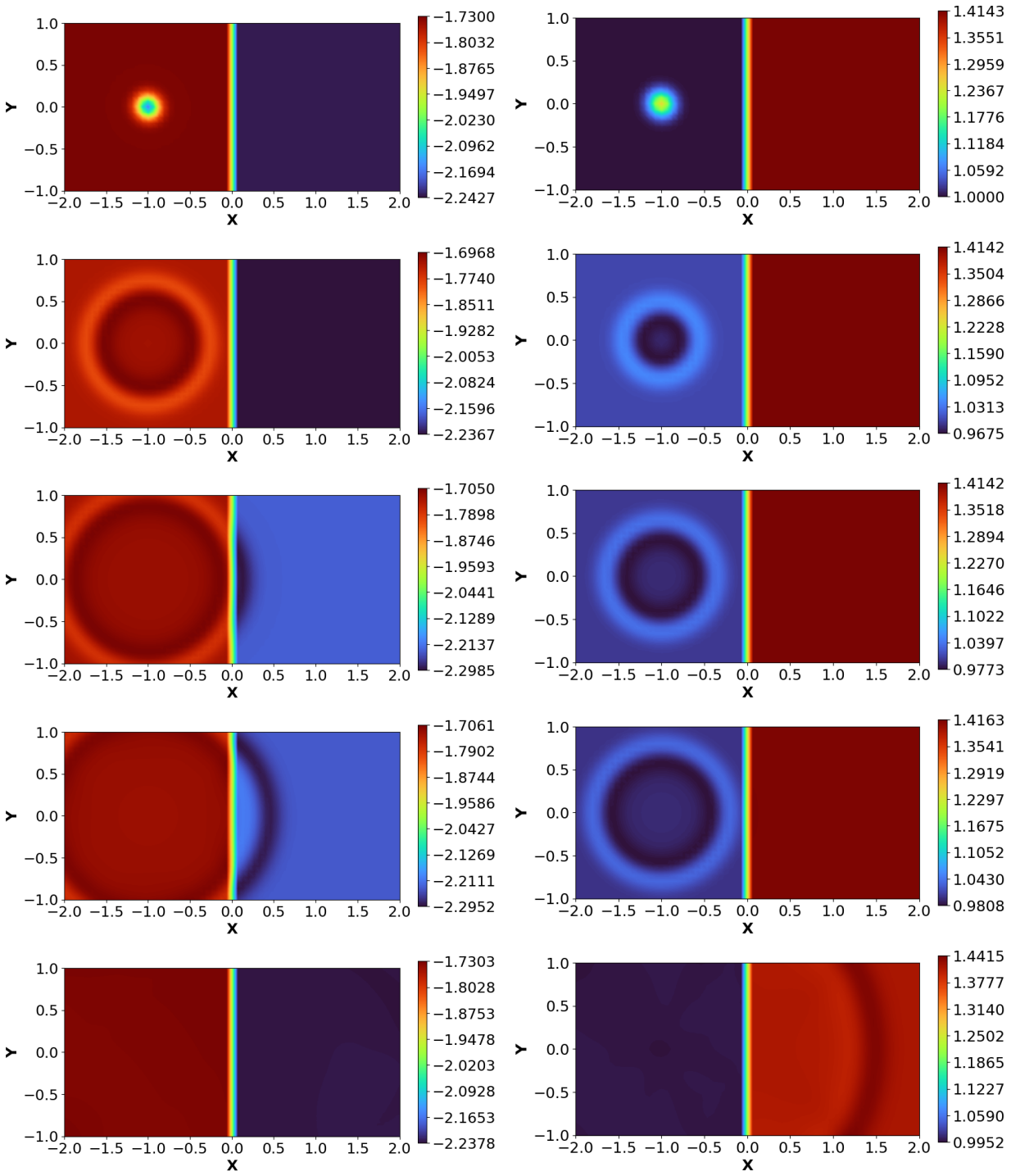

Figure 4.6: Temporal evolution of σ (left) and ω (right) during the propagation of an elastic wave through two different materials under a single-load condition; from top to bottom: $t = 0.0, 0.4, 0.6, 0.75, 2.0$.

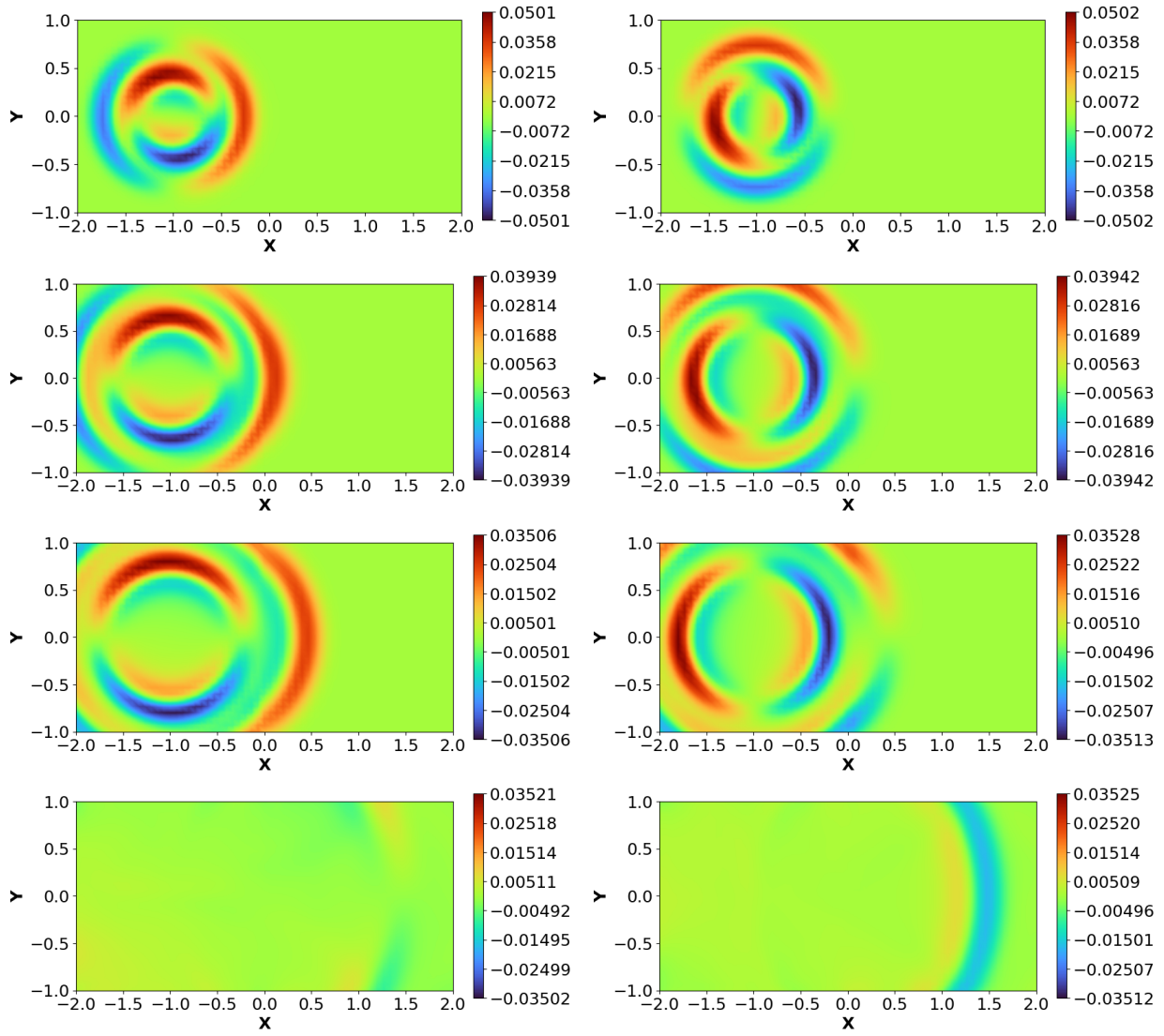

Figure 4.7: Temporal evolution of u (left) and v (right) during the propagation of an elastic wave through two different materials under a single-load condition; from top to bottom: $t = 0.4, 0.6, 0.75, 2.0$.

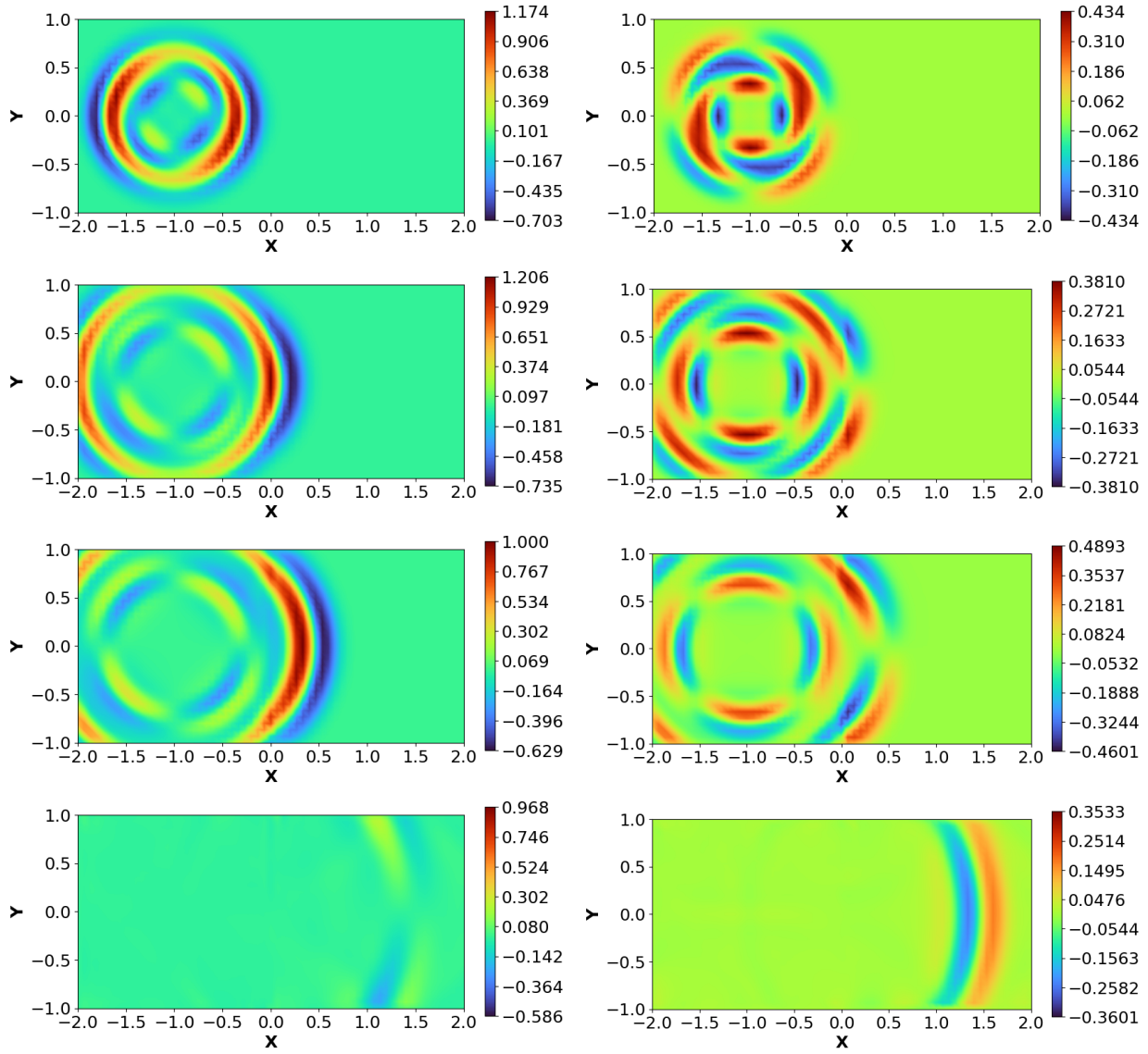

Figure 4.8: Temporal evolution of $\dot{\sigma}_{xx}$ (left) and $\dot{\sigma}_{xy}$ (right) during the propagation of an elastic wave through two different materials under a single-load condition; from top to bottom: $t = 0.4, 0.6, 0.75, 2.0$. The behavior of $\dot{\sigma}_{yy}$ closely resembles that of $\dot{\sigma}_{xx}$ but is oriented normal to the direction of $\dot{\sigma}_{xx}$ due to symmetry.

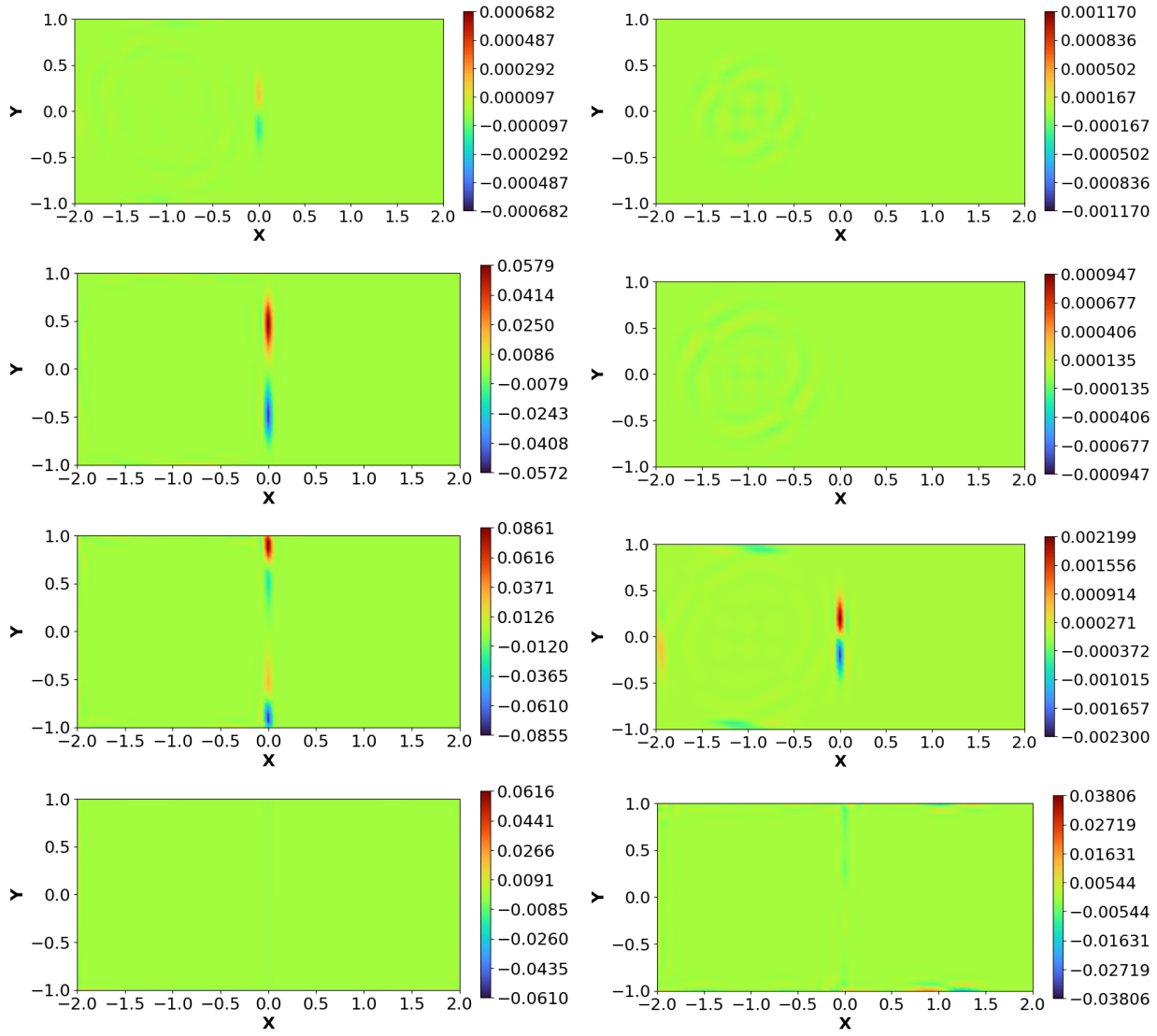

Figure 4.9: Temporal evolution of $\nabla \times \boldsymbol{u}_P$ (left) and $\nabla \cdot \boldsymbol{u}_S$ (right) during the propagation of an elastic wave through two different materials under a single-load condition; from top to bottom: $t = 0.4, 0.6, 0.75, 2.0$.

In this scenario, the wave propagation within each subsystem exhibits characteristics reminiscent of what we discussed in Sections 4.3.1 and 4.3.2. However, the presence of material variations at the interface introduces an element of asymmetry into the wave interaction around the line $(x = 0, y)$.

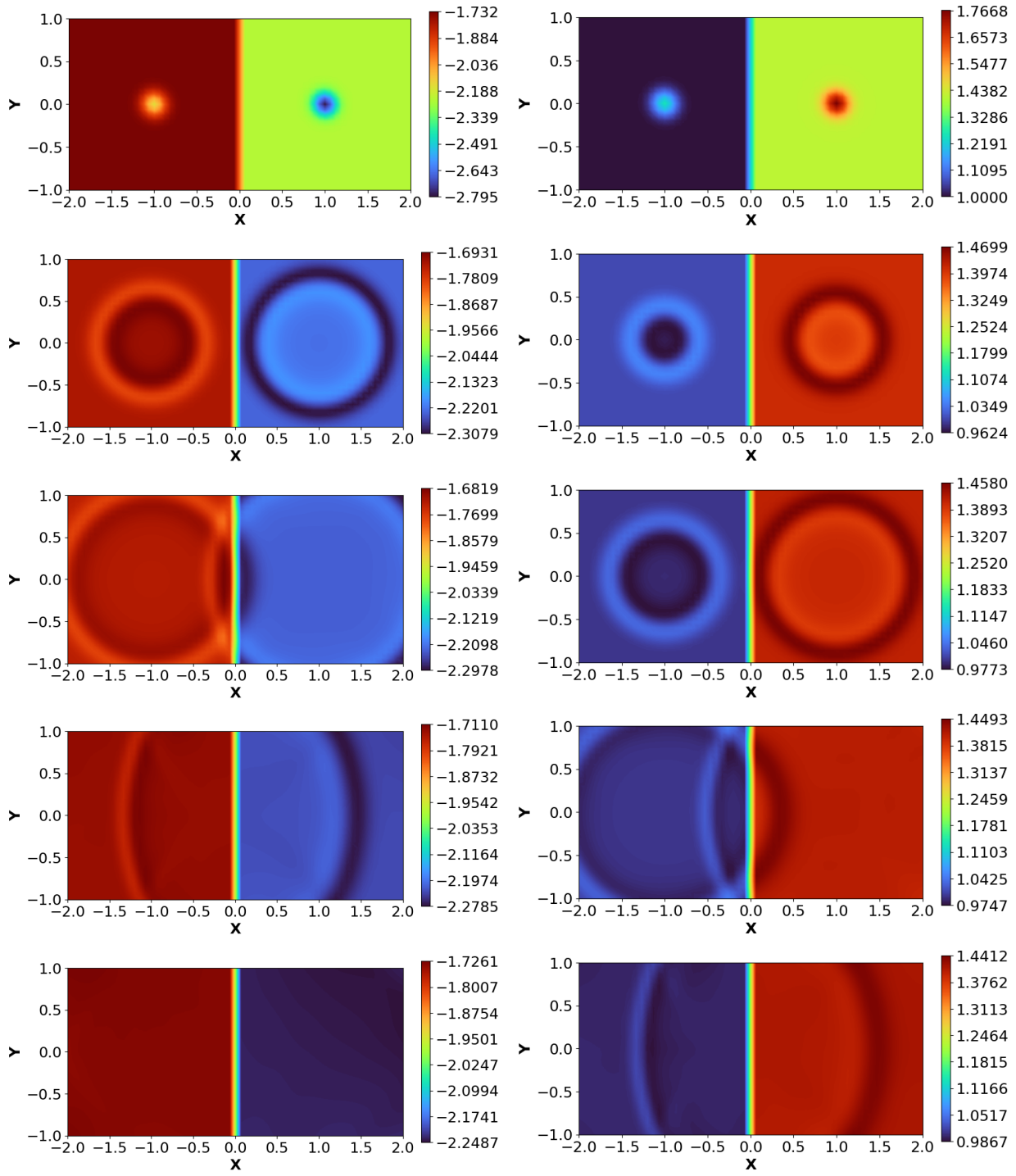

Figure 4.10: Temporal evolution of σ (left) and ω (right) during the propagation of elastic waves through two different materials under a dual-load condition; from top to bottom: $t = 0.0, 0.35, 0.6, 1.2, 2.0$.

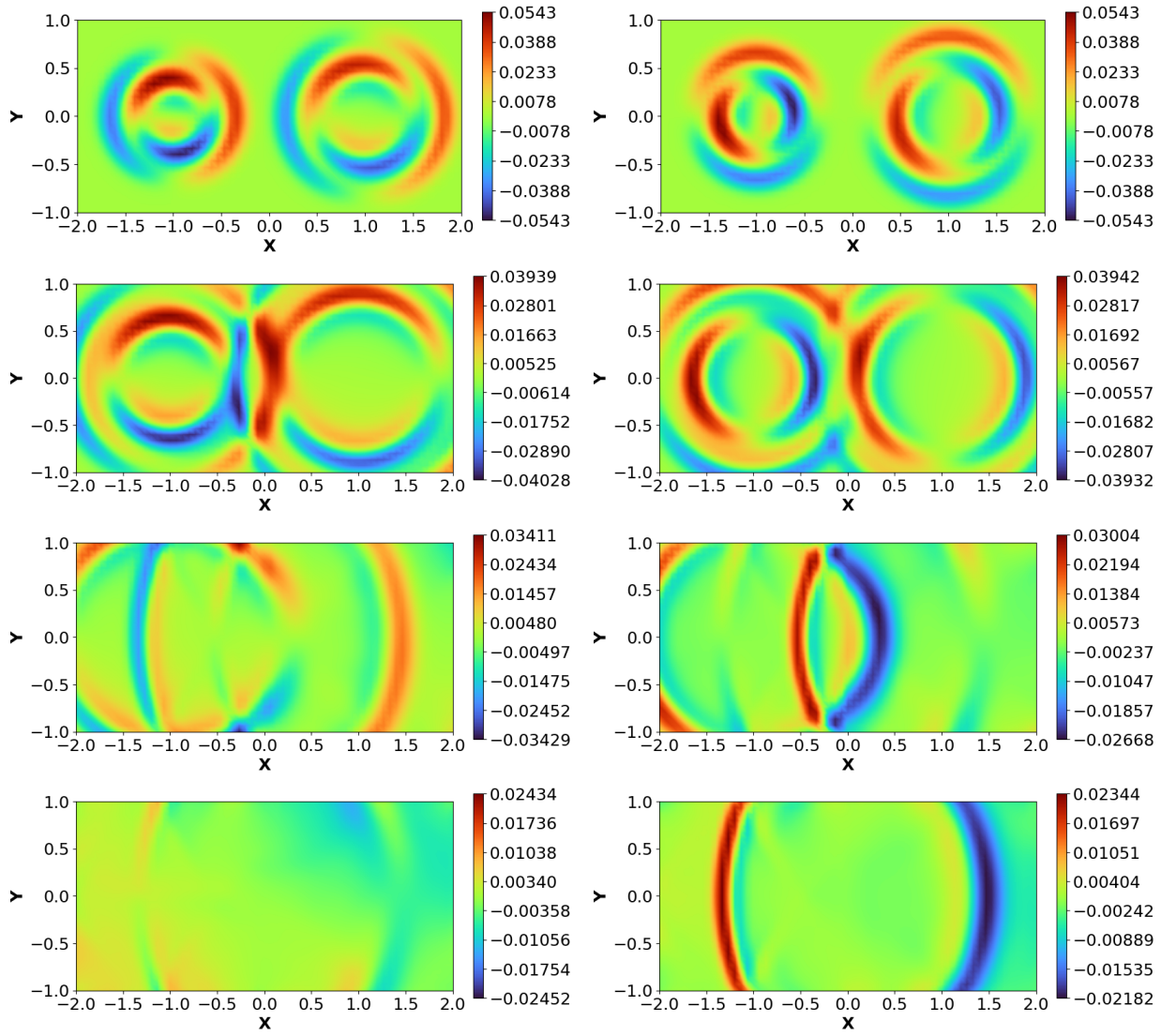

Figure 4.11: Temporal evolution of u (left) and v (right) during the propagation of elastic waves through two different materials under a dual-load condition; from top to bottom: $t = 0.35, 0.6, 1.2, 2.0$.

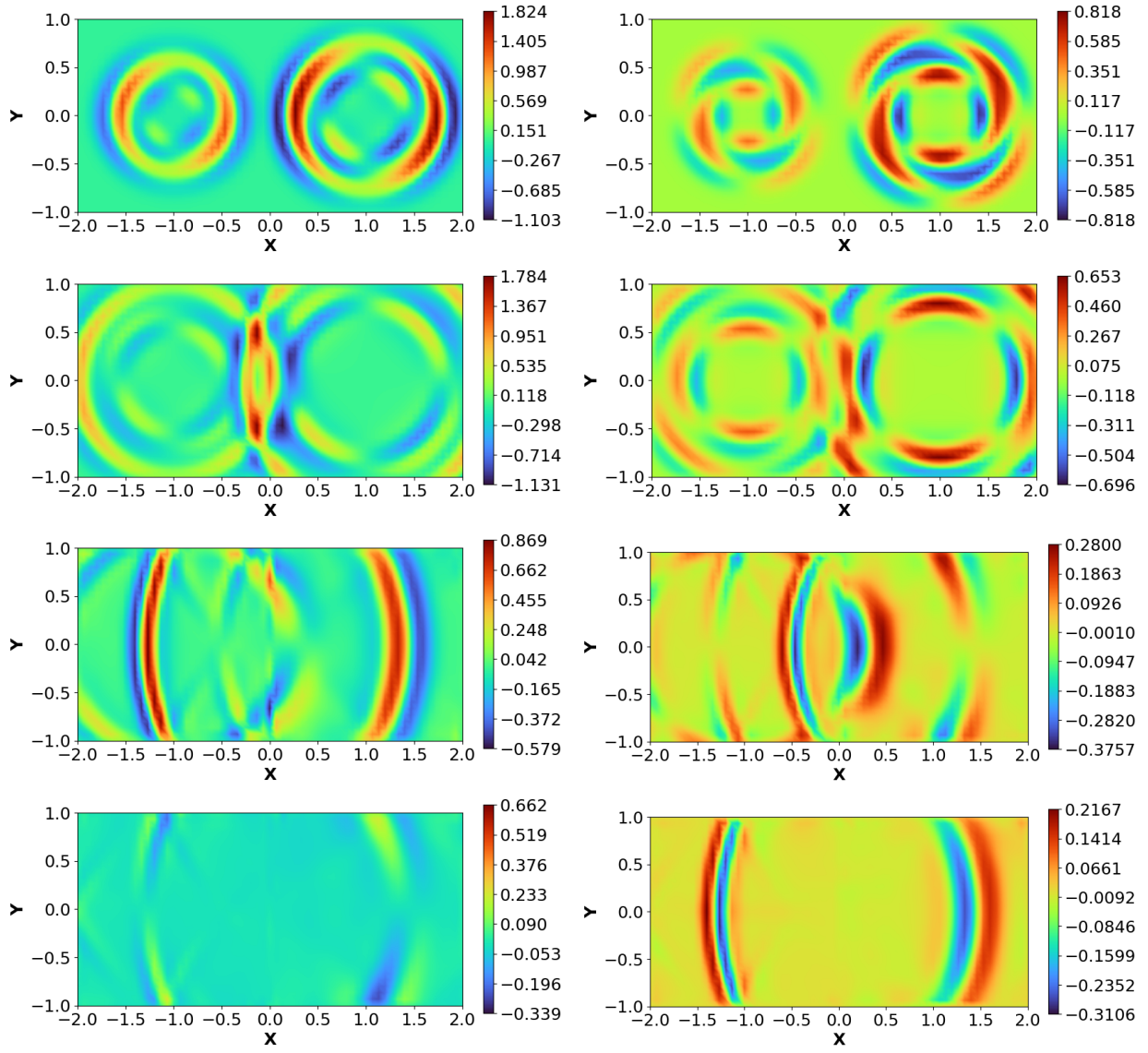

Figure 4.12: Temporal evolution of $\dot{\sigma}_{xx}$ (left) and $\dot{\sigma}_{xy}$ (right) during the propagation of elastic waves through two different materials under a dual-load condition; from top to bottom: $t = 0.35, 0.6, 1.2, 2.0$. The behavior of $\dot{\sigma}_{yy}$ closely resembles that of $\dot{\sigma}_{xx}$ but is oriented normal to the direction of $\dot{\sigma}_{xx}$ due to symmetry.

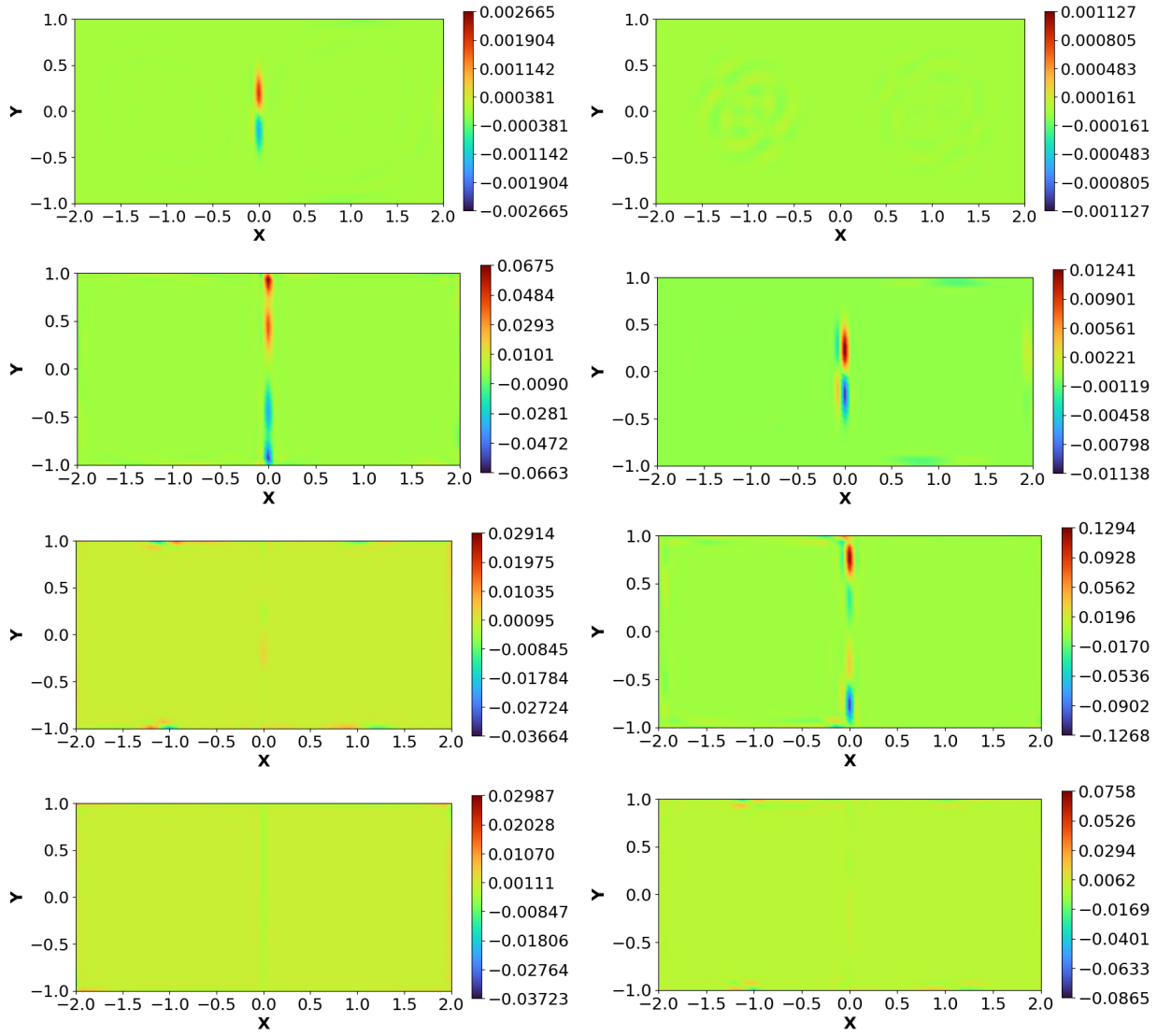

Figure 4.13: Temporal evolution of $\nabla \times \boldsymbol{u}_P$ (left) and $\nabla \cdot \boldsymbol{u}_S$ (right) during the propagation of elastic waves through two different materials under a dual-load condition; from top to bottom: $t = 0.35, 0.6, 1.2, 2.0$.

CHAPTER 5

Towards the Future: Concluding Insights and Next Steps

5.1 Conclusive Remarks

This dissertation details an effective strategy, known as the Hermite Active Flux method for tackling wave propagation problems when dealing with coarse grids. Currently, this approach is primarily applied within the context of multimaterial wave propagation, where linear equations with non-constant coefficients govern the behavior of waves.

A foundational concept explored in Chapter 2 is the "element" and its extension into arbitrary dimensions. This concept, coupled with the remarkable flexibility of reconstructing the element to attain any desired order, is crucial in addressing problems involving irregular geometries or complex domains. The chapter delves into the construction of an unstructured grid, wherein an arbitrary order element is placed in any desired dimension. Specifically, two-dimensional elements with 6 (quadratic) and 15 (quartic) degrees of freedom are discussed, highlighting various types of degrees of freedom. Hermite elements, which utilize gradients as degrees of freedom, demonstrate lower sensitivity to perturbations in reconstruction. This exploration sets the stage for a three-dimensional space discussion, introducing Hermite elements defined with 10 degrees of freedom for quadratic elements and 35 degrees of freedom for quartic elements in three-dimensional space.

Building upon the principles outlined in Chapter 2, Chapter 3 presents an alternative to Riemann solvers, which inherently assume wave propagation solely along element interfaces, thereby emphasizing one-dimensional wave behavior. Instead, our strategy relies on a representation derived from spherical means, which remains valid in three dimensions. We harness the potential of C^1 Hermitian elements, ensuring the absence of nonphysical discontinuities and enabling the use of larger time steps. Our fully discrete time-stepping approach maintains a compact domain of dependence, allowing us to clearly visualize flow features, even when they are only coarsely resolved. Additionally, it significantly reduces the need

for interface boundary conditions. Implementation is facilitated through an element-wise traversal that is applicable to any boundary with minimal adjustments.

In Chapter 4, the study focuses on elastodynamic waves, which are effectively decoupled into two distinct systems: P-waves and S-waves. Interestingly, both systems exhibit behavior akin to acoustic waves. The coupling between these systems exclusively takes place at boundaries where the two interact. The Hermite Active Flux method, introduced in Chapter 3, is applied to independently solve each system. This method facilitates the computation of stress rates through the gradient update of the Hermite element, introducing no additional computational burden.

5.2 Roadmap for Future Research

There are several promising avenues for extending this research effort. These potential extensions encompass the following areas.

- **Maxwell's Equations:** The behavior of these equations is akin to what was demonstrated in Chapter 4, where a pair of isotropic waves propagate with a constant wavespeed—one for the electric field and another for the magnetic field.

- **Exploring Different Boundary Conditions:** In Chapter 4, we delved into the propagation of elastic waves using the built-in open boundary condition implementation of AF. However, there are more intriguing boundary conditions to consider, such as free boundaries and rigid boundaries. In these scenarios, the P- and S-wave systems become coupled, resulting in interactions between waves of different types. Investigating the implementation of these boundary conditions within the context of AF represents a compelling avenue for future research.

- **Family of Multidimensional Methods:** Indeed, introducing higher-order methods in multiple dimensions presents challenges, particularly when it comes to symmetrically distributing degrees of freedom within each element. For example, to create a fifth-order method in three dimensions, each element would require 35 degrees of freedom to define a sextic function. This could be achieved by having one value and three derivatives at each vertex, along with one value and two derivatives at each edge midpoint. This distribution results in a total of $4 \times 4 + 6 \times 3 = 34$ degrees of freedom. Including the element average would complete the set and create a conservative method. Alternatively, consider seeking a seventh-order method in two dimensions, which necessitates 28 degrees of freedom. At each vertex of a tetrahedral element, you

might have one value, two first derivatives, and three second derivatives. At each edge midpoint, you could have one value, along with the first and second derivatives along the median, totaling $3 \times 6 + 3 \times 3 = 27$ degrees of freedom. Again, the addition of a element average would fulfill the requirement for conservation. However, it's worth noting that not every attempt at extension will result in such neat solutions.

- **Three-dimensional AF:** Utilizing spherical means integral to solve wave propagation problems offers the advantage of maintaining physical validity when extended to three dimensions. However, the challenge in this extension lies in the computation of the spherical means integral, as defined by Equation 3.23, over the sphere of influence. In three dimensions, this equation can be expressed using a spherical coordinate system as

$$M_R\{f\}(x_0, y_0, z_0) = \frac{1}{4\pi R^2} \int_{\phi_P}^{\phi_Q} \int_{\theta_P}^{\theta_Q} f(x_0 + R\sin\phi\cos\theta, y_0 + R\sin\phi\sin\theta, z_0 + R\cos\phi) R^2 \sin\phi \, d\theta \, d\phi \tag{5.1}$$

In Equation 5.1, we define the element's contribution to computing the average of reconstructed solution, over a partial sphere surrounded by the element. This includes the partial spheres centered at each vertex or edge node, as illustrated in Figure 5.1. These partial spheres will ultimately add up to a full sphere when taking the spherical means of neighboring elements centered at shared nodes.

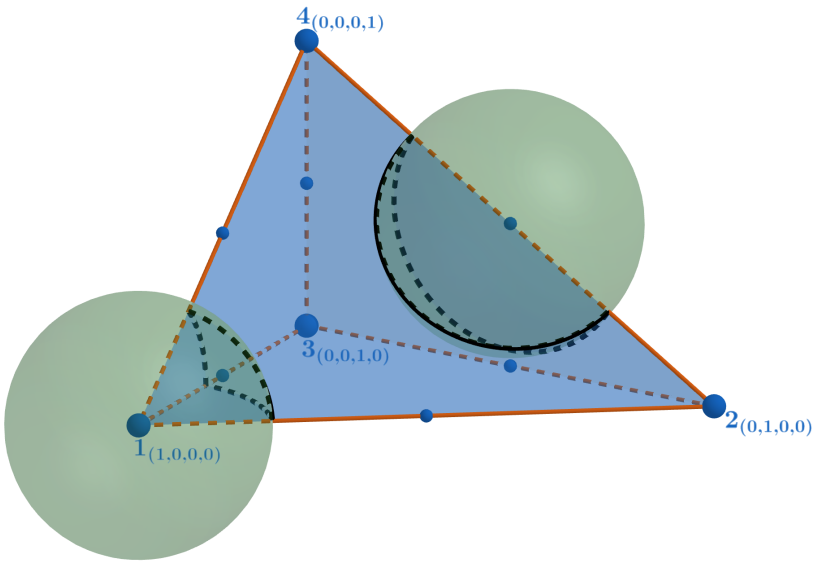

Figure 5.1: Partial spheres for spherical means computation in three dimensions.

Similar to the details expanded in Appendix B for two dimensions, we can show that

when using the basis functions for element reconstructions proposed in Table 2.6, in three dimensions, the integrals to be computed all take the form

$$I_{(p_1,p_2,p_3)} = \int_{\phi_P}^{\phi_Q} \int_{\theta_P}^{\theta_Q} (\sin\phi\cos\theta)^{p_1} (\sin\phi\sin\theta)^{p_2} (\cos\phi)^{p_3} \sin\phi \, d\theta \, d\phi \tag{5.2}$$

where $0 \leq p_1 + p_2 + p_3 \leq p$. Equation 5.2 has a closed-form solution, which takes the form:

$$I_{(p_1,p_2,p_3)} = I^{\phi}_{(p_1,p_2,p_3)} I^{\theta}_{(p_1,p_2,p_3)} \tag{5.3}$$

where $I^{\phi}_{(p_1,p_2,p_3)}$ and $I^{\theta}_{(p_1,p_2,p_3)}$ are computed by

$$I^{\phi}_{(p_1,p_2,p_3)} = a^{\phi}_0 \Delta_1(\phi_{PQ}) + \sum_{i=1}^{p_1+p_2+p_3+1} a^{\phi}_i \Delta_{\cos}(i\phi_{PQ}) + b^{\phi}_i \Delta_{\sin}(i\phi_{PQ}) \tag{5.4}$$

$$I^{\theta}_{(p_1,p_2,p_3)} = a^{\theta}_0 \Delta_1(\theta_{PQ}) + \sum_{i=1}^{p_1+p_2+p_3} a^{\theta}_i \Delta_{\cos}(i\theta_{PQ}) + b^{\theta}_i \Delta_{\sin}(i\theta_{PQ}) \tag{5.5}$$

Here, $\Delta_f(i\phi_{PQ})$ is defined as:

$$\Delta_f(i\phi_{PQ}) \equiv f(i\phi_Q) - f(i\phi_P) \tag{5.6}$$

The closed-form solutions to Equation 5.2 should be computed up to the required order of reconstruction p. Here are the solutions for $p = 1$

$$I_{(0,0,0)} = -(\cos\phi_Q - \cos\phi_P)(\theta_Q - \theta_P) \tag{5.7}$$

$$I_{(1,0,0)} = \frac{1}{4}[2(\phi_Q - \phi_P) - (\sin 2\phi_Q - \sin 2\phi_P)][\sin(\theta_Q) - \sin(\theta_P)] \tag{5.8}$$

$$I_{(0,1,0)} = -\frac{1}{4}[2(\phi_Q - \phi_P) - (\sin 2\phi_Q - \sin 2\phi_P)][\cos(\theta_Q) - \cos(\theta_P)] \tag{5.9}$$

$$I_{(0,0,1)} = -\frac{1}{4}(\cos 2\phi_Q - \cos 2\phi_P)(\theta_Q - \theta_P) \tag{5.10}$$

These integrals constitute the fundamental building blocks of spherical means integrals in three-dimensional space, which may find application in future three-dimensional Active Flux methods.

APPENDIX A

Element Reconstruction

Let $\mathbf{\Omega}$ represent an m-dimensional element in n-dimensional space ($n \geq m$) described by a barycentric coordinate system $\boldsymbol{\sigma} = (\sigma_1, \sigma_2, .., \sigma_{m+1})$. Ensuring proper normalization of coordinates is crucial to establish unique coordinates for each point within the element, and it is achieved through the condition:

$$\sum_{i=1}^{m+1} \sigma_i = 1 \tag{A.1}$$

The set $B_p = \{b_i(\sigma_1, \sigma_2, .., \sigma_{m+1})\}$ also constitutes a complete collection of polynomials of degree p. This set B_p encompasses $\binom{p+n}{p}$ members, aligning with the count of degrees of freedom for the elements. By projecting data onto B_p, we can effectively reconstruct property q.

$$q = \sum_{i=1}^{\binom{p+n}{p}} c_i b_i \tag{A.2}$$

where c_i is the coefficient corresponding to the basis function b_i.

Expanding Equation A.2 yields the general polynomial q of order p as

$$q(\sigma_1, \sigma_2, .., \sigma_{m+1}) = \sum_{a_1+a_2+...+a_{m+1}=p} c_{a_1,a_2,...,a_{m+1}} \sigma_1^{a_1} \sigma_2^{a_2} ... \sigma_{m+1}^{a_{m+1}} \tag{A.3}$$

It's important to emphasize that due to the barycentric system employed to describe property q, the resulting expanded expression is not unique. While the reconstructed values remain consistent, the form of the expression can vary. However, by enforcing the requirement that each term in Equation A.3 corresponds to an order of p (which means $a_1 + a_2 + ... + a_{m+1} = p$ for each term), a distinct expression can be attained.

Given that the element $\mathbf{\Omega}$ possesses $\binom{p+n}{p}$ degrees of freedom, Equation A.3 generates a sufficient number of linear equations to determine each coefficient $c_{a_1,a_2,...,a_{m+1}}$. This proce-

dure is effectively utilized to derive the basis function b_i. By definition, b_i takes a value of 1 at the degree of freedom i and is set to 0 at any other degrees of freedom.

Upon solving the linear system, b_i, now described by Equation A.3, can be represented as an inner product between the vector of coefficients $\boldsymbol{\lambda}_i$ and the basis features $\boldsymbol{\varphi}_i$

$$b_i = \boldsymbol{\lambda}_i \cdot \boldsymbol{\varphi}_i \tag{A.4}$$

Note that in the case of Hermite elements, where information is represented as k^{th} order gradients, equation A.3 provides the derivative of the general polynomial q with respect to σ_i. For higher-order gradients, we can take derivatives of derivatives to obtain the corresponding partial derivatives of q with respect to the barycentric coordinates.

$$\frac{\partial q}{\partial \sigma_i} = \sum_{a_1+a_2+\ldots+a_{m+1}=p} c_{a_1,a_2,\ldots,a_{m+1}} \times \begin{cases} 0, & \text{if } a_i = 0 \\ a_i \times \sigma_1^{a_1}\sigma_2^{a_2}\ldots\sigma_{i-1}^{a_{i-1}}\sigma_i^{a_i-1}\sigma_{i+1}^{a_{i+1}}\ldots\sigma_{m+1}^{a_{m+1}}, & \text{otherwise} \end{cases} \tag{A.5}$$

Furthermore, if we seek to obtain the element average, the integral of each term in equation A.3 over the element, $\boldsymbol{\Omega}$, is given by

$$\int\int\cdots\int_{\boldsymbol{\Omega}} \sigma_1^{a_1}\sigma_2^{a_2}\ldots\sigma_{m+1}^{a_{m+1}}\, d\boldsymbol{\Omega} = \frac{m a_1! a_2! \ldots a_{m+1}!}{(a_1 + a_2 + \ldots + a_{m+1} + m)!} \tag{A.6}$$

APPENDIX B

Two-Dimensional Spherical Means Integrals

The spherical means integral in two-dimensional space for a function $q(x, y)$ defined in a Cartesian coordinate system and center (x_j, y_j) is expressed as

$$M_R\{q\}(x_j, y_j) = \frac{1}{2\pi R} \int_{\theta_P}^{\theta_Q} \int_0^R q(x_j + r\cos\theta, y_j + r\sin\theta) \frac{r}{\sqrt{R^2 - r^2}}\, dr\, d\theta \tag{B.1}$$

During the reconstruction stage, the active flux method interpolates the function q with a polynomial of order p, utilizing a set of basis functions B_p defined by

$$B_p = \{b_i(\sigma_1, \sigma_2, \sigma_3)\}, \quad i = 1, 2, \cdots, (p+1)(p+2)/2 \tag{B.2}$$

Subsequently, the function q is represented as

$$q(\sigma_1, \sigma_2, \sigma_3) = \sum_{i=1}^{(p+1)(p+2)/2} c_i b_i(\sigma_1, \sigma_2, \sigma_3) \tag{B.3}$$

In this equation, c_i corresponds to the coefficient associated with the basis function b_i. Here, b_i is a polynomial of order p, expressed in a general form as

$$b_i(\sigma_1, \sigma_2, \sigma_3) = \sum_{a_1+a_2+a_3=p} \lambda_{a_1,a_2,a_3} \sigma_1^{a_1} \sigma_2^{a_2} \sigma_3^{a_3} \tag{B.4}$$

For a comprehensive derivation of basis function b_i, refer to Appendix A.

Substituting Equation B.3 into Equation B.1 and expanding the basis function using

Equation B.4

$$
\begin{aligned}
M_R\{q\}(x_j, y_j) &= \frac{1}{2\pi R} \int_{\theta_P}^{\theta_Q} \int_0^R q(x_j + r\cos\theta, y_j + r\sin\theta) \frac{r}{\sqrt{R^2 - r^2}}\, dr\, d\theta \\
&= \frac{1}{2\pi R} \sum_{i=1}^{(p+1)(p+2)/2} c_i \int_{\theta_P}^{\theta_Q} \int_0^R b_i(\sigma_1, \sigma_2, \sigma_3) \frac{r}{\sqrt{R^2 - r^2}}\, dr\, d\theta \\
&= \frac{1}{2\pi R} \sum_{i=1}^{(p+1)(p+2)/2} c_i \sum_{a_1+a_2+a_3=p} \lambda_{a_1,a_2,a_3} \int_{\theta_P}^{\theta_Q} \int_0^R \sigma_1^{a_1}\sigma_2^{a_2}\sigma_3^{a_3} \frac{r}{\sqrt{R^2 - r^2}}\, dr\, d\theta \\
&= \frac{1}{2\pi R} \sum_{i=1}^{(p+1)(p+2)/2} c_i \sum_{a_1+a_2+a_3=p} \lambda_{a_1,a_2,a_3} I_{a_1,a_2,a_3}
\end{aligned} \tag{B.5}
$$

where I_{a_1,a_2,a_3} is defined as

$$
I_{a_1,a_2,a_3} = \int_{\theta_P}^{\theta_Q} \int_0^R \sigma_1^{a_1}\sigma_2^{a_2}\sigma_3^{a_3} \frac{r}{\sqrt{R^2 - r^2}}\, dr\, d\theta \tag{B.6}
$$

The barycentric coordinate system is correlated to the Cartesian coordinate system through the relationship defined by Equation 2.6. This relationship can be expressed in a simplified form as

$$
\sigma_i = A_i x + B_i y + C_i \tag{B.7}
$$

Here, A_i, B_i, and C_i are constant coefficients computed based on the element definition, as indicated in Equation 2.6.

Equation B.6 represents the spherical means integral of Equation B.1 with the integrand of the form $\sigma_1^{a_1}\sigma_2^{a_2}\sigma_3^{a_3}$. This expression can be expanded using Equation B.7 and further transformed into a polar coordinate system centered at (x_j, y_j) to become computable:

$$
\sigma_1^{a_1}\sigma_2^{a_2}\sigma_3^{a_3} = \prod_{i=1}^{3} [A_i(x_j + r\cos\theta) + B_i(y_j + r\sin\theta) + C_i]^{a_i} \tag{B.8}
$$

Considering that in Equation B.8, $a_1 + a_2 + a_3 = p$, the expansion of the right-hand side entails a linear combination of terms $[r\sin(\theta)]^{p_1}\,[r\cos(\theta)]^{p_2}$, where $0 \le p_1 + p_2 \le p$. This further subdivides the integral of Equation B.6 into more computationally manageable forms

$$
I_{(p_1,p_2)} = \int_{\theta_P}^{\theta_Q} \int_0^R \frac{(r\cos\theta)^{p_1}\,(r\sin\theta)^{p_2}}{\sqrt{R^2 - r^2}}\, dr d\theta \quad \text{and} \quad 0 \le p_1 + p_2 \le p \tag{B.9}
$$

These integrals possess a closed-form solution, which can be expressed as

$$I_{(p_1,p_2)} = R^{(p_1+p_2)}\Bigg(a_0(\theta_Q - \theta_P) + \sum_{i=1}^{p_1+p_2} a_i\left[\cos(i\theta_Q) - \cos(i\theta_P)\right] + b_i\left[\sin(i\theta_Q) - \sin(i\theta_P)\right]\Bigg) \tag{B.10}$$

where a_i and b_i are constant coefficients of the i^{th} term.

Table B.1 illustrates the closed-form solutions up to order five ($p = 5$) for the spherical means integrals. These solutions provide the fundamental basis for computing the spherical means of the solution state q, as defined in Equation B.1. Given the general form provided in Equation B.10, the closed-form solution involves a summation with constant coefficients for terms $\cos(i\theta_Q) - \cos(i\theta_P)$ and $\sin(i\theta_Q) - \sin(i\theta_P)$.

To enhance the readability of Table B.1, we introduce the operator $\Delta_f(i\theta_{PQ})$ as

$$\Delta_f(i\theta_{PQ}) \equiv f(i\theta_Q) - f(i\theta_P) \tag{B.11}$$

Here, $\Delta_f(i\theta_{PQ})$ is the foundation for calculating spherical mean integrals. Table B.1 highlights that when determining the spherical means of q at order p, it is essential to compute $\Delta_f(i\theta_{PQ})$ for values of i ranging from 0 to p. This approach is designed for computational efficiency because $\Delta_f(i\theta_{PQ})$ for each i is computed only once per degree of freedom. Higher-order integrals in this table involve $\Delta_f(i\theta_{PQ})$ with lower values of i that have already been computed at lower-order integrals.

Order	**Term**	**Spherical Means,** $I_{(p1,p2)}$
0	1	$\Delta_1(\theta_{PQ})/(2\pi)$
1	x	$R\Delta_{\sin}(\theta_{PQ})/8$
	y	$-R\Delta_{\cos}(\theta_{PQ})/8$
2	x^2	$R^2\left[2\Delta_1(\theta_{PQ}) + \Delta_{\sin}(2\theta_{PQ})\right]/(12\pi)$
	y^2	$R^2\left[2\Delta_1(\theta_{PQ}) - \Delta_{\sin}(2\theta_{PQ})\right]/(12\pi)$
	xy	$-R^2\Delta_{\cos}(2\theta_{PQ})/(12\pi)$
3	x^3	$R^3\left[9\Delta_{\sin}(\theta_{PQ}) + \Delta_{\sin}(3\theta_{PQ})\right]/128$
	y^3	$R^3\left[-9\Delta_{\cos}(\theta_{PQ}) + \Delta_{\cos}(3\theta_{PQ})\right]/128$
	x^2y	$-R^3\left[3\Delta_{\cos}(\theta_{PQ}) + \Delta_{\cos}(3\theta_{PQ})\right]/128$
	xy^2	$R^3\left[3\Delta_{\sin}(\theta_{PQ}) - \Delta_{\sin}(3\theta_{PQ})\right]/128$
4	x^4	$R^4\left[12\Delta_1(\theta_{PQ}) + 8\Delta_{\sin}(2\theta_{PQ}) + \Delta_{\sin}(4\theta_{PQ})\right]/(120\pi)$
	y^4	$R^4\left[12\Delta_1(\theta_{PQ}) - 8\Delta_{\sin}(2\theta_{PQ}) + \Delta_{\sin}(4\theta_{PQ})\right]/(120\pi)$
	x^3y	$-R^4\left[4\Delta_{\cos}(2\theta_{PQ}) + \Delta_{\cos}(4\theta_{PQ})\right]/(120\pi)$
	xy^3	$R^4\left[-4\Delta_{\cos}(2\theta_{PQ}) + \Delta_{\cos}(4\theta_{PQ})\right]/(120\pi)$
	x^2y^2	$R^4\left[4\Delta_1(\theta_{PQ}) - \Delta_{\sin}(4\theta_{PQ})\right]/(120\pi)$
5	x^5	$R^5\left[150\Delta_{\sin}(\theta_{PQ}) + 25\Delta_{\sin}(3\theta_{PQ}) + 3\Delta_{\sin}(5\theta_{PQ})\right]/3072$
	y^5	$-R^5\left[150\Delta_{\cos}(\theta_{PQ}) - 25\Delta_{\cos}(3\theta_{PQ}) + 3\Delta_{\cos}(5\theta_{PQ})\right]/3072$
	x^4y	$-R^5\left[10\Delta_{\cos}(\theta_{PQ}) + 5\Delta_{\cos}(3\theta_{PQ}) + \Delta_{\cos}(5\theta_{PQ})\right]/1024$
	xy^4	$R^5\left[10\Delta_{\sin}(\theta_{PQ}) - 5\Delta_{\sin}(3\theta_{PQ}) + \Delta_{\sin}(5\theta_{PQ})\right]/1024$
	x^3y^2	$R^5\left[30\Delta_{\sin}(\theta_{PQ}) - 5\Delta_{\sin}(3\theta_{PQ}) - 30\Delta_{\sin}(5\theta_{PQ})\right]/3072$
	x^2y^3	$-R^5\left[30\Delta_{\cos}(\theta_{PQ}) + 5\Delta_{\cos}(3\theta_{PQ}) - 30\Delta_{\cos}(5\theta_{PQ})\right]/3072$

Table B.1: Closed-form solutions for spherical mean integrals. We use the symbol x to represent $r\sin\theta$ and the symbol y for $r\cos\theta$. For additional details, refer to the data structure available at [1].

BIBLIOGRAPHY

[1] Iman Samani. Active flux. https://github.com/imansamani/ActiveFlux, 2023.

[2] Richard Blockley. Green aviation. John Wiley & Sons, 2016.

[3] Dennis L Huff. Noise mitigation strategies. Green Aviation, pages 83–104, 2018.

[4] Philip L Roe. Characteristic-based schemes for the euler equations. Annual review of fluid mechanics, 18(1):337–365, 1986.

[5] Marvin E Goldstein. A generalized acoustic analogy. Journal of Fluid Mechanics, 488:315–333, 2003.

[6] Gang Tan and Leon R Glicksman. Application of integrating multi-zone model with cfd simulation to natural ventilation prediction. Energy and Buildings, 37(10):1049–1057, 2005.

[7] Marco Bonvini, Mirza Popovac, and Alberto Leva. Sub-zonal computational fluid dynamics in an object-oriented modelling framework. In Building Simulation, volume 7, pages 439–454. Springer, 2014.

[8] Jian-Ming Jin. The finite element method in electromagnetics. John Wiley & Sons, 2015.

[9] Allen Taflove, Susan C Hagness, and Melinda Piket-May. Computational electromagnetics: the finite-difference time-domain method. The Electrical Engineering Handbook, 3(629-670):15, 2005.

[10] Stephen H Hall, Garrett W. Hall, and James A. McCall. High-speed digital system design—A handbook of interconnect theory and design practices. John Wiley & Sons, 2000.

[11] Peter M Shearer. Introduction to seismology. Cambridge university press, 2019.

[12] Jeroen Tromp, Dimitri Komatitsch, and Qinya Liu. Spectral-element and adjoint methods in seismology. Communications in Computational Physics, 3(1):1–32, 2008.

[13] Maureen D Long and Thorsten W Becker. Mantle dynamics and seismic anisotropy. Earth and Planetary Science Letters, 297(3-4):341–354, 2010.

[14] Gordon D Smith. Numerical solution of partial differential equations: finite difference methods. Oxford university press, 1985.

[15] Bertil Gustafsson, Heinz-Otto Kreiss, and Joseph Oliger. Time dependent problems and difference methods, volume 2. Wiley Online Library, 2013.

[16] Adrian Sescu, Ray Hixon, and Abdollah A Afjeh. Multidimensional optimization of finite difference schemes for computational aeroacoustics. Journal of Computational Physics, 227(9):4563–4588, 2008.

[17] Kane Yee. Numerical solution of initial boundary value problems involving maxwell's equations in isotropic media. IEEE Transactions on antennas and propagation, 14(3):302–307, 1966.

[18] Hideo Aochi, Thomas Ulrich, Ariane Ducellier, Fabrice Dupros, and David Michea. Finite difference simulations of seismic wave propagation for understanding earthquake physics and predicting ground motions: Advances and challenges. In Journal of Physics: Conference Series, volume 454, page 012010. IOP Publishing, 2013.

[19] Susanne C Brenner. The mathematical theory of finite element methods. Springer, 2008.

[20] Patrick Joly. Variational methods for time-dependent wave propagation problems. In Topics in computational wave propagation: direct and inverse problems, pages 201–264. Springer, 2003.

[21] Mark S Gockenbach. Understanding and implementing the finite element method, volume 97. Siam, 2006.

[22] Béatrice Rivière. Discontinuous Galerkin methods for solving elliptic and parabolic equations: theory and implementation. SIAM, 2008.

[23] William H Reed and Thomas R Hill. Triangular mesh methods for the neutron transport equation. Technical report, Los Alamos Scientific Lab., N. Mex.(USA), 1973.

[24] Michel O Deville, Paul F Fischer, and Ernest H Mund. High-order methods for incompressible fluid flow, volume 9. Cambridge university press, 2002.

[25] Philip L. Roe. Designing CFD methods for bandwidth—a physical approach. Computers & Fluids, 214:104774, 2021.

[26] Alberto Bressan. Hyperbolic systems of conservation laws: the one-dimensional Cauchy problem, volume 20. Oxford Lecture Mathematics and, 2000.

[27] John George Fletcher. Local conservation laws in generally covariant theories. Reviews of Modern Physics, 32(1):65, 1960.

[28] Soo-Hyung Park and Jang Kwon. An improved hlle method for hypersonic viscous flows. In 15th AIAA Computational Fluid Dynamics Conference, page 2633, 2001.

[29] Phillip Colella. Multidimensional upwind methods for hyperbolic conservation laws. Journal of computational physics, 87(1):171–200, 1990.

[30] Stephen F Davis. A rotationally biased upwind difference scheme for the euler equations. Journal of Computational Physics, 56(1):65–92, 1984.

[31] David W Levy, Kenneth G Powell, and Bram van Leer. Use of a rotated riemann solver for the two-dimensional euler equations. Journal of Computational Physics, 106(2):201–214, 1993.

[32] Randall J Leveque. High-resolution conservative algorithms for advection in incompressible flow. SIAM Journal on Numerical Analysis, 33(2):627–665, 1996.

[33] Philip L. Roe. Is discontinuous reconstruction really a good idea? Journal of Scientific Computing, 73(2):1094–1114, 2017.

[34] Philip Roe. Did numerical methods for hyperbolic problems take a wrong turning? In Theory, Numerics and Applications of Hyperbolic Problems II: Aachen, Germany, August 2016, pages 517–534. Springer, 2018.

[35] Philip Roe. Fluctuations and signals-a framework for numerical evolution problems. Numerical methods for fluid dynamics, 11, 1982.

[36] Mani Rad. A residual distribution approach to the Euler equations that preserves potential flow. PhD thesis, University of Michigan, Ann Arbor, 2001.

[37] Hiroaki Nishikawa, Mani Rad, and Philip Roe. A third-order fluctuation splitting scheme that preserves potential flow. In 15th AIAA computational fluid dynamics conference, page 2595, 2013.

[38] Claudio Canuto, M Yousuff Hussaini, Alfio Quarteroni, and Thomas A Zang. Spectral methods: fundamentals in single domains. Springer Science & Business Media, 2007.

[39] David Gottlieb and Steven A Orszag. Numerical analysis of spectral methods: theory and applications. SIAM, 1977.

[40] Hans Schamel and Klaus Elsässer. The application of the spectral method to nonlinear wave propagation. Journal of Computational Physics, 22(4):501–516, 1976.

[41] Stephen B Wineberg, Joseph F McGrath, Edward F Gabl, L Ridgway Scott, and Charles E Southwell. Implicit spectral methods for wave propagation problems. Journal of computational physics, 97(2):311–336, 1991.

[42] Bram Van Leer. Towards the ultimate conservative difference scheme. iv. a new approach to numerical convection. Journal of computational physics, 23(3):276–299, 1977.

[43] Jungyeoul Maeng. On the advective component of active flux schemes for nonlinear hyperbolic conservation laws. PhD thesis, University of Michigan, Ann Arbor, 2017.

[44] Duoming Fan. On the acoustic component of active flux schemes for nonlinear hyperbolic conservation laws. PhD thesis, University of Michigan, Ann Arbor, 2017.

[45] Zhijian J Wang, Krzysztof Fidkowski, Rémi Abgrall, Francesco Bassi, Doru Caraeni, Andrew Cary, Herman Deconinck, Ralf Hartmann, Koen Hillewaert, Hung T Huynh, et al. High-order cfd methods: current status and perspective. International Journal for Numerical Methods in Fluids, 72(8):811–845, 2013.

[46] A Harten, B Engquist, S Osher, and S.R. Chakravarthy. Uniformly high order accurate essentially non-oscillatory schemes, iii. Journal of Computational Physics, 71:231–303, 1987.

[47] X.D. Liu, S Osher, and T. Chan. Weighted essentially non-oscillatory schemes. Journal of Computational Physics, 115:200–212, 1994.

[48] Jiayin Li, Chi-Wang Shu, and Jianxian Qiu. Moment-based multi-resolution HWENO scheme for hyperbolic conservation laws. Communications in Computational Physics, 32(2):364–400, 2022.

[49] Lin Fu, Xiangyu Y Hu, and Nikolaus A Adams. A new class of adaptive high-order targeted eno schemes for hyperbolic conservation laws. Journal of Computational Physics, 374:724–751, 2018.

[50] Christopher KW Tam and Jay C Webb. Dispersion-relation-preserving finite difference schemes for computational acoustics. Journal of computational physics, 107(2):262–281, 1993.

[51] Oded Ovadia, Adar Kahana, and Eli Turkel. A convolutional dispersion relation preserving scheme for the acoustic wave equation. arXiv preprint arXiv:2205.10825, 2022.

[52] G. W. Hedstrom. Models of difference schemes for $u_t + u_x = 0$ by partial differential equations. Journal of Computational Physics, 29:969–977, 1975.

[53] D Bouche, G Bonnaud, and D Ramos. Comparison of numerical schemes for solving the advection equation. Applied Mathematics Letters, 16, 2003.

[54] Arieh Iserles and Gilbert Strang. The optimal accuracy of difference schemes. Transactions of the American Mathematical Society, 277(2):779–803, 1983.

[55] Thibault Dairay, Eric Lamballais, Sylvain Laizet, and John Christos Vassilicos. Numerical dissipation vs. subgrid-scale modelling for large eddy simulation. Journal of Computational Physics, 337:252–274, 2017.

[56] Gianmarco Mengaldo, RC Moura, B Giralda, J Peiró, and SJ Sherwin. Spatial eigensolution analysis of discontinuous galerkin schemes with practical insights for under-resolved computations and implicit les. Computers & Fluids, 169:349–364, 2018.

[57] Rémi Abgrall and Wasilij Barsukow. Extensions of active flux to arbitrary order of accuracy. arXiv preprint arXiv:2208.14476, 2022.

[58] Alexander Ženíšek. Interpolation polynomials on the triangle. Numer.Math, 15:271–277, 1970.

[59] Archna Kumari and Vijay K Kukreja. Survey of Hermite interpolating polynomials for the solution of differential equations. Mathematics, 11.14:3157, 2023.

[60] John Goodrich, Thomas Hagstrom, and Jens Lorenz. Hermite methods for hyperbolic initial-boundary value problems. Mathematics of computation, 75(254):595–630, 2006.

[61] Arturo Vargas, Jesse Chan, Thomas Hagstrom, and Timothy Warburton. Variations on hermite methods for wave propagation. Communications in Computational Physics, 22(2):303–337, 2017.

[62] Xi Ronald Chen, Daniel Appelö, and Thomas Hagstrom. A hybrid hermite–discontinuous galerkin method for hyperbolic systems with application to maxwell's equations. Journal of Computational Physics, 257:501–520, 2014.

[63] Doreen Fan and Philip L Roe. Investigations of a new scheme for wave propagation. In 22nd AIAA Computational Fluid Dynamics Conference, page 2449, 2015.

[64] Gerald Beresford Whitham. Linear and nonlinear waves, volume 42. John Wiley & Sons, 2011.

[65] Jianxian Qiu and Chi-Wang Shu. Hermite WENO schemes and their application as limiters for runge–kutta discontinuous galerkin method: one-dimensional case. Journal of Computational Physics, 193(1):115–135, 2004.

[66] Milton Abramowitz, Irene A Stegun, and Robert H Romer. Handbook of mathematical functions with formulas, graphs, and mathematical tables, 1988.

[67] Timothy Eymann and Philip Roe. Active flux schemes. In 49th AIAA Aerospace Sciences Meeting including the New Horizons Forum and Aerospace Exposition, page 382, 2011.

[68] Richard Courant and David Hilbert. Methods of mathematical physics: partial differential equations. John Wiley & Sons, 2008.

[69] Timothy A Eymann and Philip L Roe. Multidimensional active flux schemes. In 21st AIAA computational fluid dynamics conference, page 2940, 2013.

[70] Wasilij Barsukow, Jonathan Hohm, Christian Klingenberg, and Philip L Roe. The active flux scheme on cartesian grids and its low mach number limit. Journal of Scientific Computing, 81:594–622, 2019.

[71] Fanchen He and Philip L Roe. The treatment of conservation in the active flux method. In AIAA AVIATION 2020 FORUM, page 3032, 2020.

[72] M. Lukacova-Medvidova, K.W. Morton, and G. Warnecke. Finite volume evolution galerkin methods for hyperbolic systems. SIAM Journal on Scientific Computing, 26(1):1–30, 2004.

[73] Fang Q Hu. A stable, perfectly matched layer for linearized euler equations in unsplit physical variables. Journal of Computational Physics, 173(2):455–480, 2001.

[74] A Verhoff, D Stookesberry, and S Agrawal. Asymptotic far-field boundary conditions for numerical flowfield predictions. In Thirteenth International Conference on Numerical Methods in Fluid Dynamics: Proceedings of the Conference Held at the Consiglio Nazionale delle Ricerche Rome, Italy, 6–10 July 1992, pages 488–493. Springer, 2005.

[75] Nathan Edgar and Miguel Visbal. A general buffer zone-type non-reflecting boundary condition for computational aeroacoustics. In 9th AIAA/CEAS Aeroacoustics Conference and Exhibit, page 3300, 2003.

[76] Fang Q Hu, XD Li, and DK2406542 Lin. Absorbing boundary conditions for nonlinear euler and navier–stokes equations based on the perfectly matched layer technique. Journal of computational physics, 227(9):4398–4424, 2008.

[77] Chun Sang Yoo, Yi Wang, Arnaud Trouvé, and Hong G Im. Characteristic boundary conditions for direct simulations of turbulent counterflow flames. Combustion Theory and Modelling, 9(4):617–646, 2005.

[78] Dan Givoli. High-order local non-reflecting boundary conditions: a review. Wave motion, 39(4):319–326, 2004.

[79] Robert L Higdon. Numerical absorbing boundary conditions for the wave equation. Mathematics of computation, 49(179):65–90, 1987.

[80] Florent Pled and Christophe Desceliers. Review and recent developments on the perfectly matched layer (pml) method for the numerical modeling and simulation of elastic wave propagation in unbounded domains. Archives of Computational Methods in Engineering, 29(1):471–518, 2022.

[81] Tyler B Lung and Philip L Roe. Toward a reduction of mesh imprinting. International Journal for Numerical Methods in Fluids, 76(7):450–470, 2014.

[82] Shuichi Nakazawa. The application of a two-dimensional upwind leapfrog scheme to linear elastodynamics. PhD thesis, University of Michigan, Ann Arbor, 2001.

[83] Philip Roe. Linear bicharacteristic schemes without dissipation. SIAM Journal on Scientific Computing, 19(5):1405–1427, 1998.

[84] John Arthur Hudson. The Excitation and Propagation of Elastic Waves. Cambridge University Press, 1984.